NON-INVASIVE MONITORING OF DEGRADATION OF POLY (lactide-co-glycolide) HOLLOW FIBER CHANNEL FOR RECOVERY OF SPINAL CORD INJURY USING MAGNETIC RESONANCE IMAGING

By:

Sagedeh Sadat Shahabi

A thesis submitted to the
Faculty of Graduate and Postdoctoral Studies
In partial fulfillment of the requirements

Master of Applied Science in Biomedical Engineering

Department of Mechanical Engineering
Faculty of Engineering
University of Ottawa

To my grandfather

Statement of Contributions of Collaborators

I hereby declare that I am the sole author of this Masters' thesis. All the experimental and analytical work related to this thesis is performed by me under the supervision and training received from Professor Xudong Cao.

My supervisor, Prof. Cao, provided me with an excellent collaboration throughout this work with laboratory training, discussions, supports and editorial comments for all of my written work. As a result the quality of this thesis has been tremendously improved through his guidance.

Signature: Sagedeh Sadat Shahabi

Date: 2012-09-24

ABSTRACT

Spinal cord injury (SCI) leads to axonal damage and limits the ability of the brain to communicate with the rest of the body. Several bioengineered approaches have been developed for the recovery of SCI. Among these techniques, degradable guidance tubes have shown promising results. However, design of nerve guide tubes requires several design considerations and has been a significant challenge. To assess the efficacy of a prototypical implanted nerve guide tubes, it is essential to perform continuous monitoring. In this respect, magnetic resonance imaging (MRI) is one of the most reliable imaging techniques as it offers the ability to achieve extraordinary high temporal and spatial resolution in addition to its non-invasive features. In spite of the excellent image quality of non-enhanced MRI various types of contrast agents have been developed to further enhance the contrast and allow improved visualization. The MRI contrast agents principally work by shortening the T_1 or T_2 relaxation times of protons located nearby.

The presented study was intended to evaluate the *in vitro* degradation of the nerve guide tubes made of poly (lactic-co-glycolic acid) (PLGA). PLGA tubes incorporated with different concentrations of superparamagnetic iron oxide (SPIO) were scanned by MRI 3T on weekly basis during the degradation period. Spin-echo (SE) sequence with various echo times (TEs) ranged from 13.3 to 314.4 msec was applied. T_2 mapping was computed using in-house algorithm developed in Matlab. Least square fit was used to find the slope of the decay curve by plotting log intensity on the y-axis and echo time on the x-axis. The average T2 values were calculated.

Mass loss and water uptake of the degrading tubes were also measured weekly. Moreover, the micro-structural changes of the tubes were investigated using the scanning electron microscope (SEM). The MRI results showed that the concentration of SPIO affects the signal intensity of the T_2 weighted images reducing the T_2 relaxation time value. Accordingly, a linear correlation between SPIO concentration and T_2 relaxation time was found. At the beginning of degradation, the SPIO nanoparticles were trapped within the polymeric network. Therefore, water penetration was the predominant factor affecting the T_2 relaxation times. At week 5, a significant mass loss was observed. From this stage onwards, the trapped SPIO were released from the polymeric network increasing T_2 relaxation time dramatically. According to SEM images, the size of the pores in PLGA guide tubes was increased with the degradation. Approaching the end of degradation, shrinkage of the tubes was observed and the degraded nerve guide tubes were shown to be collapsed. Similar shape variation was observed in T_2 weighted MR images.

In summary, this study provided an approach to non-invasive monitoring of degradation behavior of nerve guide tubes using contrast enhancement. The developed technique is of great importance since it opened an insight to non-invasive monitoring of tissue engineered scaffolds for *in vivo* studies.

Keywords: *Degradation, MRI, non-invasive, PLGA, T2 relaxation time*

Résumé

Un traumatisme médullaire (TM) mène à la dissociation des neurones du système nerveux central (SCN) qui sont responsable de la communication entre le cerveau et les autres parties du corps. Indépendamment de la chirurgie et les greffes nerveuses, il y a plusieurs approches mis au point par des techniques biologiques qui furent développées pour la récupération de TM. Parmi ces techniques, l'utilisation de tubes de guidage de nerf dégradables ont généré des résultats favorables. Cependant, la conception de tubes de guidage de nerf demande plusieurs considérations et fut un défi substantiel. Afin de déterminer l'efficacité des tubes de guidage de nerf une fois implantés, il est nécessaire d'effectuer une surveillance continue. Pour cet aspect, l'imagerie par résonance magnétique (IRM) est une des techniques d'imagerie les plus fiables puisqu'elle permet d'obtenir une résolution spatiale et dans le temps extrêmement élevé, en plus d'être non invasif.

Malgré l'excellente qualité de l'image de l'IRM non améliorée, plusieurs types de substances de contraste furent développé afin d'améliorer d'avantage le contraste. Les substances de contraste de l'IRM fonctionnent principalement en diminuant les temps de relaxation T1 ou T2 des protons situés à proximité immédiate. L'étude suivante avait pour but d'évaluer la dégradation *in vitro* des tubes de guidage (PLGA). Les tubes PLGA incorporé avec des concentrations différentes d'oxyde de fer superparamagnétique (OFSP) furent examinés par IRM 3T d'une façon hebdomadaire durant la période de dégradation. Une séquence d'écho de spin (ES) fut appliquée comprenant une variété de temps d'écho (TEs) allant de 13.3 à 314.4 ms.

Le mappage T2 fut calculé en utilisant un algorithme développé à Matlab. La technique d'ajustement par les moindres carrés fut utilisée pour identifier la pente de la courbe de déclin en traçant l'intensité log sur l'axe des y et le temps d'écho sur l'axe des x. La moyenne des valeurs T2 fut calculée. La perte de poids et l'absorption de l'eau des tubes en état de dégradation fut également mesuré à chaque semaine. De plus, les changements de la microstructure des tubes furent observés en utilisant un microscope électronique à balayage (MEB). Les résultats du IRM démontrent que la concentration d'OFSP a un impact sur l'intensité du signale des images pondérés T2, ce qui réduit le temps de relaxation de T2. Par conséquent, on a trouvé une corrélation linéaire entre la concentration d'OFSP et le temps de relaxation de T2. Au début de la dégradation, les nanoparticules d'OFSP étaient immobilisées à l'intérieur du réseau polymérique. En conséquent, la pénétration d'eau fut le facteur prédominant ayant un impact sur le temps de relaxation de T2.

Une perte de poids significative fut observée à la cinquième semaine. A partir de ce stade, les OFSP antérieurement immobilisées furent libérés du réseau polymérique, ce qui a augmenté le temps de relaxation de T2 d'une façon drastique. D'après les images produites par le MEB, la grosseur des pores des tubes de guidage PLGA a augmenté avec la dégradation. En approchant la fin de la dégradation, on a observé un rétrécissement des tubes et les tubes de guidage de nerfs furent affaissés. Une variation similaire des formes fut observée dans les images pondérées de T2 obtenue par IRM.

En résumé, cette étude offre une approche à l'étude non invasive du comportement de dégradation des tubes de guidage de nerf en utilisant un IRM à contraste amélioré. Les techniques développées sont de grande importance puisqu'elles offrent une nouvelle méthode de surveillance non invasive des échafaudages en ingénierie tissulaire pour les études *in vivo.*

Acknowledgements

I wish to express my most sincere appreciation to Prof. Xudong Cao for his supervision, patience, encouragement and his constructive comments throughout the development of the project. I would like to thank Dr. Eve Tsai for her tremendous guidance.

Special thanks to Dr. Karunanithi Rajamanickam who directed me in the magnetic resonance imaging studies. His kind support has been of great value in this study.

Many thanks to all the technicians of Department of Chemical and Biological Engineering at University of Ottawa and also to the MRI staff at Civic Hospital for their co-operation.

I would like to thank my colleagues Nan Cheng, Cathy Goubko, Yan Du, Matthew Coyle, Harrison Westwick and Ushananthini Shanmugalingam who have been of invaluable assistance when I hit a bottleneck during the period of completing this project.

Last but not least, my deepest gratitude goes to my beloved parents and siblings for their faith in me and allowing me to be as ambitious as I wanted to.

Table of Contents

Statement of Contributions of Collaborators 3
ABSTRACT iv
Résumé vi
Acknowledgements viii
FIGURES AND TABLES xi
List of Acronyms xiii
List of symbols xv
Chapter 1- INTRODUCTION 1
1.2 Thesis objectives 3
1.3 Organization of the thesis 4
1.4 Thesis hypothesis 4
Chapter 2- LITERATURE REVIEW 5
2.1 Nerve regeneration 5
2.1.1 Peripheral nervous system (PNS) regeneration 6
2.1.2 Central nervous system (CNS) regeneration 8
2.2 Spinal cord injury 8
2.3 Bioengineered strategies for recovery of spinal cord injury 12
2.3.1 Polymeric guidance channels 14
2.4 Essential properties for guidance channels in CNS 15
2.4.1 Polymeric degradation 19
2.5 Materials design strategies 22
2.5.1 Natural polymers 24
2.5.2 Synthetic polymers 28
2.5.3 Fabrication techniques 31
2.6 Magnetic Resonance Imaging (MRI) 34
2.6.1 T_1, T_2 and T_2* Relaxation Time 39
2.6.2 MRI mapping 41
2.6.3 Spin-Echo pulse sequence 42
2.6.4 MR contrast agents 44
2.6.5 Super paramagnetic iron oxide (SPIO) 45

2.6.6 MRI in tissue engineering and drug delivery 46
Chapter 3- Materials and methods 53
3.1 Materials 53
3.2 Fabrication of PLGA hollow fiber channel 53
3.3 Sub-critical CO_2 foaming 54
3.4 Preparation of SPIO nanoparticles loaded PLGA channels 55
3.4 *In vitro* degradation 56
3.4.1 Mass loss and water uptake 58
3.4.2 Magnetic Resonance Imaging (MRI) monitoring 58
3.4.3 Scanning Electron Microscopy (SEM) 59
3.4.4 Statistical analysis 59
Chapter 4- RESULTS 60
4.1 Mass loss 61
4.2 Water uptake 61
4.3 MRI monitoring 63
4.4 Scanning Electron Microscopy (SEM) 68
Chapter 5- DISCUSSION 70
5.1 Mass loss and water uptake 70
5.2 MRI monitoring 72
5.3 Scanning Electron Microscopy (SEM) 75
Chapter 6- CONCLUSIONS 76
Chapter 7- FUTURE WORKS 78
References 79
Appendices 90

FIGURES AND TABLES

FIG 1. 1 REPRESENTATIVE T_2 WEIGHTED MR IMAGE OF TRANSECTED RAT SPINAL CORD. POINTER SHOWS THE LOCATION OF PLGA HOLLOW FIBER CHANNEL WITH 0% SPIO 2

FIG 2. 1 NERVE REGENERATION PROCESS IN PNS AFTER INJURY[3] 6
FIG 2. 2 SIDE VIEW AND TRANSVERSE CROSS SECTION OF SPINAL CORD[15] 9
FIG 2. 3 SCHEMATIC DIAGRAM DEMONSTRATING THE INFILTRATION OF CELLS INTO INJURY SITE OF THE SPINAL CORD [20] 11
FIG 2. 4 SCHEMATIC DEMONSTRATION OF HYDROLYTIC DEGRADATION [49] 20
FIG 2. 5 FABRICATION METHODS FOR NERVE GUIDE TUBES[128] 33
FIG 2. 6 THE SPIN AND CHARGE OF A PROTON (A) CAUSES IT TO HAVE A MAGNETIC FIELD THAT TENDS TO ALIGN WITH AN APPLIED MAGNETIC FIELD B_0 (B). WHEN THE MAGNETIZATION VECTOR IS TILTED AWAY FROM VERTICAL IT UNDERGOES PRECESSION (D). THE PROTON ALSO HAS ANGULAR MOMENTUM IN THE FORM OF SPIN, WHICH WILL CAUSE IT TO PROCESS AT A FREQUENCY $w\varphi$ WHEN IT IS TIPPED OUT OF ALIGNMENT WITH THE B_0 FIELD (C). A GROUP OF SPINS PROCESS IN SYNCHRONY WHEN EXPOSED TO A UNIFORM MAGNETIC FIELD (E), WHICH FORMS A BULK MAGNETIZATION (F) REPRESENTED BY A VECTOR THAT PROCESSES AT THE SAME FREQUENCY[133] 36
FIG 2. 7 ROTATING MAGNETIZATION INDUCES A SIGNAL THAT OSCILLATES AT FREQUENCY $w\varphi$ VIA AN AMPLIFIED TUNED COIL. TWO COILS PLACED A RIGHT ANGLES SAMPLE DIFFERENT PHASES OF THE ROTATING MAGNETIZATION (A) WHICH CAN BE USED TO MEASURE THE SPIN PHASE. TRANSVERSE MAGNETIZATION CAN BE GENERATED BY AN APPLIED ALTERNATING MAGNETIC FIELD AT FREQUENCY $w\varphi$ CAUSING THE MAGNETIZATION TO TILT AWAY FROM THE Z AXIS TOWARD THE TRANSVERSE PLANE (B)[133] 38
FIG 2. 8 SPIN-LATTICE OR T_1 RELAXATION. AFTER A 90˚ RF PULSE, MAGNETIZATION IS TILTED INTO THE TRANSVERSE PLANE (A) AFTER WHICH IT UNDERGOES TRANSVERSE RELAXATION AND SIGNAL LOSS (B) AND A GRADUAL GROWTH OF LONGITUDINAL (M_Z) MAGNETIZATION WITH TIME (C). THIS RESULTS IN A CURVE OF M_Z WITH TIME WHICH IS CHARACTERIZED BY A RELAXATION TIME CONSTANT T_1, DEFINED AS THE TIME TO REACH 63% OF ITS EQUILIBRIUM VALUE (D)[133] 40
FIG 2. 9 FACTORS THAT LEAD TO T_2* RELAXATION. STATIC FIELD VARIATIONS IN SPACE DUE TO TISSUE SUSCEPTIBILITY VARIATIONS (A). IN ADDITION, RANDOM INTERACTIONS BETWEEN THE MAGNETIC PROPERTIES OF SPINS THEMSELVES (B) AND THEIR RANDOM MOTION THROUGH REGIONS OF DIFFERENT MAGNETIC FIELDS (C) WILL RESULT IN ADDITIONAL LOSS OF SIGNAL. RANDOM MECHANISMS ARE RESPONSIBLE FOR DECAY CHARACTERIZED BY T_2 WHILE THE ADDITION OF STATIC FIELD VARIATIONS LEADS TO FASTER SIGNAL LOSS AS CHARACTERIZED BY T_2* (D)[133] 41
FIG 2. 10 VARIATION OF T_2 RELAXATION TIMES FOR DIFFERENT SPIO CONCENTRATION[169] 48
FIG 2. 11 IN VITRO RELAXOMETRY OF SPIO LABELED MSCS[169] 48
FIG 2. 12 MR IMAGE OBTAINED WITH A FAST SPIN ECHO SEQUENCE FROM SPIO LABELED MSCS IN A SPONGE OF 5 mm^3 (1) AND 3 mm^3 (2) AND UNLABELED CELLS IN A SPONGES OF 5 mm^3 (3) AND 3 mm^3 (4)[169] 49
FIG 2. 13 HIGH-RESOLUTION 3D MRI OF HYDROGEL SCAFFOLDS WITH DIFFERENT INTERNAL STRUCTURES. TRANSVERSE AND LONGITUDINAL SLICES ARE SHOWN. SLICE LOCATION IS MARKED BY A LINE. GADOLINIUM-DOPED HYDRATION MEDIUM IS SEEN AS AREAS OF ENHANCED INTENSITY, WHEREAS AREAS OF REDUCED INTENSITY INDICATE THE PRESENCE OF STRUCTURED SCAFFOLD. (A) MICROPOROUS SCAFFOLD: MR IMAGE REVEALS POROUS ARCHITECTURE WITH SMALL QUASISPHERICAL CAVITIES. (B) MACROPOROUS SCAFFOLD: MR IMAGE SHOWS A HIGHLY POROUS STRUCTURE WITH LARGE PORES WHOSE OUTLINES ARE CLEARLY VISIBLE. (C) LAMELLAR SCAFFOLD: MR IMAGE REVEALS A 3D LAMELLAR STRUCTURE [171] 52

FIG 3. 1 TEFLON MOLDS (LEFT), VACUUME DRIED PLGA CHANNELS WITHIN TEFLON MOLDS PRIOR TO CO2 FOAMING PROCESS (RIGHT) 54
FIG 3. 2THE SCHEMATIC DIAGRAM OF DIP COATING PROCESS 55
FIG 3. 3 HYDROLYTIC DEGRADATION OF PLGA 56
FIG 3. 4 SCHEMATIC DIAGRAM OF SPIO LOADED PLGA (50:50) HYDROLYTIC DEGRADATION IN 50 ML PBS AT 37ºC 57

FIG 4. 1 PLGA HOLLOW FIBER CHANNEL 60

FIG 4. 2 ACCUMULATIVE MASS LOSS (%) OF PLAIN PLGA HOLLOW FIBER CHANNEL DURING DEGRADATION PERIOD. THE VERTICAL ERROR BARS INDICATE THE STANDARD DEVIATION. WEEK 2, WEEK3, WEEK 4 AND WEEK 5 POSE VERY SMALL STANDARD DEVIATIONS. 62
FIG 4. 3 WATER UPTAKE OF PLAIN PLGA HOLLOW FIBER CHANNEL DURING DEGRADATION PERIOD. THE VERTICAL ERROR BARS INDICATE THE STANDARD DEVIATION. WEEK 2 POSES VERY SMALL STANDARD DEVIATION 62
FIG 4. 4 T_2-WEIGHTED MR IMAGES OF PLGA HFC WITH 0.2 % SPIO (A) AXIAL AND (B) SAGITTAL VIEW 64
FIG 4. 5 ILLUSTRATION OF T_2 DECAY CURVES MEASURED FOR DIFFERENT CONCENTRATION OF SPIO (0.05%, 0.1% AND 0.2%) (A). AXIAL T_2 WEIGHTED MR IMAGES (LEFT) AND T_2 MAP (RIGHT) FOR PLGA HFCS WITH DIFFERENT CONCENTRATION OF SPIO (0%, 0.05%, 0.1% AND 0.2%) BEFORE DEGRADATION PROCESS BEGINS(B). 65
FIG 4. 6 RELAXATION TIME (T_2) VERSUS DIFFERENT CONCENTRATION OF SPIO (0%, 0.05%, 0.1% AND 0.2%). ERROR BARS INDICATE THE STANDARD DEVIATION. T2 RELAXATION VALUE FOR PLGA LOADED WITH 0.2% SPIO POSES VERY SMALL STANDARD DEVIATION 66
FIG 4. 7 DEGRADATION PATTERN OF PLGA HOLLOW FIBER CHANNELS; CURVE FIT BETWEEN T2 RELAXATION TIME (MS) AND DEGRADATION TIME (MS) 67
FIG 4. 8 AXIAL VIEW OF T2 WEIGHTED MRI FOR PLGA CHANNELS LOADED WITH DIFFERENT CONCENTRATION OF SPIO(0.05%, 0.1%, 0.2%) DURING 1ST, 4TH AND 8TH WEEK OF DEGRADATION 68

FIG 4.9 SEM VISUALIZATION FOR PLAIN PLGA HFCS (LEFT) VERSUS ZOOMED VIEW OF T_2 WEIGHTED MR IMAGES (RIGHT), SHOWING THE DEGRADATION OVER 6 WEEKS. MRI SCALE = 1×1×5 MM 69

List of Acronyms

Acronyms symbol	name
2D	Two dimension
3D	Three dimension
aNSC	adult neural stem cell
BBB	Blood-brain-barrier
CNS	Central nervous system
CNTF	Ciliary neurotrophic factor
CPI	Cell proliferation index
ECM	Extracellular matrix
FDA	Food and drug administration
FGF	Fibroblast growth factor
FID	Free induction decay
FOV	Field of view
GA	Glutaraldehyde
GAG	Glycosylaminoglycan
Gd	Gadolinium
HA	Hyaluronic acid
HFC	Hollow fiber channel
hUCBSC	human Umbilical cord blood stem cell
IV	Inherent Viscosity
MBP	Myelin basic protein
MRI	Magnetic resonance imaging
MSC	Mesenchymal cell
NGF	Neural growth factor

NMR	Nuclear magnetic resonance
NSPC	Neural stem/progenitor cell
NT-3	Neurotrophin-3
OEC	Olfactory ensheathing cell
PBS	Phosphate buffered saline
PCL	poly(ε-caprolactone)
PCLA	poly(e-caprolactone) acrylate
PED	poly (ethyleneterephathalate)/dimer
PGA	poly (glycolic acid)
PGS	poly (cyglycerol sebacate)
PHB	poly(β-hydroxybutyrate)
PLA	poly (lactic acid)
PLCL	poly (L-lactide-co-ε-caprolactone)
PLGA	ploy (lactic- co-glycolic acid)
PNS	Peripheral nervous system
RF	Radio frequency
SCI	Spinal cord injury
SE	Spin echo
SEM	Scanning electron microscope
SPIO	Superparamagnetic resonance iron oxide
T_g	Transition temperature
TZ	Transition zone
UV	Ultraviolet

List of symbols

Symbol	Name	Unit
Bo	Applied magnetic field	---
B_{φ}	External magnetic field strength	T
Fe_2O_3	Maghemite	---
Fe_3O_4	Magnetite	---
IV	Inherent Viscosity	dL/g
mo	Initial mass	mg
md	Dry mass	mg
mw	Wet mass	mg
M_z	Net magnetization vector	---
M_Z	External magnetic field	---
$S_{t=0}$	Signal intensity at the moment of magnetization creation	---
S(t)	signal intensity at time t	---
T_1	Longitudinal relaxation time	ms
T_2	Transverse relaxation time	ms
T_2^*	Transverse relaxation time due to local inhomogenity	ms
TE	Echo time	ms
TR	Repetition time	ms
W_{φ}	Larmor frequency	MHz
Φ	Angular momentum	N·m·s
γ	Gyromagnetic ratio	MHz/T

Chapter 1- INTRODUCTION

Over the past years, guidance channels have created enormous enthusiasm for SCI. The ultimate goal is to construct 3D structure that promotes axonal regeneration to repair the injured spinal cord. The key issues to produce a nerve guide tube include selection of the appropriate biomaterial and fabrication method. It is preferable to use degradable materials; because they reduce the complications posed by foreign objects and prevent compression of the regenerating nerves through degradation. However, concerns remain about the *in vivo* mechanism of degradation of implanted nerve tubes. To improve the design of materials for biodegradable nerve guidance channels and to obtain a better understanding of the degradation and repair process, it would be ideal to have a method of continuously tracking degradation and regeneration after implantation in animal models. There are various monitoring techniques which could be used for this purpose.

Some of the current monitoring methods have high risk and some others are invasive. Invasive methods require open surgical exploration, histological or direct mechanical measurements and consequently are involved with invasive surgery, animal sacrifice and scaffolds destruction. Therefore, it is preferable to perform non-invasive/non-destructive monitoring such as MRI. Basically, MRI signal is based on the proton density and proton relaxation time differences of an object.

Following implantation of a nerve guide tube, the relaxivity parameters of the adjacent tissues do not change. The reason refers to solidity of the polymeric tube and lack of free electrons within the polymeric structure. In addition to that, the difference between magnetic susceptibility of the tissue and polymer is not adequate to generate susceptibility-induced contrast. Therefore, MRI contrast agents are needed to label the implanted nerve guide tube. The inability to visualize the unlabeled guidance channel *in vivo* is shown in (fig 1.1). Therefore, an MR contrast agent is required. Several magnetic iron oxide-based contrast agents have been approved for clinical use with a few others being at different stages of clinical trials.

One type of contrast agent that has been widely investigated and used in MRI consists of particles with hydrodynamic size larger than 40 nm are called superparamagnetic iron oxide (SPIO). SPIO nanoparticles result in shorter T_1, T_2 and T_2* relaxation times. SPIOs predominately used as T_2 contrast agents, increasing the negative effect on T_2 and T_2* weighted MR images.

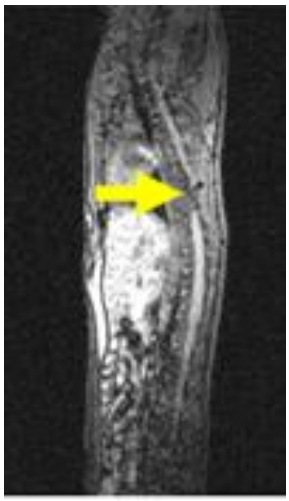

Fig 1. 1 Representative T_2 weighted MR image of transected rat spinal cord. Pointer shows the location of PLGA hollow fiber channel with 0% SPIO

The research was directed towards development of a non-invasive measurement system for monitoring the degradation rate of the polymeric scaffold by incorporating MRI relaxation times. MRI generates spatial maps of T_2 relaxation times that provide further information on the objects being imaged. Accordingly, transverse relaxation time (T_2) was measured for different contrast agent concentration. Material degradation was also followed from MR signal intensity decay and T_2 relaxation times were assessed for their ability to explore polymer structural degradation. The correlation between T_2 relaxation times and concentration of contrasting agent together with variation profile of T_2 relaxation times over degradation period were used to determine the feasibility of MRI for monitoring degradation. This work created an approach for *in vitro* monitoring of the degradable guidance channels with the goal being to allow the future assessment of the degradation of implanted bioengineered scaffolds.

1.2 Thesis objectives

This project is aimed to accomplish the following tasks:

I. To fabricate PLGA HFCs using
   - dip coating
   - vacuum drying
   - CO2 foaming

II. To assess the degradation of PLGA HFCs using MRI non-invasively

III. To investigate the change in morphology of PLGA HFCs using MRI non-invasively

IV. To find the optimum SPIO concentration

1.3 Organization of the thesis

The presented thesis contains 6 chapters. **Chapter 2** is in two parts. 1st part provides an overview of the nerve regeneration strategies highlighting those applicable for SCI specifically degradable nerve guide tubes. 2nd part provides knowledge on physics of MRI, pulse sequences and MRI contrast agents. This chapter ends by a review on MRI applications in tissue engineering. **Chapter 3** describes a novel technique in non-invasive monitoring of the nerve guide tubes and discusses the experimental procedures. **Chapter 4** presents the experimental results. **Chapter 5** deals with a discussion of the results. **Chapter 6** investigates the main conclusions from this research project. Finally, **Chapter 7** outlines the limitations of the project and the additional works that can be pursued in this field.

1.4 Thesis hypothesis

Our hypothesis is that SPIO nanoparticles loaded PLGA HFCs can be monitored by MRI based on the fact that MR signal intensity of the channel will change with degradation. The change of the signal intensity arises from alteration in T_2 relaxation time which is mainly due to two events; the first is due to water penetration in to the polymeric matrix, the second event is the breakdown of polymer molecules in degradable channel and release of SPIO.

Chapter 2- LITERATURE REVIEW

2.1 Nerve regeneration

The nervous system is categorized into central nervous system (CNS) and peripheral nervous system (PNS). The CNS includes brain and spinal cord, and PNS consists of all other nerve fibers that receive signals from the external environment and transmit information to and from CNS. Neurons are the main components of the brain, spinal cord and peripheral nerves. They are composed of a cell body, dendrites and an axon. Neurons are electrically excitable cells that process and transmit information [1]. Nervous system injury can be due to traumatic injury. Since neurons are non-proliferative, any injury to the axons or the cell bodies, which can cause neural death can results in the loss of the functionality. Therefore, injury to the nervous system affects the quality of the patient's life directly. Injury of the CNS and PNS can result in the loss of the function in the muscles and sensory organs. The patient might stay paralyzed below the site of injury for the rest of his life. That's why nerve regeneration strategies for PNS and CNS have received great attention and extensive research efforts have been done in nerve regeneration filed. Due to different reaction of PNS and CNS after injury and because the myelination process of PNS is distinct from that of CNS, the understanding of the differences between these two nervous systems is crucial.

2.1.1 Peripheral nervous system (PNS) regeneration

In the PNS, axons can regenerate and functional recovery of the nerves is possible. Proliferating schwann cells, macrophages, and monocytes remove myelin debris and release neurotrophins, and eventually guide axons towards their synaptic targets and can result in neural function restoration (Fig 2.1)[2].

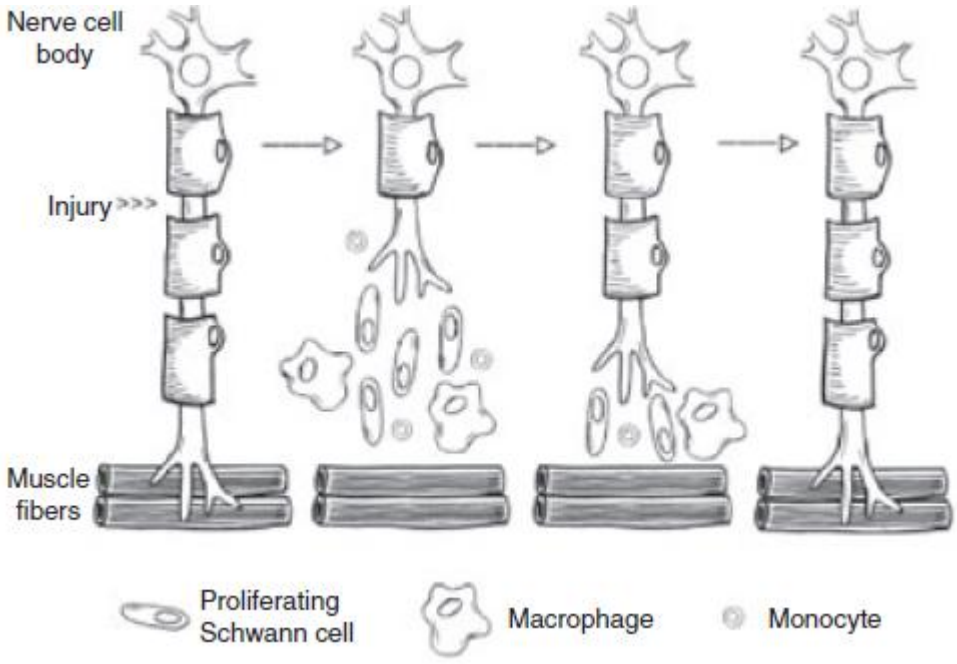

Fig 2. 1 Nerve regeneration process in PNS after injury[3]

For repair, nerves can be surgically sutured end to end. However, this method is effective only for small gaps. For nerve repair when the nerve ends are not directly adjacent, nerve autografts are recommended. Autografts are also known as the "gold standards" for nerve graft repair and have been used widely for PNS repair. In this method a nerve segment is taken from part of the body and inserted back into the lesion area [4].

Variations on the nerve Autograft also include allograft and xenograft. In an allograft, the nerve is taken from another person while in a xenograft it is donated from another species. Although these clinical treatment approaches have shown successful results but they have several disadvantages including multiple surgeries causing functional loss at donor site with regards to autografts, tissue availability, risk of disease transmission, secondary deformities and potential differences in tissue structure and size [5]. To eliminate the need of autografts, researchers have developed guidance channels. Guidance channels are available commercially and can be composed of natural and synthetic polymers[6] and can be resorbable or non-resorbable. Guidance channels can be used for 20-25 mm transection injuries. However, the recovery of longer gaps is considered challenging. There are techniques that improve the functionality of the nerve guides including use of primary support cells (ex. Schwann cells) [7] or stem cells (ex. bone marrow-derived stem cells) [8].

Moreover, several physical or biochemical modifications have been shown to improve the neural repair significantly. Accordingly, Cai et al. showed that presence of internal scaffolds made of synthetic polymer or matrix proteins within the lumen of channel improves its physical and chemical properties [9]. Studies have reported that aligned fibers promote the guidance of axons compared with non-aligned fibers [10, 11]. Dodla et al. on the other hand, demonstrated the effect of gradients of laminin and neural growth factor (NGF) within the nerve guide stimulating nerve regeneration [12]. It was also reported that coating the guidance channel materials enhances the cell attachment, proliferation and migration. For instance, plasma polymerization has been shown to be a reproducible coating method that does not change the chemistry of the bulk material but increases the cell coverage [13].

2.1.2 Central nervous system (CNS) regeneration

Nerve regeneration in the CNS differs from the PNS. During early development, the CNS and PNS contain glycoproteins (laminin and fibronectin) which enhance the axonal growth. In contrast to the PNS, these glycoproteins do not exist when CNS is matured. On the other hand, oligodendrocytes of the CNS produce glycoprotein in the injury site inhibiting the axonal outgrowth. This inhibitor does not exist in Schwann cells during PNS regeneration. Therefore, due to lake of growth factors that overcomes inhibition or inhibition neuralization, injuries in CNS do not spontaneously regenerate. In summary, recovery of the CNS is more complex than the PNS and requires different considerations. None of the conventional strategies for PNS regeneration is effective enough for CNS recovery. Therefore, it is a significant challenge for scientists to repair the injured CNS especially spinal cord. Accordingly, various approach being optimized and tested [14].

2.2 Spinal cord injury

The spinal cord is approximately 1 cm thick and 42 cm long, and is enclosed within the bony structure of the spine. Anatomically, the spinal cord is divided in to four parts: the cervical, thoracic, lumbar, and sacral regions (Fig 2.2). The central region of the spinal cord which is in the shape of a butterfly is called gray matter. This region contains cell bodies of excitatory neurons, glial cells and blood vessels. The gray matter is surrounded by the white matter. The white matter insulates the spinal cord and is composed of axons and glial cells (oligodendrocytes, astrocytes and microglia).

Oligodendrocytes provide myelination for the axons in CNS. Actrocytes and endothelial cells create blood nerve barrier, separating the CNS from blood proteins and cells.

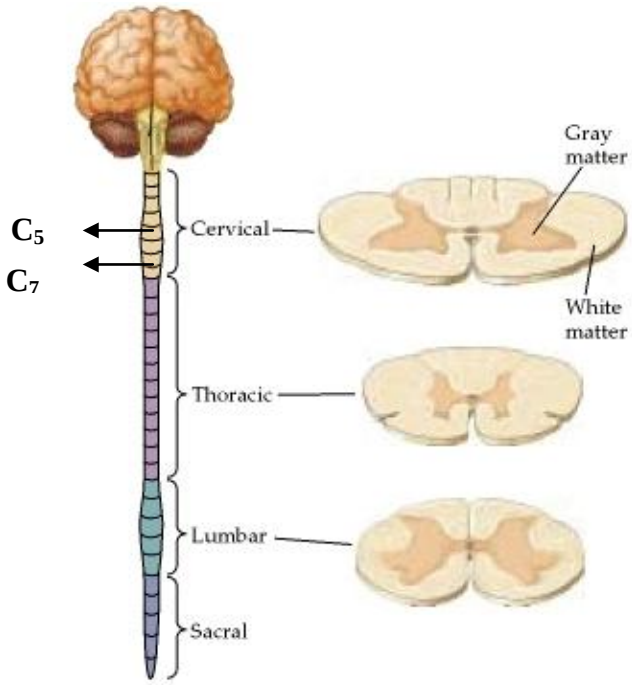

Fig 2. 2 Side view and transverse cross section of spinal cord[15]

It is estimated that about 253,000 people with spinal cord injury are living in the United State, and there are about 11,000 new injuries per year mainly male (82%) and of median age 26 (National Spinal cord Injury Association, 2011). Human spinal cord injury can be classified into two types: open and closed injury. About 27% of human spinal cord injuries are the open injury type. Penetrating objects that tear the spinal tissue cause discontinuity of the spinal cord and is the reason of this kind of injury. However, majority of the spinal cord injuries result in compression injuries of the cord.

According to the literature, spinal cord damage occurs mostly where the spine is the most flexible which is at region C_5-C_7 in the neck area (fig 2.2) [16, 17]. As mentioned previously, spinal cord injury (SCI) is a very complex clinical problem characterized by the inability to repair or regenerate damaged neurons and axons, and the presence of inhibitors for regeneration (fig 2.2). SCI can result in the death of neurons, oligodendrocytes, astrocytes and precursor cells and the creation of cavities and cyst at the injury site interrupting ascending and descending axonal tracts. The axon can undergo demylination and inflammatory cells such as microglia, macrophages, neutrophils and T-cells proliferate into damaged region and can cause loss of axonal connections and failure of motor and sensory function.

On the other hand, the macrophages infiltrate the injury region slower than when they infiltrate the PNS; therefore the removal of the inhibitory myelin will get delayed, resulting in blood-spine barrier. This barrier limits the entry of the macrophages into the injury site. Moreover, cell adhesion molecules in the distal end of the injured spinal cord are not upregulated enough as they are in the PNS, limiting contribution of the macrophages which play an important role in healing of SCI [18, 19]. SCI will progress furthermore following the formation of glial scars.

These scars are formed when reactive astrocytes, glial progenitors, microglia, macrophages schwann cells and fibroblasts infiltrate into injury site (fig 2.3). They contain secreted and transmembrane molecular inhibitors that inhibit the axonal growth. However, few axons can bypass the lesion forming a new circuit with motor neurons via interneurons.

The injury site is then covered by trabecula which contains axon sprouts and eventually, few axons regenerate over a long distance back to their original target. Even though there is some spontaneous regeneration attempt after SCI, it is incomplete[20]. Accordingly, there are several bioengineering and therapeutic strategies have been investigated to promote repair and recovery after SCI.

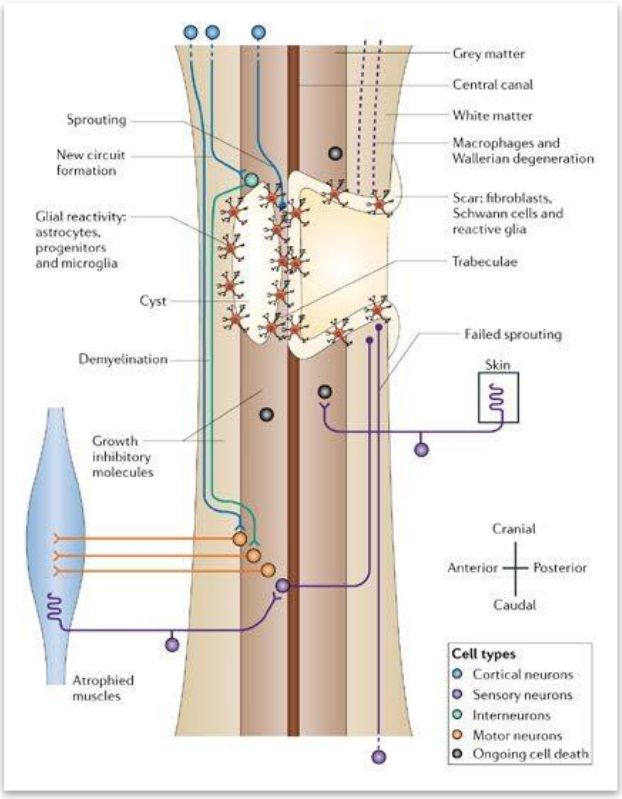

Fig 2. 3 Schematic diagram demonstrating the infiltration of cells into injury site of the spinal cord [20]

2.3 Bioengineered strategies for recovery of spinal cord injury

Recovery of the injured spinal cord is a multi-step process and requires several cellular and environmental considerations. It has been two decades since researchers have found that spinal axons can regenerate. According to the literature, embryonic spinal grafts and peripheral nerve grafts are able to support axonal regeneration in CNS, but the regenerating axons cannot grow back across PNS-CNS transition zone (TZ) effectively[21]. The PNS-CNS transition zone is an irregular but clearly defined interface that separates the CNS from PNS. The TZ contains both central and peripheral nervous tissue. This interface is penetrated only by axons[22]. Hence, researchers are focusing on building a permissive environment which provides physical and chemical pathways for axonal regeneration eliminating the limitations of the previous repair strategies. Accordingly, there are several treatment approaches for spinal cord repair including bimolecular therapy, cellular therapy and nerve guidance therapy [23].

Bimolecular therapy- Neurotrophic factors (neurotrophins) have an important role in neural survival and enhancing axonal regeneration in CNS and sensory axon growth across the PNS-CNS transition zone. There are various neurotrophins that have been investigated for axonal regeneration. Nerve grow factor (NGF), neurotrophin-3 (NT-3), ciliary neurotrophic factor (CNTF) and acidic and basic fibroblast growth factor (aFGF, bFGF) are examples of the neurotrophic factors which have been studied with respect to spinal cord axonal regeneration.

Studies have shown that guidance channles incorporated with NGF and NT-3 increase the neural outgrowth in the spinal cord and the axonal growth across the PNS-CNS transition zone [24, 25]. However, NGF caused sprouting of uninjured sensory axons resulting in chronic pain and improper neural reflexes[26]. CNTF was also showed to promote nerve regeneration; however its application has been shown to provoke glial scarring creating a non-permissive environment for neural growth in spinal cord[27]. FGF has shown to be effective in the regeneration of oligodendroglial lineage and myelin repair in spinal cord. FGF increases neovascularization and formation of damaged blood-brain-barrier (BBB)[28]

Cellular therapy- May different cell types (ex. stem cells) have been studied with respect to spinal cord repair. Stem cells are classified into embryonic stem cells, fetal stem cells, neonatal stem cells (umbilical cord blood cells), and adult neural stem cells (aNSCs). Cellular therapy is based on two directions: restitution of white matter long tracts (regenerative approach) and cell replacement. Cellular therapy is either via intraspinal transplantation of fetal cells or progenitor cells to restore the functional properties of the damaged axons, or through transplantation of oligodendrocytes, olfactory ensheathing cells (OECs) and schwann cells. The later approach is effective when axons are intact anatomically but interrupted physiologically [29]. There are several reports on successful stem cell transplantation into the injured spinal cord. Stem cells have shown to be capable of differentiating into neurons and glial cells[30].

Wang et al, found that the transplantation of Schwann cells into an alginate hydrogel prevented cellular apoptosis and promoted Bcl-2 expression in the transected spinal cord, and enhanced the functional recovery after spinal cord injury[31]. Venkata et al. showed that human umbilical cord blood stem cells (hUCSCs) when transplanted into the injured spinal cord, differentiates into oligodendrocytes and neurons. UCSCs secrete neurotrophin-3 (NT-3) and brain derived neurotrophic factor (BDNT) and assist production of myelin basic protein (MBP) to promote the process of remyelination [32].

Nerve guide therapy- Investigators are now making efforts to used materials (natural or synthetic) in order to stimulate nerve regeneration and provide a guidance pathway for their outgrowth. In the following section nerve guidance therapy will be discussed in more details.

2.3.1 Polymeric guidance channels

When repairing sensory nerves, it would be optimal not to remove a sensory nerve from another part of the body as a source of autograft. Therefore, polymeric guidance channels are used instead. These channels are available in degradable and non-degradable forms and they provide a promising strategy for recovery of SCI [23]. Nerve guide tubes direct the nerve growth from the proximal to distal nerve stump, facilitate the diffusion of the neurotrophic molecules secreted from injured nerve stump and inhibit the ingrowth of scar tissues[33].

Guidance channels are required to have certain characteristics in order to provide the necessary support for the neural cells to proliferate and maintain their functions. There are a variety of natural and synthetic biomaterials and techniques available for nerve guide tube fabrication. The geometry of the channel is of great importance since their architecture defines the final shape of the new tissue[34]. In order to achieve the ultimate goal for repair, specific parameters need to be considered when designing guidance channel.

2.4 Essential properties for guidance channels in CNS

An ideal guidance channel for recovery of SCI possess the following characteristics: 1) Biocompatibility with high affinity for cell attachment and proliferation; 2) an extensive interconnected pores network to allow cells to migrate, multiply and attach deep within nerve tubes and to control the direction of the axonal growth; 3) channels through which oxygen and nutrient are supplied to the cells deep inside the nerve guide and the waste product can be drained away; 4) appropriate mechanical strength and biodegradation behavior; and 5) suitable geometry as requested by the surgeon[23]. There are two main material categories that have been successfully investigated for use in nerve guide tubes fabrication such as 1) natural polymers, 2) synthetic polymers.

Mechanical strength- Guidance channels are required to have mechanical strength compatible with the regeneration of the new tissue. They need to be strong enough in order to prevent collapse that includes repetitive compressive forces, or the degradation of the material by specialized cells in the body like macrophages. However, guidance channels should have enough mechanical strength to maintain the opening of their lumen until nerve regeneration is complete. Studies have introduced several techniques which tune the mechanical stiffness of nerve guide tubes including coil reinforcement, crosslinking and altering material composition[33]. It has been reported that reinforcing the walls of the tubes with coils has a great influence on their mechanical strength. For instance, PHEMA-MMA containing poly(ε-caprolactone) (PCL) coils and chitin tubes containing PLGA coils have shown to be stiffer in comparison with non-reinforced tubes[35]. In contrast, experimental evidences have indicated that reinforcing the walls of the guidance channels makes them rigid and results in negative impact between the implanted tube and the soft spinal cord tissue [36].

The overall goal is to design a guidance channel which promotes regeneration, allowing the cells and their matrix to regenerate and replace the material composition of the tube. Another modification that can be applied in order to change the mechanical strength of nerve tubes is the surface or bulk crosslinking. Studies have shown that crosslinking treatments have an effect on the initial mechanical strength and degradation rate of the nerve guide tubes. For instance, Soichiro et al. showed that non-crosslinked collagen nerve tubes swell after implantation. Therefore they are mechanically unstable. Plus the regenerated nerve tissues in those tubes were restricted.

To overcome this problem, they tested different crosslinking methods such as ultraviolet (UV) irradiation, heating and immersing in glutaraldehyde (GA) on collagen nerve tubes and found that UV irradiation has the best effect retaining the inner space of the collagen tube. UV irradiated nerve tubes also showed to protect the regenerated nerves form any disturbance or restriction [37].

Cell attachment- Cell attachment is another important parameter to be considered when developing a nerve guide tube. This property is necessary in order to mimic the natural environment of nerves *in vivo*. Cell attachment provides contact mediated guidance for tissue regeneration[38]. Most of the synthetic and natural materials that are being used in fabrication of nerve guide tubes are not cell adhesive. Therefore, studies have been focused on modifying these materials, so they become cell adhesive. Generally, cell attachment occurs either via non-specific adhesion or through specific adhesion. According to literatures, factors such as surface roughness, surface topography and surface charge influence non-specific adsorption significantly[39, 40].

There are number of materials such as chitosan and polylysine that have the potential to enhance the cell affinity through non-specific adsorption. Accordingly, It has been reported that coating the chitosan with polylysine or using chitosan/polylysine mixture can facilitate a good neural cell attachment[40]. However, specific cell adhesion has been shown to be more significant in comparison with non-specific adsorption. Techniques are available for specific adhesion to be occurred on guidance channel involve: cross-linking full-length extracellular matrix (ECM) proteins or functional peptide sequences to the surface of the material [41-43].

Studies have shown that precoating the material with ECM proteins such as laminin and neuronal adhesion molecules such as L1-Fc increase the neural cell attachment and nerve regeneration significantly[44].

Porosity- Guidance channels are required to have a porous structure. Porosity affects the permeability and surface area of the nerve guide tubes. The porosity can improve rate of vascularization and clearance of myelin debris resulting in enhanced axonal growth and myelination. The method of fabrication has a great effect on pore size and porosity of the nerve guide tubes [45, 46]. It has been reported that nerve guide tubes with various porosity ranging from semipermeable to macroporous affect the nerve regeneration significantly. The reason is attributed to the availability of endogenous neurotrophic factors and nutrient exchange[47]. Dalton et al produced a hydrogel channels composed of poly(2-hydroxyethyl methacrylate-co-methyl methacrylate) (p(HEMA-co-MMA)) to be used.

The channels were soft and flexible consisting of a gel like outer layer and an interconnected macroporous, inner layer. The porosity was shown to induce great diffusive permeability within channels and promoted axonal regeneration in the CNS specifically spinal cord [36]. In the other study, Cheng et al. fabricated a porous guidance channel for spinal cord recovery. The channel was composed from porous chitosan incorporated with laminin. The porosity in these channls had a great influence on density of cell seeding as well as efficient nutrient and oxygen supply to the cells[48].

2.4.1 Polymeric degradation

Degradable polymers that are utilized for tissue engineering implants are often required to degrade within a certain time frame that is suitable for the tissue regeneration process. Degradable polymers maintain their functional properties under conditions used for a certain time period known as functional time. The duration of the initial degradation of the polymer until its complete degradation is disappearance time.

During disappearance time, the polymer degrades, loses mass and releases degradation products. The functional and disappearance time and the rate of release of degradation products of a polymeric scaffold need to be comparable with the rate of tissue healing in order to achieve its optimum functionality[49]. There are different kinds of chemical degradation mechanism for polymers used in tissue engineering, such as hydrolysis, oxidation, physical and enzymatic degradation. In general, biodegradable polymers degrade or absorb into the physiological environment in which they are implanted.

Natural polymer such as gelatin and collagen degrade via enzymatic degradation when suitable enzyme is available [50]. Synthetic polymers are incorporated with hydrolysable bonds; therefore chemical degradation is one of the most important degradation types[51]. Synthetic polymers that are intended for biomedical applications are degraded through hydrolysis reaction. Biodegradable polymers are composed of repeated monomers held together with bonds such as anhydride, ortho-ester, ester and amide bonds [49]. These bonds undergo cleavage following penetration of water in to the polymeric matrix. The hydrolytic degradation takes place in two types: 1) bulk degradation and 2) surface erosion. (Fig 2.4)

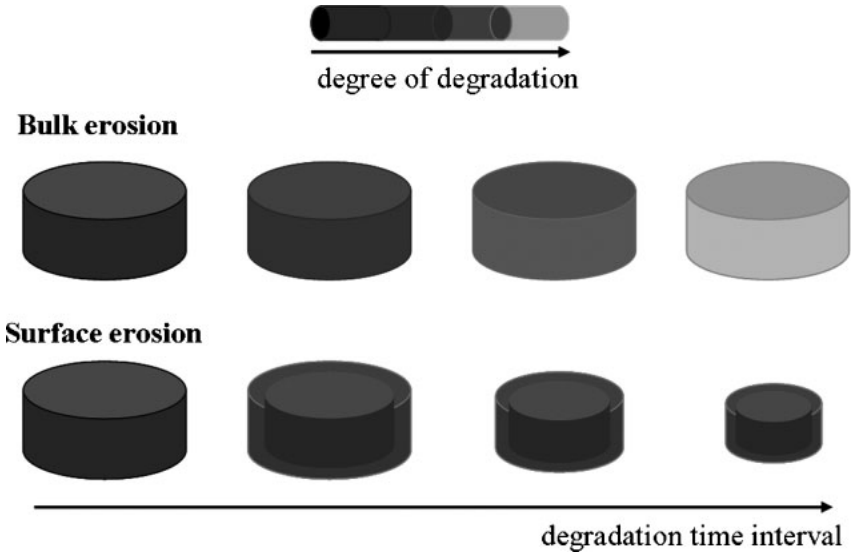

Fig 2. 4 Schematic demonstration of hydrolytic degradation [49]

In the case of bulk degradation, the water uptake takes place faster than polymeric bond cleavage. It means that the polymeric object first absorbs certain amount water and then degradation occurs throughout the bulk. But for the surface erosion the degradation takes place at the interfacial area between polymeric object and the aqueous environment resulting in linear mass loss. This type of degradation proceeds at lower rate compared to bulk degradation. Polymers with anhydride and ortho-ester bonds undergo surface erosion while the other polymers such as polyesters containing glycolic and lactic acid undergo bulk degradation [52-54].

There are several factors affecting the hydrolytic degradation including [49, 55-57]:

- Chemical composition
- Molecular weight
- Morphology (crystalline or amorphous)
- Dimension
- Viscosity
- Porosity
- Impurities (acidic, basic, solvent, monomers, catalyst or drugs)
- Sterilization
- Environment conditions (pH, ionic strength, ion exchange, fluid flow, temperature, buffering capacity)
- Stress and strain applied during degradation
- Manufacturing process

As mentioned previously, when a degradable scaffold is in an aqueous environment, the polymer bonds react with water molecules, breaking up the old molecules and producing new chain ends. This is how degradation process takes place. According to experimental evidences the degradation occurs in four steps including hydration, initial degradation, further degradation and solubilization. In the hydration step, the polymer starts absorbing the aqueous medium that causes glass transition temperature (T_g) decrease and structural relaxation of the polymer.

The degradation begins when the monomer chains are cleaved following water penetration into the swollen polymer. As hydrolysis proceeds, more chain scission and cleavage occur. Thus, the molecular weight of the polymer decreases and reaches the value that the concentration of the chain ends is high enough to catalyze a large number of polymer bonds. The carboxylic polymer chain ends catalyze the reaction between the ester bonds and water molecules[58]. As a result, the polymer will not be able to maintain its integrity anymore and the mass loss begins [59]. The polymer bonds that are in the vicinity to chain ends have a higher chance to be catalyzed comparing to those far from the chain ends. Thus, the degradation proceeds heterogeneously and the concentration of the chain ends accelerates and enhances the interaction between the polymer and water. Consequently, the water uptake increases significantly[60]. The degradation continues to proceed until all the fragments of the polymer are cleaved. Eventually, the molecular weight of the polymer reaches a value that the polymer chains are small enough to become soluble in the incubating media [61].

2.5 Materials design strategies

The selection of material for fabrication of a guidance channel is a fundamental issue in a regeneration strategy. There are varieties of polymeric materials that have been investigated for nerve guide development. These polymers are either natural or synthetic.

Natural polymers can be found in degradable (biointeractive) form while synthetic polymers exist in both degradable and non-degradable (bioinert) form. Non-degradable materials are free of complications such as degradation rate and toxicity of degradation products, but their utilization raises several concerns. These concerns include risk of inflammation and neural tissue compression. Therefore, additional surgical intervention may be required to remove the material. Non-degradable polymers are less adhesive comparing to synthetic polymers minimizing their application in cell transplantation [62, 63]. Degradable polymers on the other hand, have more advantages comparing to non-degradable ones. Due to their degradation, they have lower risk of nerve compression. In contrast with non-degradable polymers, degradable polymers are more adhesive to cells. They also have the potential for the controlled delivery of therapeutic agents as they degrade.

Degradable guidance channels require more complex design; their degradation rates need to meet the regeneration rate and the degradation products must not be toxic but compatible to the body. Degradable guidance channels eliminate the risk of delayed immune response or rejection and the necessity for additional surgical intervention. For these reasons, degradable guidance channels may be more favorable compared to to non-degradable polymers [33, 64] .

2.5.1 Natural polymers

Natural polymers are biological fibrillar protein, such as polysaccharide, or glycosylaminoglycan (GAG) carbohydrates which form hydrogels [65]. They are biocompatible materials and have been used widely in the fabrication of various tissue scaffolds [23]. Natural polymers provide cell attachment and support the cellular functions. They are composed of mesh networks of insoluble polymer fibers so the water can freely flow and result in osmotic swelling or shrinkage of the overall scaffold structure [65-67]. Natural polymers allow appropriate signaling to cells without the need of growth factors. They can be found in both degradable and non-degradable forms. They are non-toxic, non-inflammatory and can avoid serious immune responses.

Natural polymers can be easily shaped to fit the defect. Moreover, since viscoelastic behavior is important for structural and protective function of many soft tissues, the viscoelastic property of the natural polymers make them suitable for soft tissue replacement.[68]. In addition, natural polymers are used in the production of scaffolds for reconstructive/cosmetic surgery applications and bone, cartilage and spinal cord repair implants [23, 68-72]. Natural polymers that are commonly used for neural regeneration include: collagen, agarose/aliginate, chitosan, fibrin, fibronectin and hyaluronic acid (HA). Natural polymers do not have sufficient mechanical strength, and therefore they require extensive modification. In most cases they need to be corsslinked or blended with other structural components such as synthetic polymers. Degradable natural polymers are increasingly being used for nerve guide tubes due to their natural degradation by enzymes secreted in the body [2, 73-75].

Collagen- Collagens are composed of an extended rod of triple helical strands stabilized by hydrogen bonding. Collagens are the most abundant protein in animals. At least twenty-eight types of collagen have been identified. Collagens are favored for several applications such as tissue scaffolding, tissue repair, cancer therapy, cell adhesion and migration [76].

Collagen type I, III and IV are the most commonly used for biomedical applications [77, 78]. Collagens are used for nerve guide tubes in different forms such as porous sponges, gels and sheets. They have been used extensively for both outer tubular structures and central lumens for nerve regeneration [73, 74]. They have a high surface area, softness, and absorbency, and can be fabricated into many product forms [79]. Liu et al. found electrospun nanofibrous collagen to have great feasibility in providing a permissive environment for cellular infiltration and neural growth due to their interconnected pores. They found that collagen scaffolds are effective for inhibiting astrocyte accumulation [80]. Collagens may not have enough mechanical strenght and undergo shrinkage depending on the way they are processed. However, combining other natural materials such as glycosaminoglycan (GAG), chitosan and elastin can enhance the mechanical properties of the collagen nerve tubes significantly [81].

Apart from natural materials, synthetic materials such as poly (glycolic acid) (PGA) and its copolymers with ε-caprolactone can also improve the mechanical strength of the collagen. Yosuke et al. in a study showed that the incorporation of collagen with PGA fibers increased the compression strength and as a result the cell infiltration into the sponge was deeper in comparison with the collagen sponge without incorporation of PGA [82].

Chitosan- Chitosans are the deacetylated form of chitin. Chitosans are suitable materials for nerve guide fabrication. Chitosans are derived from the naturally occurring polysaccharide chitin. They are widely found in exoskeleton of arthropods, shells of crustacean and cuticle of insects [83]. Due to their high T_g and low thermal stability, pure chitosan is unable to melt and they can be processed in solution [84]. Nerve guide tubes fabricated from chitosan have good mechanical strength and support neurite outgrowth [85]. Combining chitosan with other polymers promotes the mechanical and biodegradation properties of this polymer. The presence of two reactive groups (free amine group and hydroxyl group) in the chitosan structure makes it possible for chitosan to combine with other natural polymers such as collagen or synthesized polymers such as PLA and PLGA [86]. For instance, poly (lactic acid) (PLA) was incorporated with chitosan to develop nerve guide tubes using a dip-coating technique which enhanced the resistance to tension and compression [87]. Chitosan has also been used widely as a cell seeding substrate. Zahir et al. developed a neurosphere tube composed of chitosan. The tube was seeded by neural stem/progenitor cells (NSPCs) and implanted in a transected spinal cord. The *in vivo* results showed great survival for NSPCs and differentiation into astrocytes and oligodendrocytes. Their observation also showed that the host neurons were maintained intact in the regenerated tissue bridge within the chitosan tube [88].

Gelatin- Gelatin is derived from collagen by thermal denaturation of physical and chemical degradation. Nerve guide tubes fabricated from gelatin have great biocompatibility and plasticity and provide excellent cell adhesion property. Gelatin tubes are often prepared by dip-coating or injection molding [89-91].

It has been found that the density of the crosslinking gelatin solution is an important factor in adjusting degradation rate and consequently it has an effect on axonal regeneration. A very high degree of crosslinking lowers the degradation rate and results in nerve compression, while too low a degree of crosslinking degree enhances the degradation rate and therefore provokes more of a foreign body reaction [92].

Alginate- Alginate has been used mainly to encapsulate certain cell type increasing the growth rate and cell survival[93]. Alginate is thermally stable, non-toxic and biodegradable, and it has been documented that nerve guide channels made of alginate, are soft and flexible and support the regenerating axons. This natural polymer can easily incorporate neurotrophic factors produced by fibroblast to enhance the axonal growth. Alginate is also capable of encapsulating hippocampus derived neurospheres to reduce immunological response following implantation[94]. Suzuk et al. implanted freeze dried alginate gel into transected spinal cord and found that aliginate stimulate the ingrowth of myelinated and unmyelinated fibers into the implanted hydrogel. Alginate was also showed to stimulate the generation of neural projections across and beyond the gap and form synaptic connections with host neurons [95].

Fibronectin- Fibronectin has been used widely in the fabrication of guidance channels for peripheral nerves and the injured spinal cord providing a substrate to support nerve repair. Fibronectin is also capable of storing nerve growth factor (NGF), neurotrophin-3 (NT-3) and antibodies, and releasing them gradually to injured site.

It was shown that the presence of fibronectin increased cellular attachment, migration and proliferation [96, 97]. Fibronectin is effective in myelination, axonal outgrowth and neural protection [97]. Priestley et al. showed that the implanted fibronectin conduit in the transected spinal cord not only enhanced the directional axonal growth but also supported long distance regeneration. It was reported that various neural elements, mostly axons, were infiltrated in fibronectin mats. The regenerated axons were oriented parallel to the direction of the pores within the conduit [98]. In another study King et al. showed that fibronectin provokes the migration and deposition of the cellular and non-cellular elements. This process results in tissue continuity across the site of the injury site and creates an implant site which contains a large number of myelinated axons [99].

2.5.2 Synthetic polymers

Synthetic polymers have established great success in clinical applications and many are approved for human use by FDA. Synthetic polymers offer a wider scope to develop and control the characteristics of the material. Synthetic polymers have several benefits over natural polymers including unlimited supply and their chemistry, architecture, mechanical strength and degradation rate can be adjusted with respect to their application [100, 101]. They can be found in both degradable and non-degradable forms. So far the synthetic polymers that have been investigated for nerve regeneration are poly (lactic acid) (PLA) [102, 103], poly (β-hydroxybutyrate) (PHB) [104, 105], poly (caprolactone) (PCL) [106, 107], poly (glycolic acid) (PGA) and poly (lactic-co-glycolic acid) (PLGA) [108-110].

PLA- PLA is a biodegradable and non-toxic polymer that has shown promising results in nerve regeneration [111]. It has been reported that the implantation of a PLA single channel tube seeded by Schwann cells effectively promoted axonal regeneration in the transected adult rat spinal cord [112, 113]. Another study showed that macroporous PLA foam with oriented inner channels provides good axonal guidance for defective spinal cords specially in chronic cases [103].

PHB- PHB is a biodegradable synthetic polymer which has shown impact on guiding axonal growth after spinal cord as well as peripheral nerve injury [104, 114]. PHB has a unique trait of a tubular structure with longitudinal oriented fibers. These fibers provide a physical guide for the growing neurons and enhance their alignment [33]. PHB nerve guide channels coated with alginate hydrogel or fibronectin and seeded with Schwann cells has demonstrated promising results in the reduction of spinal cord cavitations and promotion of axonal regeneration across the channel [115].

PCL- PCL is a biodegradable synthetic polymer which has a slow degradation rate; therefore it is receiving a great attention for use in long term implantation [116]. PCL incorporated with collagen has been used to generate a porous network that provides pathways to transmit signaling molecules to and from cells in regenerating nerves [117].

PLGA- PLGA is one of the most successfully developed biodegradable polymers and has specific properties such as, 1) biodegradability and biocompatibility, 2) FDA approval, 3) ability to incorporate with hydrophilic and hydrophobic small molecules or macromolecules, 4) capability to facilitate sustained release of factors, 5) capability to modify surface properties and 6) capability to target nanoparticles to specific organs or cells. PLGA is one of the most commonly used polymers for fabricating tubular guidance structures. This polymer is composed of PLA and PGA. PLA is found in the form of either optically active racemic ($_{L}$- PLA) which is a crystalline polymer or optically inactive stereoregular ($_{D,\ L}$- PLA) which unlike the other form is an amorphous polymer and is more preferable.

The reason is due to the amorphousness of $_{D,\ L}$- PLA which creates inherent irregularities in the polymer chain structure promoting the homogenous dispersion of drugs, growth factors and proteins into the polymer matrix. PLGA degrades through the hydrolysis of ester bonds along its backbone to produce the original monomers PGA and PLA. Under normal physiological conditions, these monomers are by-products of various metabolic reactions in the body [118]. PLGA with lower PLA content has higher degradation rate. And that's due to hydrophobicity of the PLA in comparison to PGA.

In addition to ratio of PLA/PGA there are several other factors that have influence on degradation behavior of PLGA such as, molecular weight, viscosity, crystallinity, tube geometry and size, temperature, pH and the amount of the aqueous incubating media (*in vitro* condition).

2.5.3 Fabrication techniques

There are several techniques that have been used to produce nerve guide tubes, including: electrospinning, injecting molding, dip coating, film rolling, and extrusion (Fig 2.5).

Electrospinning- In this technique, the natural or synthetic polymer is dissolved into an appropriate solvent or melt prior to application of high voltage. The high voltage is used to overcome surface tension and viscoelastic forces and to draw fine fibers (50 nm-30μm) from the liquid polymer. These types of fibers are suitable for the fabrication of guidance channels since they can be made to have a similar morphology to the extracellular matrix of neural tissue. Moreover, the 3D fibrous network derived from the electrospun process can improve neural attachment, migration, proliferation and diffusion[119].

Injection molding- This method can be used for most polymers except for brittle polymers such as PHB. Polymer melts or solutions with suitable viscosities are injected into a special tube shaped mold, forming the desired nerve guide shape after solidification. In this method, a polymer with high molecular weight is required; otherwise a crosslinking treatment is needed.

For chemical crosslinked polymers like collagen, the crosslinking agent is added into mold while for photo crosslinked polymers such as poly (e-caprolactone) acrylates (PCLAs) the transparent mold is exposed to UV light[120].

Dip Coating- In this method a substrate is immersed in the polymeric solution and remains for a period of time during which a thin layer of polymer is deposited on the substrate. The substrate is then pulled out of the solution. The draw rate of the substrate determines the film thickness with the faster it being pulled out, the thicker the film [121].

Film rolling- This technique is suitable for 2D substrates with surface patterns which can be only fabricated by rolling into a 3D nerve guide tube [122]. Sealing is an important process in film rolling method. There are various types of sealing such as heating[123], gluing, fusing, overlapping the ends using organic chemicals [124, 125] or dipping the roll in a crosslinking solution[126].

Extrusion- In this method a single screw extruder is used to fabricate nerve tubes. The outer and inner diameter of the nerve tube is characterized by the nozzle of the extruder and the rod moving spontaneously with the piston [127].

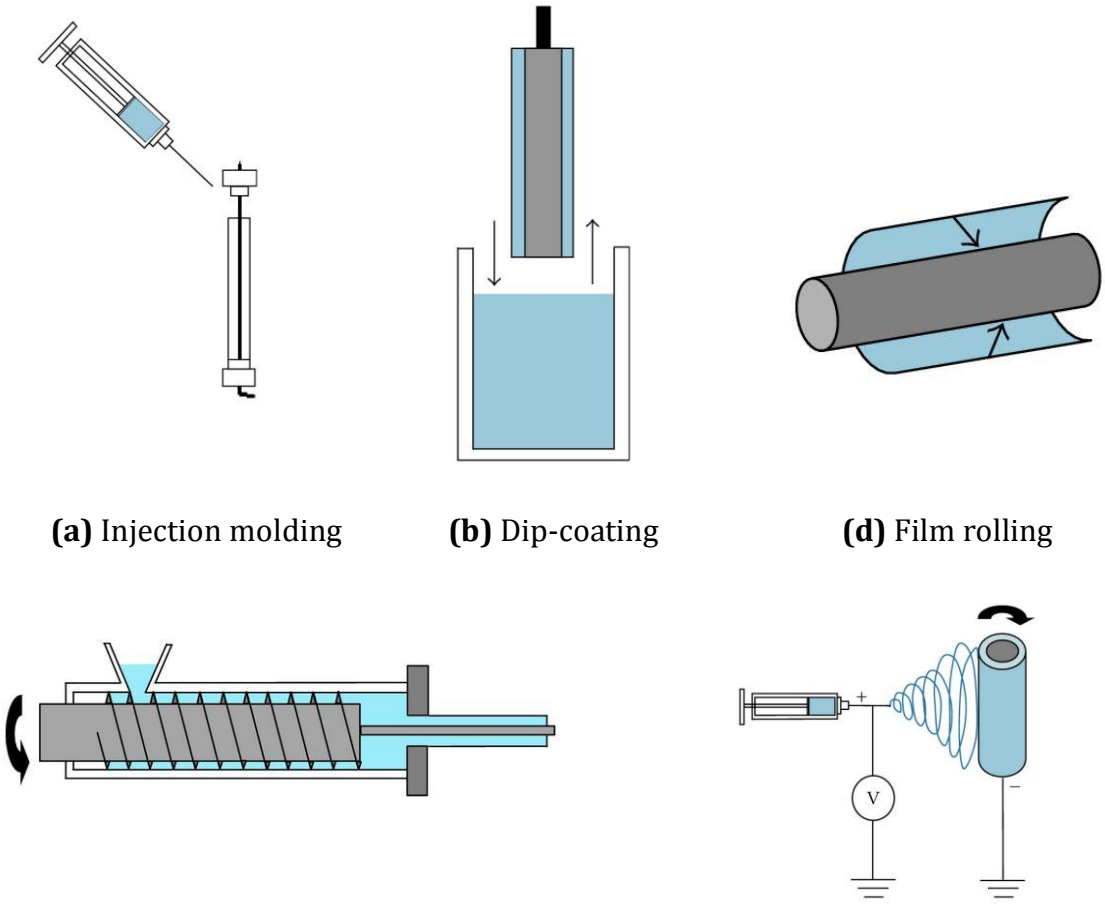

(a) Injection molding **(b)** Dip-coating **(d)** Film rolling

(e) Extrusion **(f)** Electro-spinning

Fig 2. 5 Fabrication methods for nerve guide tubes[128]

2.6 Magnetic Resonance Imaging (MRI)

Nuclear Magnetic Resonance (NMR) was discovered by Purcell and Bloch in 1946[129, 130]. These two scientists were later awarded the Nobel Prize in 1952. However, until 1970 NMR was used for chemical analysis. Later, in 1973 Lauterbur and Mansfield developed a technique based on the principle of NMR to display physical structures, i.e. MRI. Since then MRI technology has been used for medical diagnosis, biomedical, and chemical applications[131, 132]. The conventional MRI machine is composed of different parts including:

- **Magnet-** produces the static magnetic field
- **Shim coil-** creates homogonous magnetic field
- **Radio frequency (RF) coil-** Transmits and receives RF signals to and from the object
- **Gradient coil-** performs spatial localization
- **Shielding coil-** creates magnetic field which cancels the field from primary coil in undesired region
- **Computer-** Constructs images from MR signals

The room where the MRI machine is located should be shielded with Faraday cage. MRI creates high quality images of the inside of human body. This imaging modality is based on spinning protons. In physics, a moving electric charge produces a magnetic field. If the particle moves faster, the generated magnetic field will be stronger. A proton has a certain mass, positive charge and spin. Although a proton does not create high electric field, it does spin fast, therefore generating high magnetic field.

In the body, the source of the protons is water and fat. These particles act like tiny bar magnets and they rotate in random directions. In another word, each proton possesses an intrinsic angular momentum Φ. In the absence of an external magnetic field the spin direction of all hydrogen atoms are random and cancel each other out. When hydrogen atoms are placed in an external magnetic field, all spins align themselves with the external field. Some parallel to the field and some anti-parallel to the field canceling each other out. However, small number of spins will remain parallel to the external field so the net result is an alignment with the external magnetic field (M_Z). The net magnetization vector (M_z) rotates about the external field and its orientation changes (precesses) with a certain frequency proportional to the strength of the field (fig 2.5). This precession frequency is known as Larmor frequency and is defined by:

$$\omega_\varphi = \gamma B_\varphi$$

Where:

γ is gyromagnetic ratio, and

B_φ is external magnetic field strength

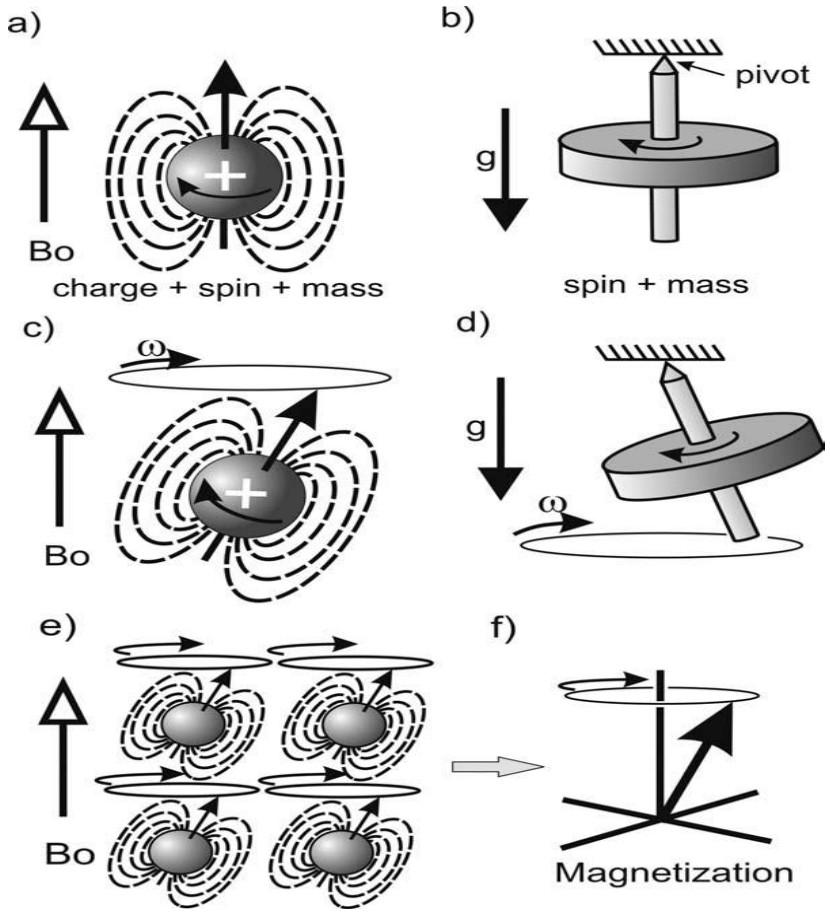

Fig 2. 6 The spin and charge of a proton (a) causes it to have a magnetic field that tends to align with an applied magnetic field B_o (b). When the magnetization vector is tilted away from vertical it undergoes precession (d). The proton also has angular momentum in the form of spin, which will cause it to process at a frequency ω_φ when it is tipped out of alignment with the B_o field (c). A group of spins process in synchrony when exposed to a uniform magnetic field (e), which forms a bulk magnetization (f) represented by a vector that processes at the same frequency[133]

When a radio frequency (RF) with the frequency equal to the larmor frequency is applied perpendicular to the external field (90˚ RF), the protons absorb energy and the magnetization vector (M_z) will be tilted away from z axis while precessing around the external field with larmor frequency. In the absence of an RF coil, the excited spins go from higher energy state to a lower energy state realigning with the external magnetic field B_{φ}. As a result the precession relaxes gradually and Mz returns to its equilibrium state. This return to equilibrium is known as relaxation. During relaxation the proton loses energy by emitting their RF signal. This signal is referred to as the free induction decay (FID) response signal. The FID response signal is detected by a conductive filed coil placed around the object being scanned. Usually, the RF coil which sends the excitation signal acts as both transmitter and receiver (fig 2.6).

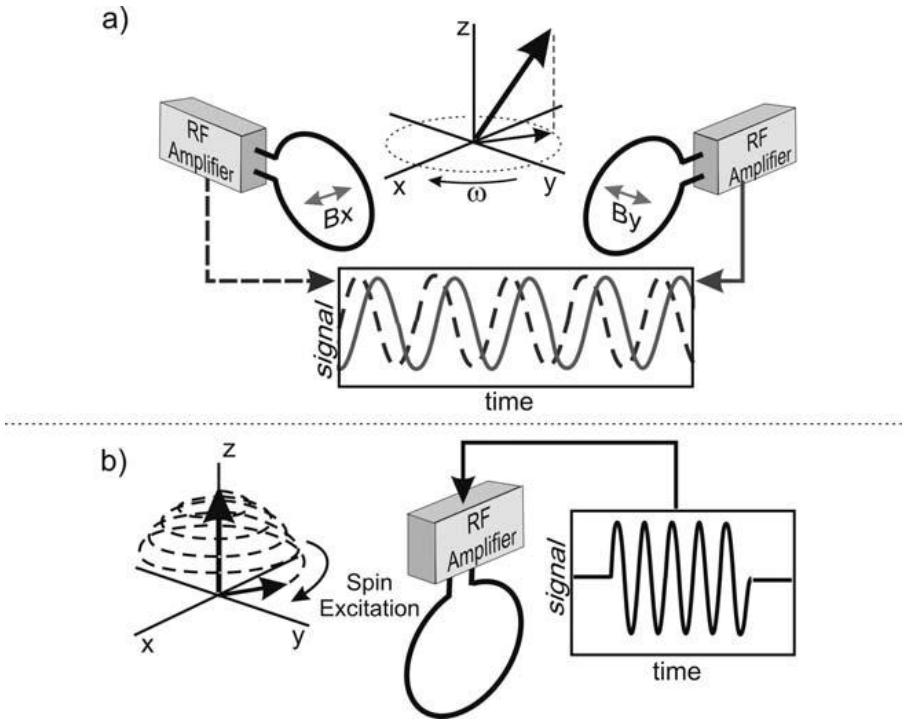

Fig 2. 7 Rotating magnetization induces a signal that oscillates at frequency ω_{φ} via an amplified tuned coil. Two coils placed a right angles sample different phases of the rotating magnetization (a) which can be used to measure the spin phase. Transverse magnetization can be generated by an applied alternating magnetic field at frequency ω_{φ} causing the magnetization to tilt away from the z axis toward the transverse plane (b)[133]

When protons are relaxed, xy-component decays to zero (ie. equilibrium) and z component increases to its original. These relaxations require some time lines know as T_2 and T_1 relaxation time respectively. The concept of these two parameters, how they affect the MR images and MR pulse sequences is discussed in the following section.

2.6.1 T_1, T_2 and T_2* Relaxation Time

T_1 relaxation time indicates the time required for a substance to become magnetized after being placed in an external magnetic field. Alternatively, it is the time needed to regain longitudinal magnetization following a RF pulse. All molecules have natural motion such as vibration, translation or rotation. Large molecules like proteins move slowly while smaller ones like water move rapidly. T_1 is based on the thermal interaction between resonated protons and other protons in the magnetic environment or "lattice". That is why it is so called spin-lattice relaxation time. It is the time during which resonant spins transfer their energy to the environment (fig 2.7). In fact, T_1 reflects the relation between the frequency of these molecular motions and the resonance frequency. When these two frequencies are similar, recovery of magnetization is rapid and T_1 relaxation time is short. When they are different, T_1 relaxation time is long. T_2 relaxation time is a measure of how long resonating protons rotate in phase after application of an RF pulse (fig 2.8).

In contrast with T_1 relaxation time, T_2 decay does not contribute to energy transmission. It is mainly due to magnetic interaction between spinning protons. T_2 relaxation time indicates the time that transverse magnetization would last in a uniform external magnetic field. T_2* is another MRI time constant that includes the loss of phase coherence as a result of field inhomogeneities and susceptibility effects. In reality there are several factors that result in imperfection in the homogenous magnetic field. The MR magnet may have defects in its manufacture which can generates inhomogeneity [133].

Every tissue has a different magnetic susceptibility that can result in distortion of the magnetic field at tissue borders especially at an air/tissue interface. Moreover, metal objects such as implants can also alter the magnetic susceptibility. All these factors lead to increase or decrease (non-uniformities) in local regions of the external magnetic field. Local filed non-uniformities make the protons to rotate at slightly different frequency following 90˚ RF pulse [134]. Hence, the proton loses coherence and transverse magnetization returns back to zero. This will result in both T_2* and T_2 relaxation times.

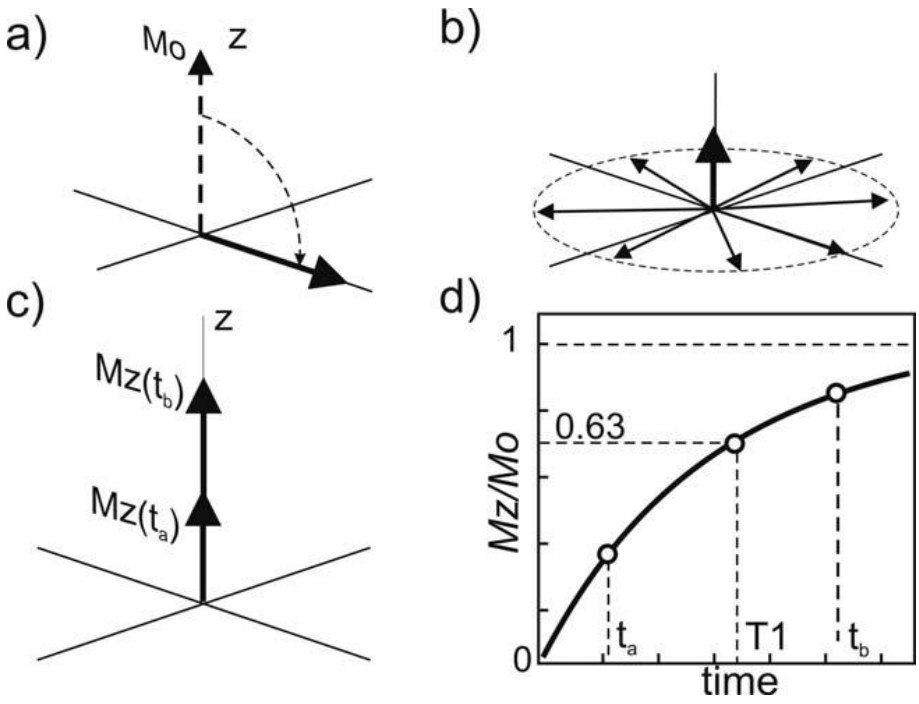

Fig 2. 8 Spin-lattice or T_1 relaxation. After a 90˚ RF pulse, magnetization is tilted into the transverse plane (a) after which it undergoes transverse relaxation and signal loss (b) and a gradual growth of longitudinal (M_z) magnetization with time (c). This results in a curve of M_z with time which is characterized by a relaxation time constant T_1, defined as the time to reach 63% of its equilibrium value (d)[133]

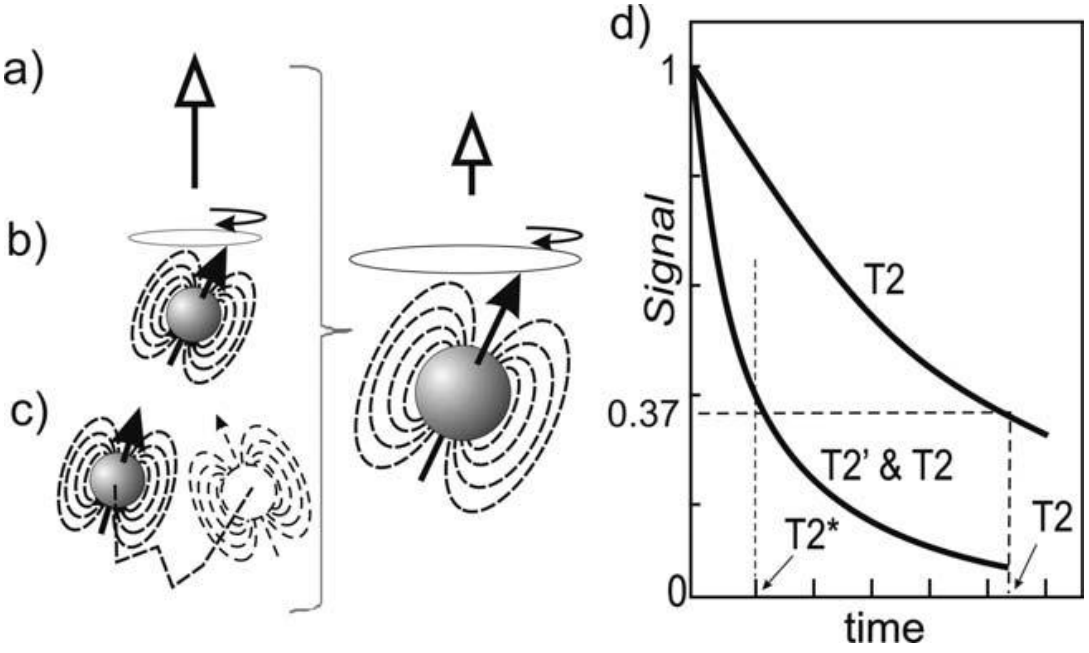

Fig 2. 9 Factors that lead to T_2* relaxation. Static field variations in space due to tissue susceptibility variations (a). In addition, random interactions between the magnetic properties of spins themselves (b) and their random motion through regions of different magnetic fields (c) will result in additional loss of signal. Random mechanisms are responsible for decay characterized by T_2 while the addition of static field variations leads to faster signal loss as characterized by T_2* (d)[133]

2.6.2 MRI mapping

Due to composite nature of the MR signal, direct quantification of T_1 and T_2 relaxation times using the raw MR images is not feasible. To get T_1 and T_2 information, a serious of raw MR images with different acquisition parameter is required. These raw images are used to perform multi-parameter curve fitting analysis based on mathematical functions that explains the corresponding physical process. This can be done pixel by pixel, creating a "map".

The signal intensity of each pixel is such that a map reflects the calculated relaxation times. Therefore, these maps demonstrate the T_1 and T_2 properties in a quantitative manner.

2.6.3 Spin-Echo pulse sequence

A pulse sequence is composed of series of RF pulses, gradient applications and intervening time periods. Pulse sequence is essential MRI because it is responsible of refocusing dephased spins. Otherwise, there is no sufficient signal to generate an image. A pulse sequence removes the inhomogenity effects of the external magnetic field, and generates a MR signal or echo that provides information about T_2 relaxation characteristics of a certain tissue. It also controls the echo time (TE) and repetition time (TR) to create different kind of contrast. A pulse sequence rephases the dephased spins by: applying a 180˚ RF pulse, or employing a gradient.

There are various types of MR pulse sequences such as, spin echo, fast spin echo, inversion recovery, STIR and FLAIR. Spin echo is one of the most applicable pulse sequences. The mechanism of spin echo is as follows: First a 90˚ RF pulse is applied and the existing longitudinal magnetization vector is flipped from z axis to transverse xy plane. However, spins experience an increase or decrease in their processional frequency produced by magnetic field inhomogenities. Therefore, they precess either more slowly or more quickly. The second step in the spin echo pulse sequence is application of a 180˚ RF pulse.

This RF pulse is responsible of repahsing the spins. Following the application of RF, spins that were precessing faster will be positioned behind those that are precessing slower. As a result, all dephased spins will precess with the same frequency and the coherent signal in the receiver coil is regenerated. This regenerated signal is called "echo". Whenever, a 180˚ RF pulse is applied, a spin echo is produced and rephasing mechanism takes place. The conventional spin echo sequence is found in two forms based on how many times the spin echo signal is produced. It can either single spin echo or dual echo.

Single spin echo contains a 90º RF excitation pulse followed by only one 180º RF pulse. This pulse sequence generates a single spin echo and it is mostly used to create T_1 weighted images. T_1 weighted images have a short TR and short TE. TR and TE are two important parameters which determine the contrast of the MR images. TR (repetition time) is the time between one 90º RF pulses to the next 90º RF pulse in a particular slice. TE (echo time) is the time between the 90º RF pulse to the midpoint of spin echo. A dual echo sequence is composed of two 180º RF pulses and as a result there are two spin echoes. The first echo has a short TE and long TR and produces proton density weighted MR images. The second echo has a long TR and long TE and results in T_2 weighted images. Spin echo is one of the basic pulse sequences used in MRI and is available on all MRI systems. This pulse sequence provides good image quality but requires a relatively long scanning time. Last but not least, spin echo is considered as a gold standard for image contrast and weighting.

2.6.4 MR contrast agents

MR images in some cases may not have adequate contrast; therefore, it is hard to differentiate various tissues which eventually lead to poor clinical diagnostic capabilities. Currently, contrast agents are being widely used to improve MR image contrast [135-139]. Contrast agents are chemical compounds which highly affect the relaxation times of the hydrogen molecule by creating magnetic susceptibility in the local magnetic field and shortening the hydrogen relaxation times. Contrast agents are classified into positive or negative agents. Positive contrast agent enhances the signal intensity and appears as a bright area on T_1 weighted images. Paramagnetic contrast agents such as gadolinium (Gd) and manganese (Mn) are examples of positive contrast agents. They have a similar effect on T_1 and T_2. However, since T1 of tissues is higher than T_2, the effect of these contrast agents at low concentrations is mainly the reduction of the T_2 relaxation time. Superparamagnetic nanoparticles such as magnetite (Fe_3O_4) are a class of negative MR contrast agents that generate spin-spin relaxation effect due to induced field inhomogenity. Negative contrast agents result in reduction of signal intensity. Therefore, thet appear as a relatively dark region by shortening T_2 and T_2* [139].

MRI contrast agents have a large number of applications such as:

i. Diagnosis of brain and spin disorders [140-143]
ii. Detection of tumor, cancer cells and metastases [144-146]
iii. Visualization of the of defects and lesions in the internal organs (ex. liver) [147]
iv. Molecular and cellular imaging, imaging of the fate of the implanted cells [148-151]
v. Assessment of regenerated tissue [152, 153]
vi. Drug delivery [154-157]

2.6.5 Super paramagnetic iron oxide (SPIO)

SPIO nanoparticles have been widely used in medical diagnostic and therapy. SPIO nanoparticles are composed of two components: an iron oxide core and a hydrophilic coating. The iron oxide core consists of magnetite (Fe_3O_4) and/ or maghemite (Fe_2O_3). Oxidation of SPIO results in Fe_3O_4 conversion to $_{\gamma}Fe_2O_3$. Despite similar magnetic properties of Fe_3O_4 and Fe_2O_3, the later one has a lower saturation magnetization. When paramagnetic materials are introduced to external magnetic field, their atomic magnetic dipoles align themselves with the external field while in the absence of magnetic field they are randomly oriented (due to Brownian forces). Paramagnetic materials have a small positive magnetic susceptibility strengthening the magnetic field they are in. SPIO has a single crystal domain and its entire crystal aligns with the external magnetic field generating a large susceptibility[158].

When SPIO nanoparticles are placed within external magnetic field, their moments align parallel to direction of the field increasing the magnetic flux. SPIOs generate local magnetic field interruption and therefore result in rapid proton dephasing producing a detectable variation in the MR signal. SPIOs reduce T_1 and T_2 relaxation time significantly [159, 160]. However, when the external magnetic field is removed no magnetic is remained and due to Brownian forces the orientations of SPIOs will be randomized. Parameters such as diameter and surface characteristic of SPIO are important for cellular response, toxicity and removal from body. Studies have shown that polymer coated SPIO increase the cell viability significantly. For instance, dextran coated SPIO showed to influence the cell viability and has been shown to not have serious side effects [161].

SPIO nanoparticles have been used specifically in various fields such as liver and spleen imaging, cancer imaging, macrophages imaging, cardiovascular imaging, lymph node imaging, protein and enzyme detection and cell tracking.

2.6.6 MRI in tissue engineering and drug delivery

MRI has been used widely in stem cell therapy in heart, liver, kidney, bone, cartilage and central nervous system [162-164]. This imaging modality can acquire images of soft tissues with 100μm resolution[165]. Studies have shown that it is possible to visualize targeted implantation, track cellular migration and proliferation, and monitor the cell-host interaction and any adverse impacts on host vasculature and parenchyma using MRI.

Stuckey et al. used an 11.7T MRI to monitor heart scaffolds non-invasively for the first time. Three different materials were investigated in the study including poly(cyglycerol sebacate) (PGS), poly(ethyleneterephathalate)/dimer fatty acid (PED) and TiO_2 reinforced PED. They found that implanted scaffold appeared as signal voids (dark) and the reason refers to the solidity and water impermeability of the scaffolds.

The same study also showed that due to the strong contrast between scaffold and surrounding tissue, the size of the scaffold could be quantified. Accordingly, they measured the signal void induced by scaffolds over 6 weeks and found that there was a significant change in the size of PGS indicating a rapid degradation while there was no change for PED-TiO_2. These findings were confirmed by histological results. These results showed the feasibility of MRI for non-invasive monitoring of the scaffolds location, size and degradation [166].

In another study done by Terrovitis et al. mesenchymal cells (MSCs) labeled with SPIO (ferumoxide) were seeded on a collagen scaffold. An 1.5 T MRI was performed weekly to calculate T_2 relaxation times. They showed that ferumoxide did not lead to any adverse effect and remained preserved during 4 weeks of scanning. The labeled cells emerged as regions of signal voids in T_2 weighted images. The *in vitro* results showed that T_2 relaxation times were 40% to 50% shorter in ferumoxide labeled cells. This study illustrated the ability of MRI to monitor the seeded cells on scaffold *in vitro*. However, since *in vivo* implanted cells encountered high pressure and other *in vivo* circumstances, further optimization is required for this study to be applicable *in vivo*[167].

Obenaus et al. performed high field MRI to assess the viability, migration, proliferation and location of the iron oxide labeled neural stem cells (NSCs). This study group reported that cell proliferation index (CPI) can be calculated using the volume of T_2 hypointensity [168].

Ko et al. showed that it is possible to evaluate the cellular behavior after transplantation non-invasively. Mesenchymal stem cells (MSCs) were labeled with SPIO and suspended within agarose gel. An 1.5T MRI was performed for different concentrations of SPIO. The corresponding results showed that increasing SPIO concentration results in enhancement of MRI contrast (fig 2.10). In the second part of this study, the labeled MSCs were seeded into gelatin sponges with different thicknesses and then scanned by MRI. The results were similar to previous group demonstrating the effect of SPIO labeled MSCs on MRI contrast (fig 2.11).

The labeled seeded gelatin sponges were displayed as dark comparing to unlabeled ones regardless of their thickness. Comparing MRI data with histological results showed that the darkness observed in MR images were larger than the dimension of the total cells in a sponge. The reason was related to the "blooming effect". Blooming effect is produced when the magnetic susceptibility of the SPIO particles effect a region larger than the actual size of the particles. Therefore, the displayed region containing SPIO is enlarged[169].

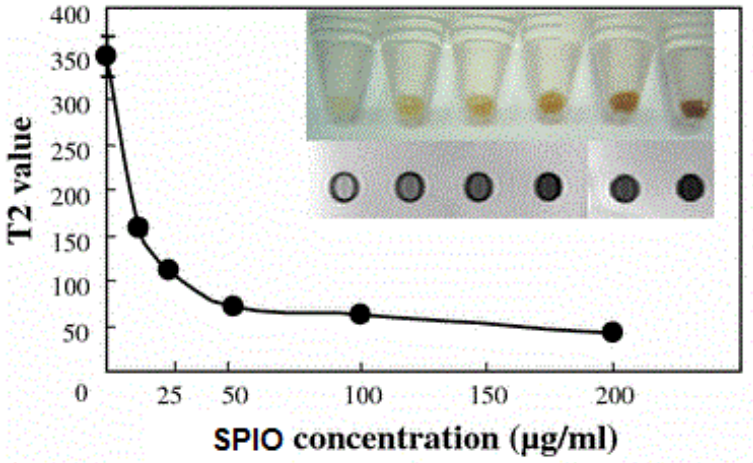

Fig 2. 10 Variation of T_2 relaxation times for different SPIO concentration[169]

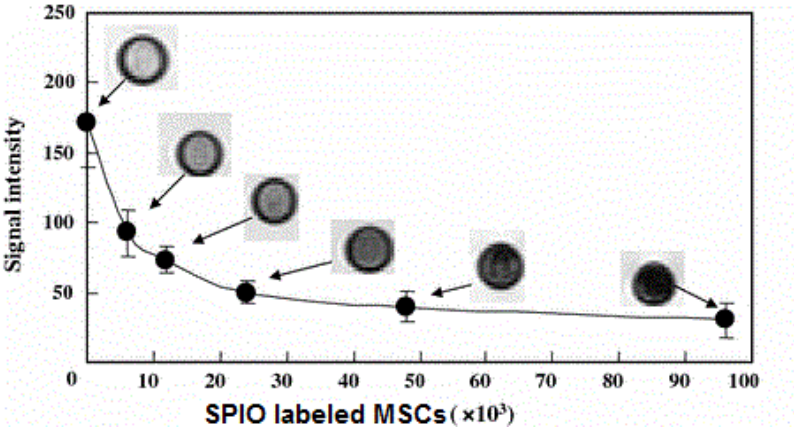

Fig 2. 11 In vitro relaxometry of SPIO labeled MSCs[169]

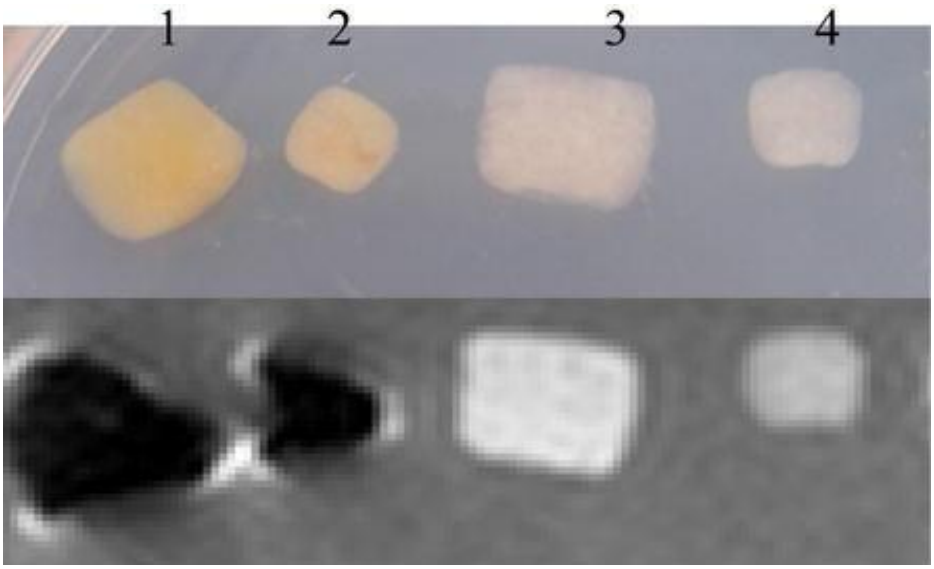

Fig 2. 12 MR image obtained with a fast spin echo sequence from SPIO labeled MSCs in a sponge of 5 mm^3 (1) and 3 mm^3 (2) and unlabeled cells in a sponges of 5 mm^3 (3) and 3 mm^3 (4)[169]

Similarly, Saldanha et al. used MRI to track MSCs labeled with iron oxide particles and seeded in 3D hydrogel scaffolds. The hydrogel scaffolds were used for articular cartilage regeneration and iron oxide labeled MSCs appeared as signal voids on MR images due to signal loss [170].

Marie et al. found that using high resolution MRI; it is possible to visualize the internal structure of the tissue scaffold. For this purpose, polysaccharide based hydrogel scaffolds were fabricated with different internal structures such as macroporous, microporous and lamellar. The scaffolds were infused with gadolinium (Gd) and high resolution 1.5T MRI was performed.

The results showed that the Gd-dopped medium appear as enhanced signal intensity regions, whereas the regions with low intensity showed the presence of structured scaffold (fig 2.13). The MR spatial resolution in this study was very high (~ $30\mu m^3$). This high resolution was obtained using a high temperature superconducting yttrium barium copper oxide detection coil which has high signal to noise ratio comparing to conventional room temperature copper coil. In the same study, the polysaccharide scaffolds were seeded with iron labeled MSCs; and they found that the signal loss on the scaffold was in correlation with the number of seeded cells and their iron loaded [171].

In another study, Zhang et al. developed a method to evaluate the intrahepatically transplanted islets labeled with SPIO (Feridex)[172]. MRI also was used in monitoring SPIO labeled pancreatic islets transplanted in to liver. The purpose of this study was to detect the allergenic rejection following the transplantation[173].

Cheng et al. performed a 1.5T MRI to evaluate the development of tissue in a bladder ACM-based regeneration model. According to their investigations, an increase of T_2* could be an indication of cell filling of matrix pores. Also scaffolds with larger pores exhibited a larger T_2* relaxation time, since large pores allow more water absorption. The study showed the feasibility of MRI in monitoring tissue development[174].

One of the limitations of the current therapeutic treatments is the incapability of drugs to reach a desired region in the body. There are several methods to monitor the drug delivery MRI has also been recognized as a non-invasive monitoring method for drug delivery agents.

In this regard, Ling et al. used PLGA-based superparamagnetic nanoparticles as a delivery system that carries diagnostic agent for malignant brain glima. T_2 weighted MR images showed that T_2 signal intensity decrease with increasing iron concentration[175].

Overall, applications of MRI is not only limited to visualizing internal organs. This imaging modality is capable of tracking transplanted cell, evaluating drug delivery, monitoring implanted scaffolds and the cellular behavior around the scaffold non-invasively[176].

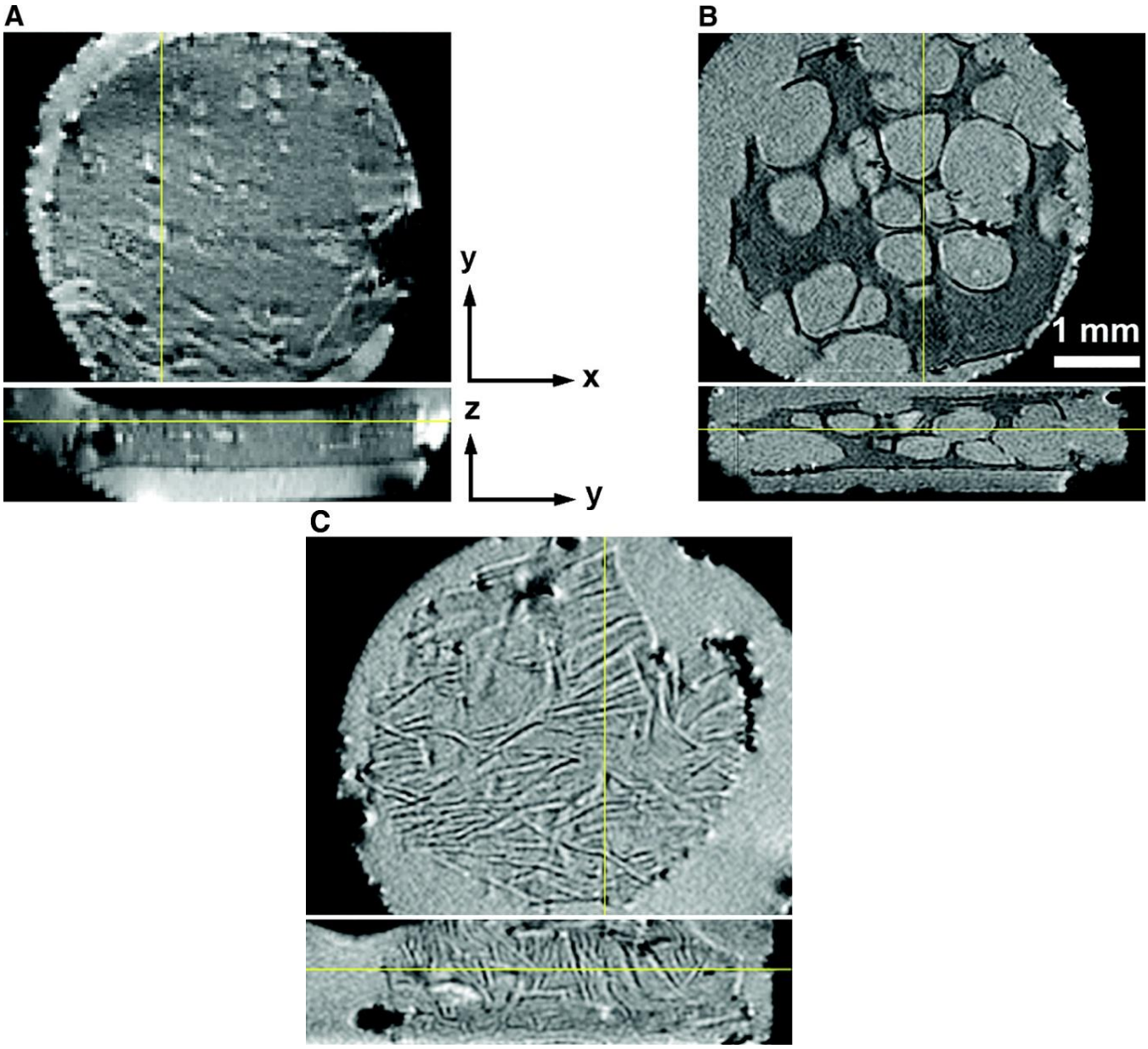

Fig 2. 13 High-resolution 3D MRI of hydrogel scaffolds with different internal structures. Transverse and longitudinal slices are shown. Slice location is marked by a line. Gadolinium-doped hydration medium is seen as areas of enhanced intensity, whereas areas of reduced intensity indicate the presence of structured scaffold. (A) Microporous scaffold: MR image reveals porous architecture with small quasispherical cavities. (B) Macroporous scaffold: MR image shows a highly porous structure with large pores whose outlines are clearly visible. (C) Lamellar scaffold: MR image reveals a 3D lamellar structure [171]

Chapter 3- Materials and methods

3.1 Materials

Poly($_{D,\ L}$-lactide-co-glycolide acid) pellets of $_{D,\ L}$-lactide/glycolide ratio of 50/50 with an Inherent Viscosity range (IV. range) of 0.95–1.2 dL/g. were obtained from LACTEL Absorbable Polymers(Durect corporation, Birmingham, AL, USA) . Chloroform was purchased from VWR International (Ville Mont-Royal, QC, CA). Dry carbon dioxide (CO2) was supplied by BOC (Ottawa, ON, CA) and glass rods with outer diameter 3 mm were obtained from Pegasus Industrial Specialties Inc. (Cambridge, ON, CA). Phosphate buffered saline (PBS) tablets were obtained from MPBiomedical LLC. (Montreal, QC, CA). Fifty mL centrifuge tubes were purchased from Fisher Scientific (Ottawa, ON, CA).

3.2 Fabrication of PLGA hollow fiber channel

To prepare the 20 % (wt/v) PLGA solution, PLGA was dissolved in chloroform. the five layers PLGA hollow fiber channel was fabricated by the dip coating method (fig 3.1). The glass rod was dipped into the solution and dried for 3 hours horizontally using BDC 2002 digital driller (VWR International, Ville Mont-Royal, QC, CA) at a speed 250 rpm to avoid the formation of bubbles, prior to coating of another layer on top. This process was repeated 5 times in order to achieve 5 layer channels with an inner diameter 2.8 mm and a wall thickness of 0.4 mm. The dimensions were specified with respect to the rat spinal cord.

Following the dip coating process, the solvent removal was done by drying the polymer coated glass rods for 8-10 days in a vacuum chamber, at gauge pressure of -24 kPa and room temperature.

3.3 Sub-critical CO_2 foaming

The dried channels were placed into cylindrical Teflon molds while they are still on glass rods and caped at both ends to ensure the final accurate dimensions for the channels (fig 3.1). To foam the channels, the loaded molds were soaked into a CO_2 stainless steel chamber at a pressure of 5.6 MPa at room temperature (25˚C) for 8 hours (fig 3.2). After foaming process, the channels were kept in the mold for another 8 hours at normal atmospheric pressure. In this stage, the CO2 molecules diffuse out of the channels due to thermo dynamic stability forming numerous pores in the polymeric structure of the channels.

Fig 3. 1 Teflon molds (left), Vacuum dried PLGA channels within Teflon molds prior to CO2 foaming process (right)

3.4 Preparation of SPIO nanoparticles loaded PLGA channels

PLGA (20% wt/v) solution with different concentration of Fe_3O_4 (0.05%. 0.1% and 0.2%) were prepared. To fabricate SPIO loaded PLGA channels, the dip coating and foaming process was done as described previously. The channels were stored in -80˚C preventing them from degrading until used.

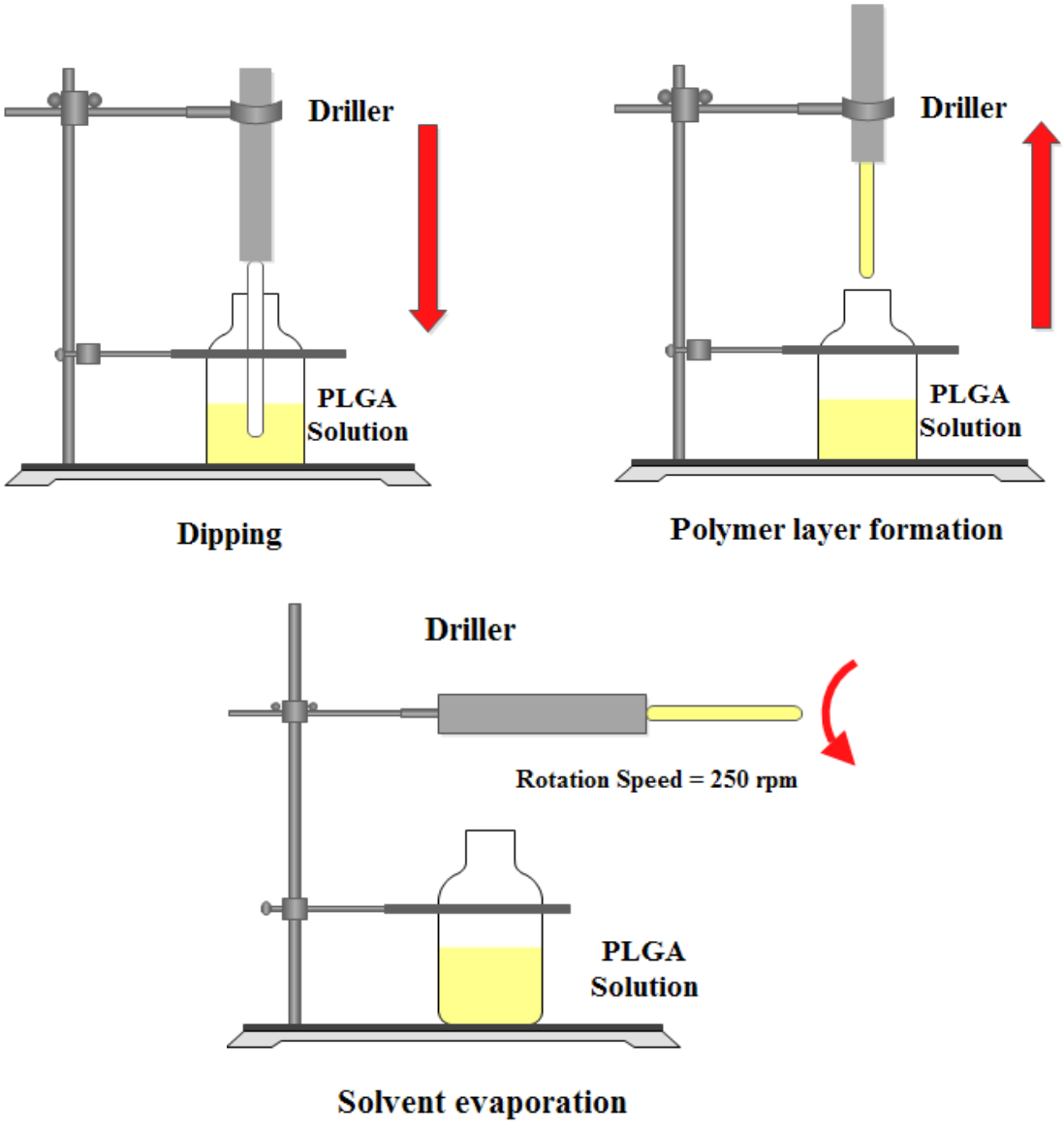

Fig 3. 2 The schematic diagram of Dip Coating process

3.4 *In vitro* degradation

To provide a medium with good chemical stability, PLGA channel was immersed in 50 mL of PBS solution with the physiological pH pH 7.4, and incubated at 37˚C. PBS solution was prepared from dissolving one PBS tablets in one litter distilled water. The medium was replaced by fresh PBS solution every 24 h to keep the pH value constant for the entire degradation period. This study was carried out using both plain and iron loaded PLGA channels.

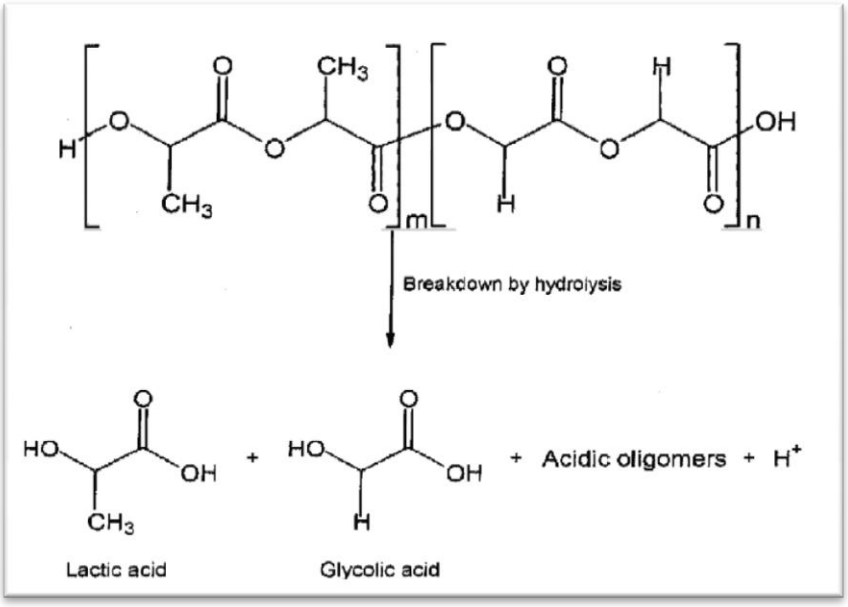

Fig 3. 3 Hydrolytic degradation of PLGA

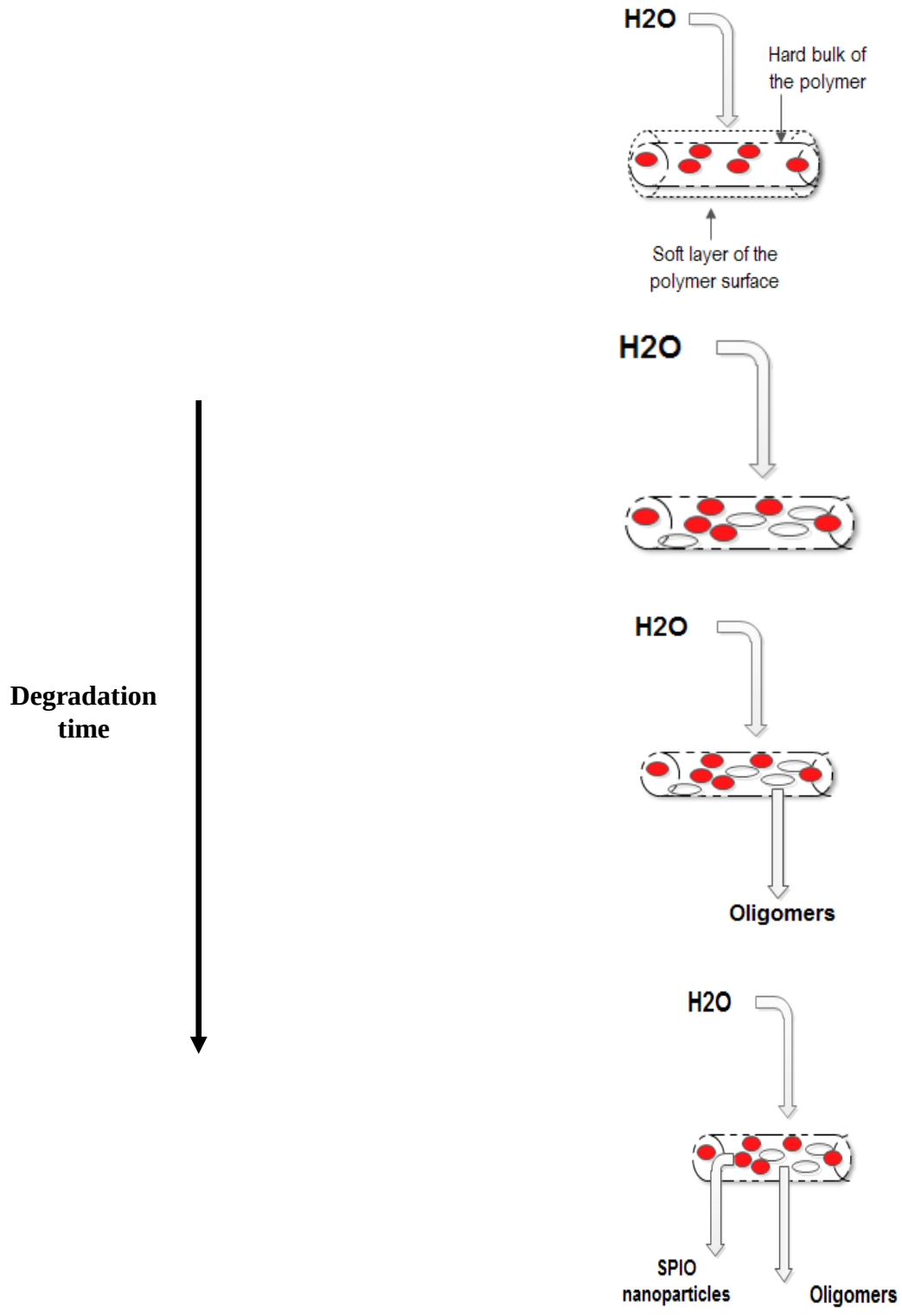

Fig 3. 4 Schematic diagram of SPIO loaded PLGA (50:50) hydrolytic degradation in 50 mL PBS at 37ºC

3.4.1 Mass loss and water uptake

Plain PLGA channels were taken out from PBS every week and weighted using a digital balance to obtain the wet mass, m_w. The channels were freeze dried then for 48 h and weighed. The dry mass was described as m_d, and the initial mass was identified as m_o. The initial mass is the mass of the channel prior to incubation.

Mass loss of the porous channels was calculated by following equation:

$$\text{Mass loss} = (m_o - m_d)/\, m_o \times 100\ \%$$

The percentage of the water uptake during degradation was calculated as:

$$\text{Water uptake} = (m_w - m_d)/\, m_d \times 100\ \%$$

3.4.2 Magnetic Resonance Imaging (MRI) monitoring

PLGA channels with iron concentration ranging from 0% to 0.2% (i.e. 0%, 0.05%, 0.1%, and 0.2%) were scanned on a weekly basis using 1.5T MRI (Siemens, Erlangen, Germany). The channels were in PBS during the MRI scan. For T_2 relaxation times and T_2 map calculations, a series of spin echo (SE) sequences was applied with an excitation pulse of 90˚ and refocusing pulse of 180˚. There was 24 echo times (TE) ranging from 13.3 to 314.4 ms and the constant repetition time (TR) was 4000 ms. The Field of view (FOV) was 210 mm and the image resolution was 256×256 with 4 times averaging. T_2 mapping was computed using in-house algorithm developed in Matlab.

Least square fit was used to find the slope of the decay curve by plotting log intensity on the y-axis and echo time on the x axis and the average T_2 values were calculated and tabulated. Levenberg-Marquardt algorithm was used to solve the resulting nonlinear least square problem. The T_2 weighted images of the channels were obtained with fast spin echo sequence with a matrix size of 512×512 TR of 3000 msand TE of 20 ms. The relaxation decay was modeled using the following monoexponential fitting function:

$$S_{(t)} = S_{t=0}\ e^{\frac{TE}{T_2}}$$

Where,

$S_{(t)}$ represents the signal intensity at time t

$S_{t=0}$ is the signal intensity at the moment of magnetization creation

TE is the echo time

T_2 is the relaxation time

3.4.3 Scanning Electron Microscopy (SEM)

Plain PLGA channels were gold sputter coated and the pore morphology, pore size, pore density and level of interconnectivity were observed using scanning electron microscope (Tescan Vega-II XMU VPSEM). The SEM visualization was carried out every week until end of degradation period.

3.4.4 Statistical analysis

All experiments were conducted in triplicate and the acquired data were expressed as mean ± standard deviation.

Chapter 4- RESULTS

The desired thickness of PLGA hollow fiber channel was acquired via dip coating technique. The final shape (fig 3.2) was obtained after foaming process using by sub-critical CO_2.

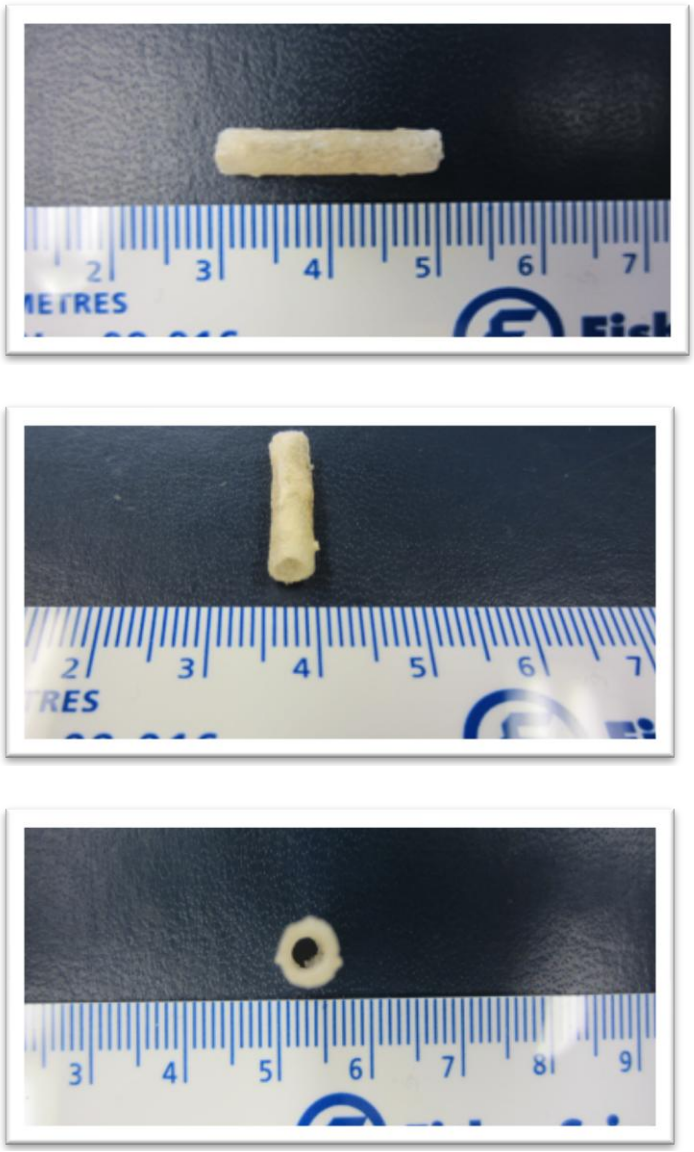

Fig 4. 1 PLGA hollow fiber channel

4.1 Mass loss

The mass of the channels did not change significantly until Week 4. During this time period PLGA channels were in hydration state. From Week 4 to Week 5, the channels showed sudden mass loss. This evidence was due to the cleavage of the backbone chain of the polymer. As a result of polymer cleavage, the channels were unable to retain their integrity. Therefore, they started to lose mass significantly. Along with progress of hydrolysis reaction, more polymeric chain session occurred. Therefore, the number of carboxylic ends groups in the PLGA chains increased. Consequently, more mass loss was observed. PLGA channels continued losing mass until end of degradation period (fig 4.1).

4.2 Water uptake

Considering the water uptake measurement results, PLGA tubes were found highly water absorbable. Water uptake was 109% at the first week. This value remained constant until Week 4. At Week 5, water absorption increased to 137%. The sudden increase in water absorption caused the hydrolysis reaction to accelerate which resulted in rapid mass loss. Due to the accumulation of the hydrophilic products inside the polymeric network, the amount of water absorbed by polymer was dramatically increased. Eventually, the oligomer fragments of polymer were water soluble when the channels were completely degraded (fig 4.2). The mass loss and water uptake measurements were done for 8 weeks. After that the channels were too fragile to be weighed.

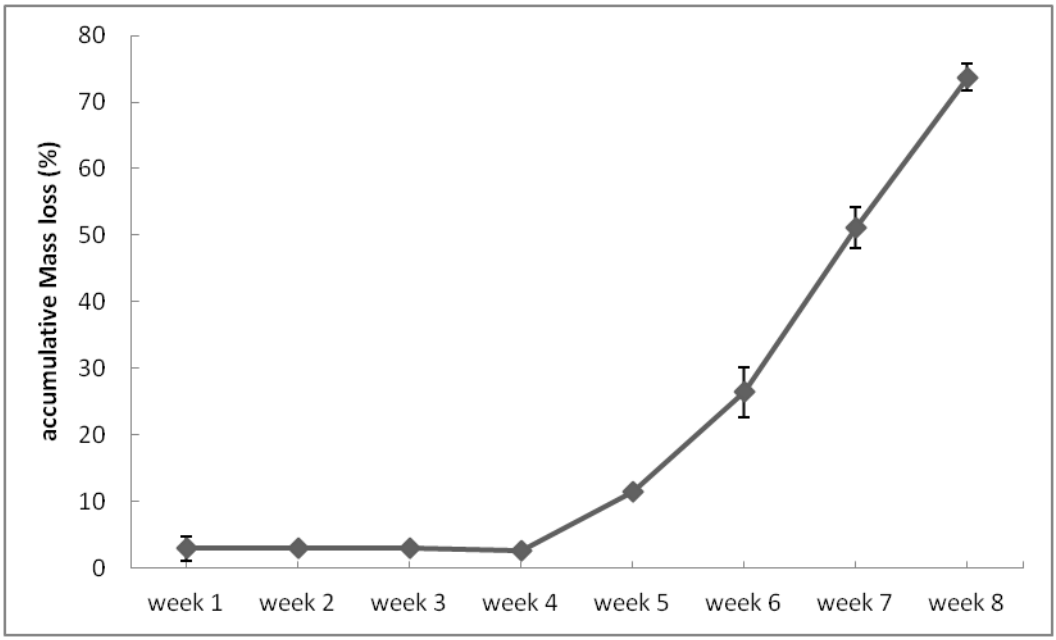

Fig 4. 2 Accumulative mass loss (%) of plain PLGA hollow fiber channel during degradation period. The vertical error bars indicate the standard deviation. Week 2, week3, week 4 and week 5 pose very small standard deviations.

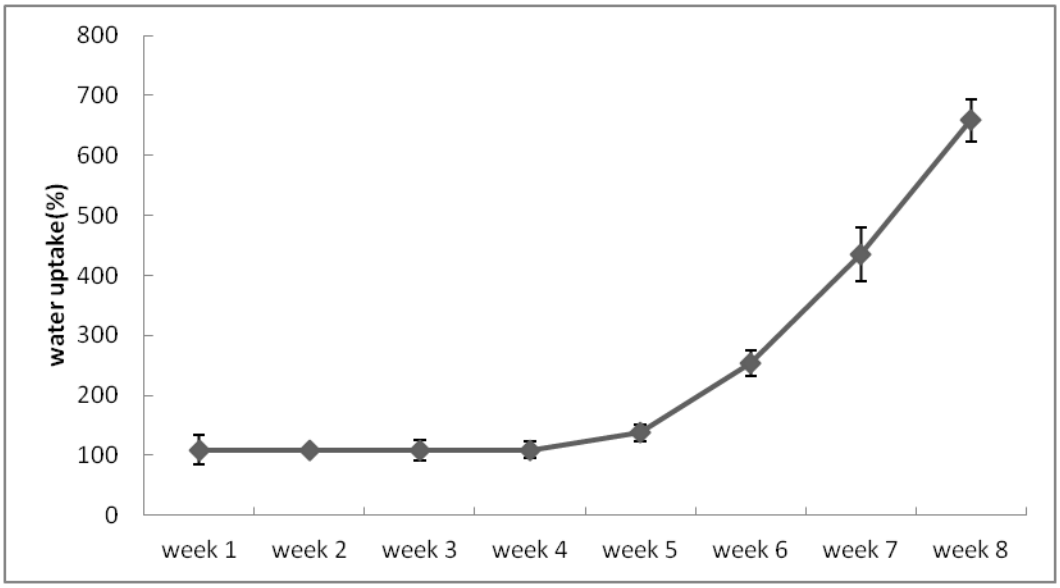

Fig 4. 3 Water uptake of plain PLGA hollow fiber channel during degradation period. The vertical error bars indicate the standard deviation. Week 2 poses very small standard deviation.

4.3 MRI monitoring

PLGA tubes loaded with various concentrations of SPIO were scanned by MRI weekly until the end of degradation period (fig 4.3). As mentioned previously, multiple echo times were applied when acquiring MR images. In addition to T_2 weighted MR images, T_2 mapping was also developed for each tube (fig 4.4). The MRI data showed that higher concentrations of SPIO resulted in a shorter T_2 relaxation time. According to the degradation data, T_2 relaxation time was found to increase along with the degradation of SPIO loaded PLGA. With reference to data obtained from water uptake measurements, we believe that both water penetration and SPIO nanoparticle release from PLGA tubes had effective impacts on the increase of T_2 relaxation time over 12 weeks of degradation. Until Week 4, mild increase in T_2 relaxation time was observed. This behaviour was mostly due to water penetration into polymeric structure rather than SPIO release, since there was no significant mass loss. On the 5^{th} week T_2 relaxation times were increased further due to increase in water absorption and significant mass loss.

However, since the degradation products had not left the polymeric structure of the tube yet, the SPIO nanoparticles were still trapped in the tubes. Therefore the increase in T_2 relaxation times was not dramatic. On Week 6, tubes were even more degraded. The slow release of unbounded SPIO was initiated. The release of SPIO and polymeric degradation combine to give more room for water penetration and caused a cumulative increase in T_2 values.

As a result, increase in T_2 values were noted on Week 7 and T_2 relaxation times increased rapidly until the end of degradation period. As a control group, plain PLGA tubes were also imaged every week over 8 weeks of degradation. We found that the increasing trend of the T_2 relaxation times were related to polymeric degradation, SPIO release and water uptake. All these factors together resulted in a mild increase in T_2 values and an exponential signal recovery pattern of degradation (fig 4.5).

According to our observations, PLGA channels with 0.05%, 0.1% and 0.2% SPIO shown a good contrast in T2 weighted MRI. But with degradation and release of SPIO, they became hyperintnce posing lower contrast. At the end of degradation, PLGA channels loaded with 0.2% SPIO had a better contrast in comparison with other channels (fig 4.8).

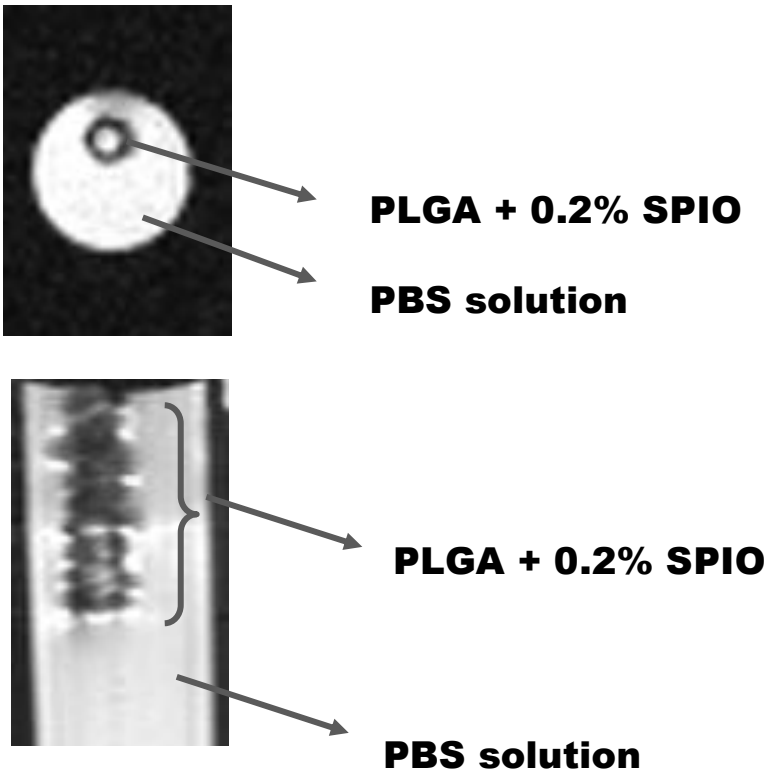

Fig 4. 4 T_2-weighted MR images of PLGA HFC with 0.2 % SPIO (A) Axial and (B) Sagittal view

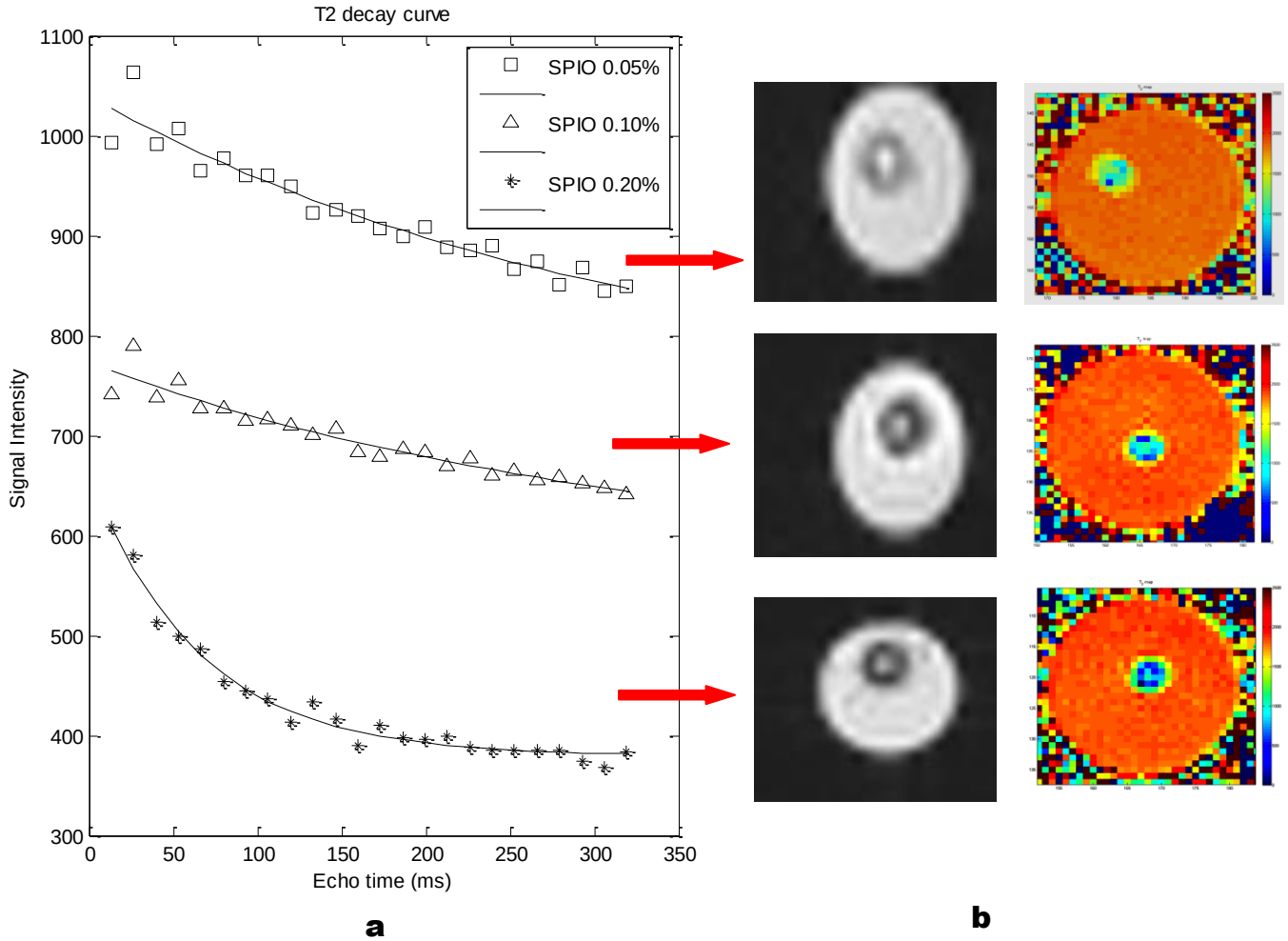

Fig 4. 5 Illustration of T_2 decay curves measured for different concentration of SPIO (0.05%, 0.1% and 0.2%) (a). Axial T_2 weighted MR images (left) and T_2 map (right) for PLGA HFCs with different concentration of SPIO (0%, 0.05%, 0.1% and 0.2%) before degradation process begins(b).

MRI scale (size of the voxel) = 1×1×5 mm

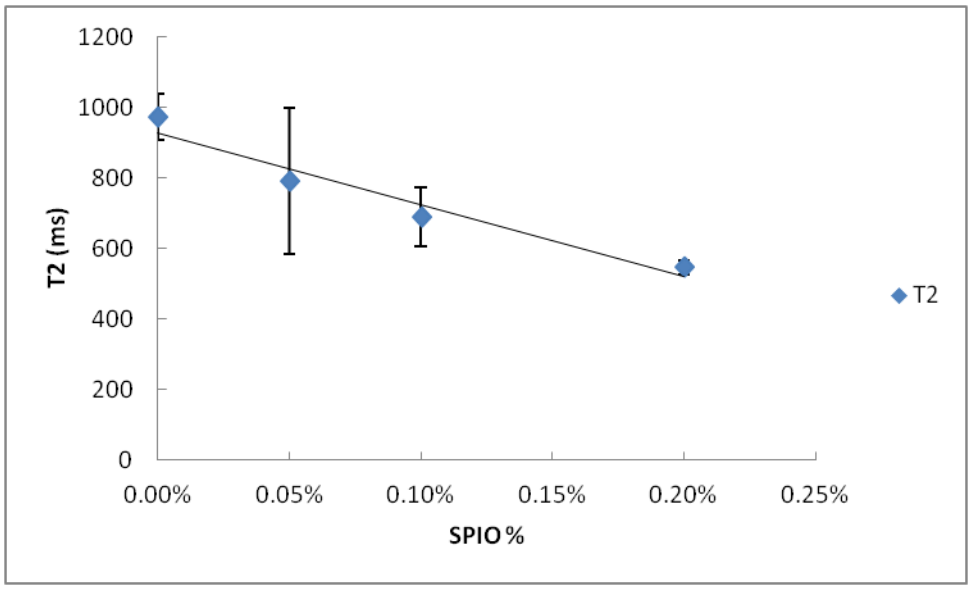

Fig 4. 6 Relaxation time (T_2) versus different concentration of SPIO (0%, 0.05%, 0.1% and 0.2%). Error bars indicate the standard deviation. T2 relaxation value for PLGA loaded with 0.2% SPIO poses very small standard deviation

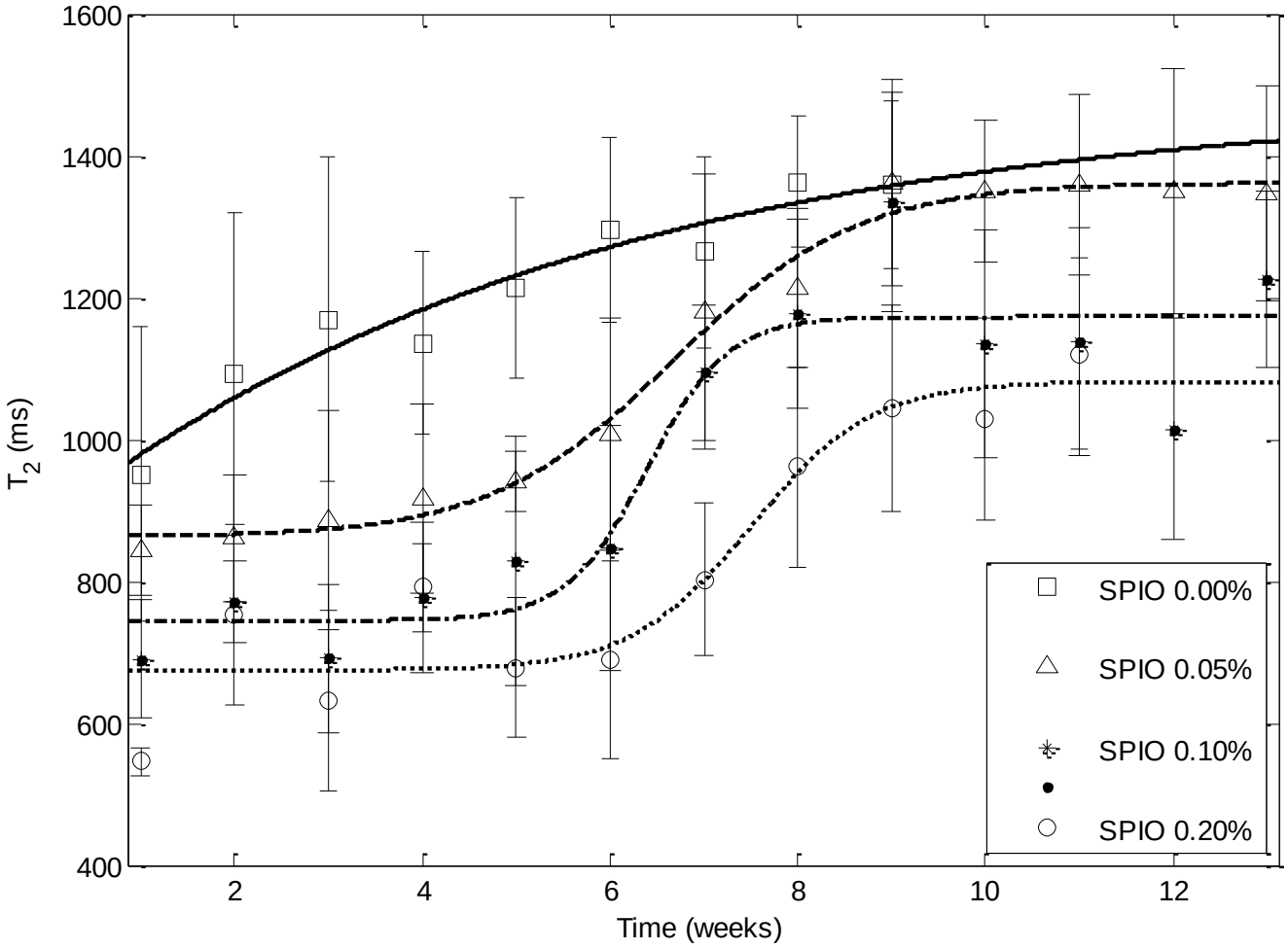

Fig 4. 7 Degradation pattern of PLGA hollow fiber channels; curve fit between T2 relaxation time (ms) and degradation time (ms)

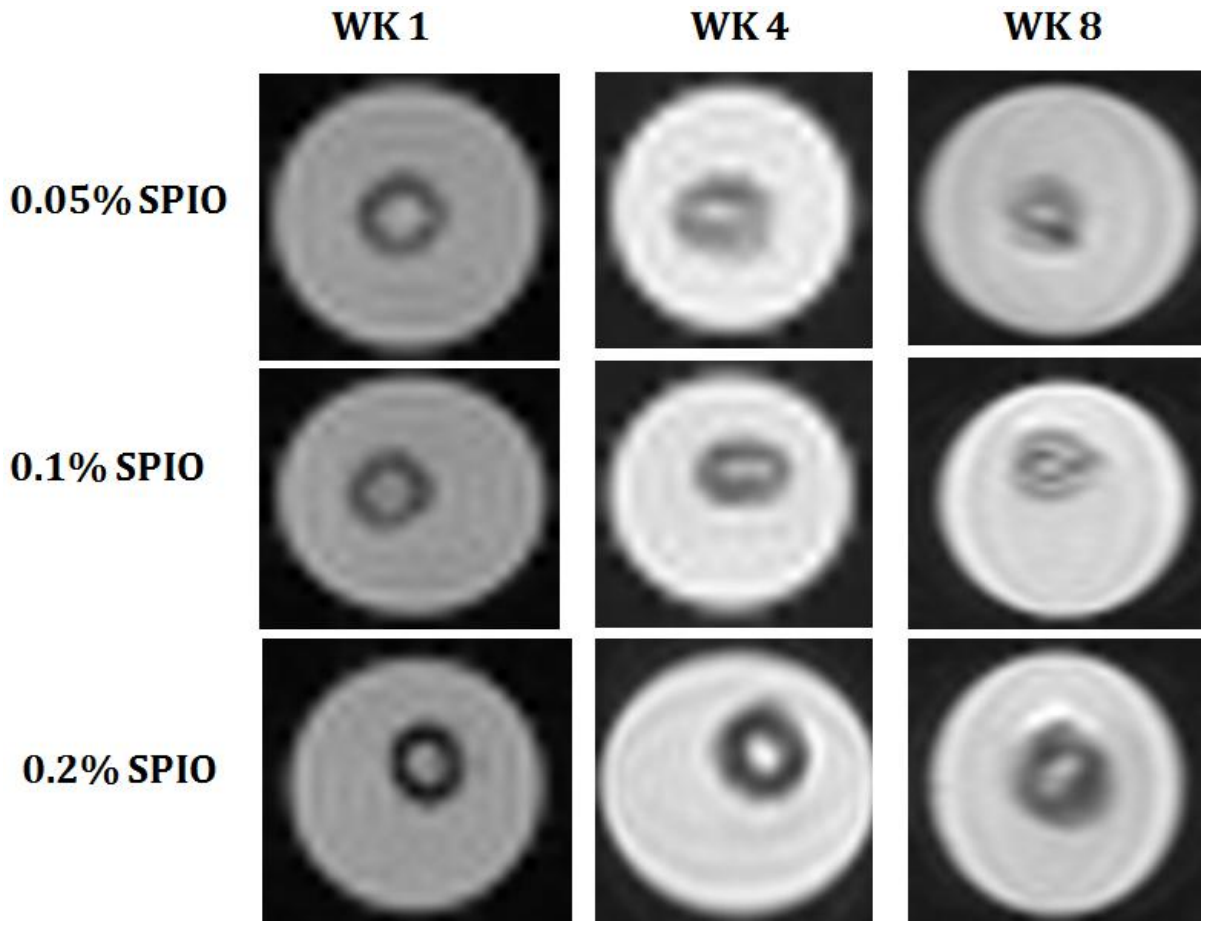

Fig 4. 8 Axial view of T2 weighted MRI for PLGA channels loaded with different concentration of SPIO(0.05%, 0.1%, 0.2%) during 1st, 4th and 8th week of degradation

4.4 Scanning Electron Microscopy (SEM)

The changes in morphology of the polymeric structure, porosity and pore size were assessed using SEM over the degradation period and illustrated versus T_2 weighted MR images for PLGA channels with no SPIO nanoparticles (fig 5.6). At Weeks 1 and Week 2 the tubes were swollen due to water absorption. However, there was no observable change and the original shape was maintained. At Week 3, signs of shrinkage were appeared on the surface of the tubes.

The shrinkage was related to the presence of short polymer chains created as a result of water penetration and cleavage of the bonds. At Week 4, the tubes were even more shrunk and a significant reduction in the pore size was observed. A few numbers of micropores were also appeared on the bulk of the pore walls. At Week 5, an increase in the porosity of the pore walls and bulging of the scaffold was observed. With the progress of degradation, the porosity of the pore walls and the size of the pores were increased. At Week 6 closure of the tube lumen was noticeable. Eventually, the polymer degraded into small fragments.

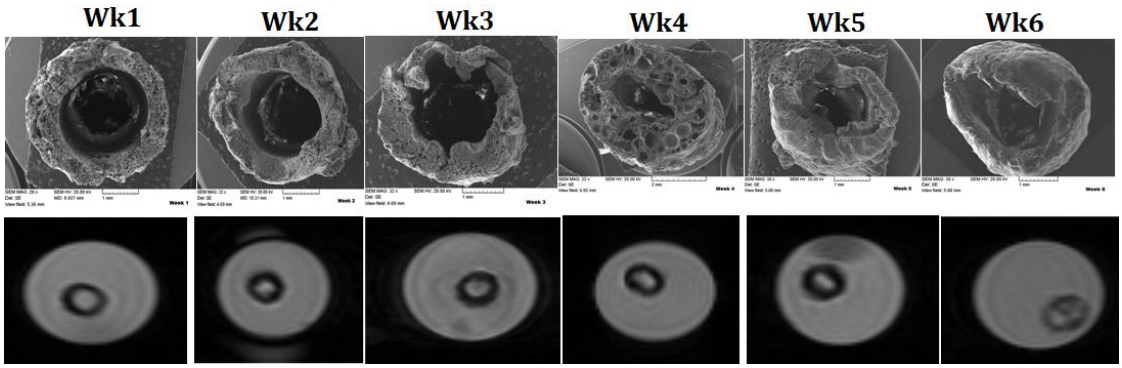

Fig 4.9 SEM visualization for plain PLGA HFCs (left) versus zoomed view of T_2 weighted MR images (right), showing the degradation over 6 weeks. MRI scale = 1×1×5 mm

Chapter 5- DISCUSSION

In this study, we assessed the degradation of PLGA HFCs using MRI which have been never been reported before. PLGA has been successful as a biodegradable polymer because it undergoes hydrolysis in the body to produce the original monomers, lactic acid and glycolic acid. Polymers hydration is the first stage of biodegradation. As the composition of PLGA affects the hydrophobicity of these polymers, the composition influences the hydration of the polymer matrices. This effect will remain during the whole period of biodegradation until the polymers become soluble. There are numerous study reported on the biodegradable mechanism of the polymers [177-180]. We found that nanoparticles could be incorporated directly into foamed PLGA tubes for the recovery of the SCI providing an approach for non-invasive guidance channels monitoring.

5.1 Mass loss and water uptake

As soon as the nerve tube is placed in the aqueous medium, water molecules diffuse into the polymeric structure and degradation starts via polymer chain scission. At the very beginning (first 4 weeks) the outer surface of the tube becomes soft and wrinkly because of the penetration of a large amount of water into the polymer.

Due to the chain scission and ester cleavage, the concentration of the degradation products (lower molecular weight polymer chains with carboxylic end group remaining) increase and remain trapped in the bulk polymer autocatalyzing the hydrolysis of the remaining ester bonds. However, on the surface of the polymer the degradation products easily diffuse into the medium and neutralization of the carboxylic acid end groups caused by the buffer solution reduces the autocatalytic reaction intensively. Therefore, the polymer degradation in the bulk of the tube degrades faster than the polymer composing in surface layer. Due to slow degradation of the surface of the tubes, there is no significant mass loss. At the 5^{th} week of degradation, water uptake increase slightly. At this stage, the oligomers formed in the bulk of the tube become soluble. Thereby, at Week 5 onwards, the mass loss and the release of the acidic products into the medium increased dramatically.

Moreover, small bubbles corresponding to low molecular weight viscous liquid appeared inside the tubes. The bubbles get larger overtime as tubes degrade. This leads to drastic change (shrinkage) in the appearance of the tube. Eventually a highly viscous polymer residue was left that continued to degrade and lose mass until all bonds broke and polymeric fragments dissolved into the aqueous medium.

5.2 MRI monitoring

The intra-cellular SPIO can cause a proton spin and rapid phase loss on MRI, thus decreasing the values of T_2 [181-183]. Due to the existence of free electrons in SPIO nanoparticles, they can produce great magnetism even at a weak external magnetic field. The magnetism will disappear rapidly after removal of the external magnetic field[184]. We obtained similar results showing that with increasing nanoparticle (contrast agent) concentration, the effect of a contrast agent will be magnified such that T_2 relaxation times will decrease [169, 185]. Therefore, PLGA tubes will appear darker in T_2 weighted MR image. Based on MRI data, high concentration of SPIO produced a decrease in T2 relaxation time.

Our findings are in agreement with previous clinical investigations for SPIO quantification in spleen and liver where they showed that the concentration of SPIO and the T_2 relaxation time are highly correlated[186]. Plain PLGA channels and SPIO loaded channels were scanned with MRI on a weekly basis. As the result from the water uptake measurements showed the channels were highly water absorbable. The water molecules penetrate into the channels and when the channels are place in the external magnetic field they started to presses and generate an MR signal from which MR image is constructed. T_2 relaxation time calculations demonstrate an exponential increase in T_2 over degradation time [187]. When approaching the end of the degradation period, T_2 relaxation was very close to the T_2 relaxation of water (2 sec). Despite the degradation and release of SPIO, T_2 relaxation times of the channels are still shorter than T_2 of water.

This phenomena probably is due to the fact that in MRI, a voxel with dimensions 1×1×5 mm is under investigation, some SPIO might still exist in the voxel shortening the T_2 relaxation time (fig 4.7). For SPIO loaded PLGA channels, the presence of nanoparticles leads to the alteration of magnetic susceptibility which contributed to the enhancement of T_2 relaxation time along with water penetration. Although both water absorption and SPIO release are effective factors in the increase of T_2 values but MRI results showed that the influence of the SPIO was predominant. The obtained results showed that T_2 relaxation times demonstrated a degradation behavior profile for PLGA channels during degradation process. At the beginning, when the channels were only hydrated without any significant change in mass, T_2 relaxation times fluctuate around a constant value. This evidence is solely due to water absorption.

During this time, hydroxyl end groups were not able to leave the polymer, thereby trapping the SPIO nanoparticles within the polymer matrix. At the 5^{th} weeks, there was a significant increase in the T_2 relaxation times. This was associated with a sudden increase in mass loss. As discussed previously, when the ester bonds are cleaved and polymeric monomers became water soluble, the channels will begin to lose mass dramatically. Therefore, SPIO nanoparticles that were enclosed within polymeric matrix will have freedom to diffuse out. The release of nanoparticles leads to the enhancement of the MR signal and consequently, T_2 relaxation times. This increasing trend is retained until the 8^{th} week when close to 80% of the polymer mass was lost. Only fragments of the channels were remaining in the last 4 weeks. During this time, the majority of the SPIO nanoparticles were diffused out from the channels.

Large number of void spaces is created within polymeric structure generating large surface area for water absorption. The obtained results from last 4 weeks of degradation study demonstrated large T_2 values close to the T_2 relaxation of water. This is mainly due to huge amount of water penetrating in to the polymer. The increasing trend of T_2 relaxation time for SPIO loaded PLGA channels is a combination of three states. The first state demonstrates the hydration of the channels when the water molecules penetrating into the channels generating MR signal. No degradation occurred and the channels are retaining their integrity prohibiting the SPIO nanoparticles form flowing out of the polymer. In the second stage, due to break out of ester bonds and water solubility of the monomers the mass loss was dramatic. Failure of the polymeric structure makes the magnetic nanoparticles to leave the matrix resulting in a sudden increase of T_2 values. However, at the last stage the channels have almost completely degraded and SPIO nanoparticles have completely diffused out of the polymer. The only parameter inducing the MR signal is the absorbed water molecules. Overall, the results showed that the timeframe when the channels start losing mass results in significant increased of T_2 values. This time period is a transition stage during which the channels move from hydration to degradation state.

5.3 Scanning Electron Microscopy (SEM)

Results showed that when water penetrates into the polymeric structure, the surface layer of the channels start to become soft and wrinkles of the surface were appeared. Penetration of the surface by water initiates hydrolysis reaction and leads to shortening of polymer chain. The mobility of the chains increase and the channels shrink slightly. Shrinkage of the channel is observable on the 4^{th} week of degradation. During this time due to the movement of the chains there is more space for water to get in, accelerating the hydrolysis reaction. Eventually, the hydrolytic products of the PLGA polymer break and leach out from the inside matrix to the surrounding aqueous solution. Therefore, the outer surface morphology becomes more porous and more interconnected channels thought matrix are created. The porous structure provides pathway for SPIO release. Upon this, SPIO is released from polymer matrix and produces even more voids within PLGA channels. Along with polymer degradation, wall cracking creates severe cracks in the wall of the channels. During this time the channel begin to lose mass and the degradation process speeds up until all degradation products are released from the channel and the channels degrades completely.

Chapter 6- CONCLUSIONS

PLGA has been widely used in tissue engineering applications especially for the nerve guidance fabrication. PLGA degrades in water through hydrolysis of its ester linkage. The presence of methyl group in PLA allows this monomer to have hydrophobic property in comparison to PGA. Therefore, PLGA with higher PLA content has a lower degradation speed. In order to develop biodegradable guidance channels with optimal characteristic, it is of great importance to investigate and understand its degradation behavior. Up to date, many studies have been done assessing the degradation of PLGA and the factors influencing this reaction [188-190].

Despite these studies, no report was found on non-invasive monitoring of the PLGA throughout its degradation. Here, we described a new method to monitor the degradation of the PLGA guidance channels non-invasively using MRI. This technique includes loading PLGA hollow fiber channels with SPIO nanopartilces. SPIO nanoparticles are able to magnetize when introduced to static field. Hence, a local magnetic field will be generated surrounding SPIO nanoparticles which result in an interaction between the electronic dipoles of SPIO and water protons. This will lead to a linear association between SPIO concentration and T_2 relaxation times [191-193]. There are two important phenomena occur during degradation of the PLGA. First, degradation increases the number of acid chain ends which autocatalyse the ester bond hydrolysis. Second, the oligomers that are water soluble can escape form polymeric matrix[58].

Therefore, the soluble oligomers which are close to the surface leach out while those inside the matrix remain trapped. As a result, at the beginning of degradation when there is no remarkable mass loss, the SPIO are not able to release out of the matrix. Thus no significant T_2 relaxation was notable. However, as degradation proceeds more carboxylic acid group produce resulting in burst of PLGA channel. Upon burst of the PLGA nerve guide channel, the SPIO nanoparticle flow out of the polymeric network. This evidence increases the T_2 relaxation time and induces a lower MR signal. The slight fluctuation of the T_2 relaxation time was mostly due to water penetration rather than SPIO release. However, with respect to our observations the alteration of the T_2 relaxation time for the PLGA channel with 0% SPIO was solely due to water penetration in to the polymer structure. The presented approach provided a great advantage of non-invasive monitoring a PLGA guidance channel and will facilitate the investigation of the biodegradation of polymeric implants non-invasively.

Chapter 7- FUTURE WORKS

In the presented work, a novel non- destructive monitoring technique was presented to assess the *in vitro* degradation of the nerve guide tubes. With respect to the obtained experimental results, it would be interesting to conduct the following experiments:

I. Extending this monitoring technique to assess the degradation of nerve guide tubes after *in vivo* implantation. Further optimization of this technique may help determining an ideal protocol for *in vivo* monitoring of different tissue scaffolds.

II. Quantification of SPIO release form guidance channels and incorporation of release rate with the polymeric mass loss of the channels.

III. Fabrication of multi-layer drug delivery system incorporated with MR contrast agent in order to track the drug release. The layers of the channel can be composed of different polymer with different degradation rate to tune the drug release according to the desired application.

References

1. McKay, W.B., *Neurophysiological characterization of the New Anatomy and motor control that results from neurological injury or disease.* Clinical Neurology and Neurosurgery. **114**(5): p. 447-454.
2. Schmidt, C.E. and J.B. Leach, *Neural tissue engineering: Strategies for repair and regeneration.* Annual Review of Biomedical Engineering, 2003. **5**: p. 293-347.
3. Huang, Y.C. and Y.Y. Huang, *Biomaterials and strategies for nerve regeneration.* Artificial Organs, 2006. **30**(7): p. 514-522.
4. Kalantarian, B., et al., *Gains and losses of the XII-VII component of the "baby-sitter" procedure: A morphometric analysis.* Journal of Reconstructive Microsurgery, 1998. **14**(7): p. 459-471.
5. Weber, R.V. and S.E. Mackinnon, *Bridging the Neural Gap.* Clinics in Plastic Surgery, 2005. **32**(4): p. 605-616.
6. Kehoe, S., X.F. Zhang, and D. Boyd, *FDA approved guidance conduits and wraps for peripheral nerve injury: A review of materials and efficacy.* Injury-International Journal of the Care of the Injured. **43**(5): p. 553-572.
7. Schlosshauer, B., et al., *Rat Schwann cells in bioresorbable nerve guides to promote and accelerate axonal regeneration.* Brain Research, 2003. **963**(1-2): p. 321-326.
8. Keilhoff, G., et al., *Peripheral nerve tissue engineering: Autologous Schwann cells vs. transdifferentiated mesenchymal stem cells.* Tissue Engineering, 2006. **12**(6): p. 1451-1465.
9. Cai, J., et al., *Permeable guidance channels containing microfilament scaffolds enhance axon growth and maturation.* Journal of Biomedical Materials Research Part A, 2005. **75A**(2): p. 374-386.
10. Chew, S.Y., et al., *The effect of the alignment of electrospun fibrous scaffolds on Schwann cell maturation.* Biomaterials, 2008. **29**(6): p. 653-661.
11. Kim, Y.-t., et al., *The role of aligned polymer fiber-based constructs in the bridging of long peripheral nerve gaps.* Biomaterials, 2008. **29**(21): p. 3117-3127.
12. Dodla, M.C. and R.V. Bellamkonda, *Differences between the effect of anisotropic and isotropic laminin and nerve growth factor presenting scaffolds on nerve regeneration across long peripheral nerve gaps.* Biomaterials, 2008. **29**(1): p. 33-46.
13. Buttiglione, M., et al., *Behaviour of SH-SY5Y neuroblastoma cell line grown in different media and on different chemically modified substrates.* Biomaterials, 2007. **28**(19): p. 2932-2945.
14. Chiu, D.T.W. and B. Strauch, *A Prospective Clinical Evaluation of Autogenous Vein Grafts Used as a Nerve Conduit for Distal Sensory Nerve Defects of 3 cm or Less.* Plastic and Reconstructive Surgery, 1990. **86**(5): p. 928-934.
15. Purves D, A.G., Fitzpatrick ed. *Neuroscience.* 2001.
16. Oudega, M., L.D.F. Moon, and R.J.D. Leme, *Schwann cells for spinal cord repair.* Brazilian Journal of Medical and Biological Research, 2005. **38**(6): p. 825-835.
17. Choo, A.M., et al., *Secondary pathology following contusion, dislocation, and distraction spinal cord injuries.* Experimental Neurology, 2008. **212**(2): p. 490-506.

18. McKeon, R.J., et al., *Reduction of neurite outgrowth in a model of glial scarring following cns injury is correlated with the expression of inhibitory molecules on reactive astrocytes.* Journal of Neuroscience, 1991. **11**(11): p. 3398-3411.
19. Shechter, R., et al., *Infiltrating Blood-Derived Macrophages Are Vital Cells Playing an Anti-inflammatory Role in Recovery from Spinal Cord Injury in Mice.* Plos Medicine, 2009. **6**(7).
20. Thuret, S., L.D.F. Moon, and F.H. Gage, *Therapeutic interventions after spinal cord injury.* Nat Rev Neurosci, 2006. **7**(8): p. 628-643.
21. Carlstedt, T., *Nerve fibre regeneration across the peripheral-central transitional zone.* Journal of Anatomy, 1997. **190**: p. 51-56.
22. Fraher, J.P., *The transitional zone and CNS regeneration (vol 194, pg 161, 1999).* Journal of Anatomy, 2000. **196**: p. 137-158.
23. Tabesh, H., et al., *The role of biodegradable engineered scaffolds seeded with Schwann cells for spinal cord regeneration.* Neurochemistry International, 2009. **54**(2): p. 73-83.
24. Oudega, M. and T. Hagg, *Nerve growth factor promotes regeneration of sensory axons into adult rat spinal cord.* Experimental Neurology, 1996. **140**(2): p. 218-229.
25. Bradbury, E.J., et al., *NT-3 promotes growth of lesioned adult rat sensory axons ascending in the dorsal columns of the spinal cord.* European Journal of Neuroscience, 1999. **11**(11): p. 3873-3883.
26. Romero, M.I., et al., *Functional regeneration of chronically injured sensory afferents into adult spinal cord after neurotrophin gene therapy.* Journal of Neuroscience, 2001. **21**(21): p. 8408-8416.
27. Levison, S.W., et al., *Acute exposure to CNTF in vivo induces multiple components of reactive gliosis.* Experimental Neurology, 1996. **141**(2): p. 256-268.
28. Rabchevsky, A.G., et al., *Basic Fibroblast Growth Factor (bFGF) Enhances Functional Recovery Following Severe Spinal Cord Injury to the Rat.* Experimental Neurology, 2000. **164**(2): p. 280-291.
29. Garbossa, D., et al., *Recent therapeutic strategies for spinal cord injury treatment: possible role of stem cells.* Neurosurgical Review. **35**(3): p. 293-311.
30. Cao, Q.-l., et al., *Pluripotent Stem Cells Engrafted into the Normal or Lesioned Adult Rat Spinal Cord Are Restricted to a Glial Lineage.* Experimental Neurology, 2001. **167**(1): p. 48-58.
31. Wang, H.B., C.B. Liu, and X.Q. Ma, *Alginic acid sodium hydrogel co-transplantation with Schwann cells for rat spinal cord repair.* Archives of Medical Science. **8**(3): p. 563-568.
32. Dasari, V.R., et al., *Axonal remyelination by cord blood stem cells after spinal cord injury.* Journal of Neurotrauma, 2007. **24**(2): p. 391-410.
33. Straley, K.S., C.W.P. Foo, and S.C. Heilshorn, *Biomaterial Design Strategies for the Treatment of Spinal Cord Injuries.* Journal of Neurotrauma. **27**(1): p. 1-19.
34. Liu, C., Z. Xia, and J.T. Czernuszka, *Design and development of three-dimensional scaffolds for tissue engineering.* Chemical Engineering Research & Design, 2007. **85**(A7): p. 1051-1064.
35. Katayama, Y., et al., *Coil-reinforced hydrogel tubes promote nerve regeneration equivalent to that of nerve autografts.* Biomaterials, 2006. **27**(3): p. 505-518.

36. Dalton, P.D., L. Flynn, and M.S. Shoichet, *Manufacture of poly(2-hydroxyethyl methacrylate-co-methyl methacrylate) hydrogel tubes for use as nerve guidance channels.* Biomaterials, 2002. **23**(18): p. 3843-3851.
37. Itoh, S., et al., *Evaluation of cross-linking procedures of collagen tubes used in peripheral nerve repair.* Biomaterials, 2002. **23**(23): p. 4475-4481.
38. Freier, T., et al., *Controlling cell adhesion and degradation of chitosan films by N-acetylation.* Biomaterials, 2005. **26**(29): p. 5872-5878.
39. Curtis, A. and C. Wilkinson, *Topographical control of cells.* Biomaterials, 1997. **18**(24): p. 1573-1583.
40. Gong, H.P., et al., *Studies on nerve cell affinity of chitosan-derived materials.* Journal of Biomedical Materials Research, 2000. **52**(2): p. 285-295.
41. Suzuki, M., et al., *Tendon chitosan tubes covalently coupled with synthesized laminin peptides facilitate nerve regeneration in vivo.* Journal of Neuroscience Research, 2003. **72**(5): p. 646-659.
42. Meiners, S. and M.L.T. Mercado, *Functional peptide sequences derived from extracellular matrix glycoproteins and their receptors - Strategies to improve neuronal regeneration.* Molecular Neurobiology, 2003. **27**(2): p. 177-195.
43. Cui, F.Z., et al., *Hyaluronic acid hydrogel immobilized with RGD peptides for brain tissue engineering.* Journal of Materials Science-Materials in Medicine, 2006. **17**(12): p. 1393-1401.
44. Xu, G., et al., *Optic nerve regeneration in polyglycolic acid-chitosan conduits coated with recombinant L1-Fc.* Neuroreport, 2004. **15**(14): p. 2167-2172.
45. Johnson, E.O. and P.N. Soucacos, *Nerve repair: Experimental and clinical evaluation of biodegradable artificial nerve guides.* Injury-International Journal of the Care of the Injured, 2008. **39**: p. S30-S36.
46. Weber, R.V. and S.E. Mackinnon, *Bridging the neural gap.* Clinics in Plastic Surgery, 2005. **32**(4): p. 605-+.
47. Xu, X.Y., et al., *Peripheral nerve regeneration with sustained release of poly(phosphoester) microencapsulated nerve growth factor within nerve guide conduits.* Biomaterials, 2003. **24**(13): p. 2405-2412.
48. Cheng, H., et al., *Laminin-incorporated nerve conduits made by plasma treatment for repairing spinal cord injury.* Biochemical and Biophysical Research Communications, 2007. **357**(4): p. 938-944.
49. Hofmann, D., et al., *Knowledge-Based Approach towards Hydrolytic Degradation of Polymer-Based Biomaterials.* Advanced Materials, 2009. **21**(32-33): p. 3237-3245.
50. Gopferich, A., *Mechanisms of polymer degradation and erosion.* Biomaterials, 1996. **17**(2): p. 103-114.
51. Ammala, A., et al., *An overview of degradable and biodegradable polyolefins.* Progress in Polymer Science. **36**(8): p. 1015-1049.
52. Tamada, J.A. and R. Langer, *Erosion kinetics of hydrolytically degradable polymers.* Proceedings of the National Academy of Sciences of the United States of America, 1993. **90**(2): p. 552-556.
53. Lee, W.C. and I.M. Chu, *Preparation and degradation behavior of polyanhydrides nanoparticles.* Journal of Biomedical Materials Research Part B-Applied Biomaterials, 2008. **84B**(1): p. 138-146.
54. Kipper, M.J., et al., *Nanoscale morphology of polyanhydride copolymers.* Macromolecules, 2005. **38**(20): p. 8468-8472.

55. Perron, J.K., et al., *A Study on the Effect of Degradation Media on the Physical and Mechanical Properties of Porous PLGA 85/15 Scaffolds.* Journal of Biomedical Materials Research Part B-Applied Biomaterials, 2009. **91B**(2): p. 876-886.
56. Zolnik, B.S. and D.J. Burgess, *Effect of acidic pH on PLGA microsphere degradation and release.* Journal of Controlled Release, 2007. **122**(3): p. 338-344.
57. Holy, C.E., et al., *In vitro degradation of a novel poly(lactide-co-glycolide) 75/25 foam.* Biomaterials, 1999. **20**(13): p. 1177-1185.
58. Lyu, S.P. and D. Untereker, *Degradability of Polymers for Implantable Biomedical Devices.* International Journal of Molecular Sciences, 2009. **10**(9): p. 4033-4065.
59. Gualandi, C., et al., *Poly(butylene/diethylene glycol succinate) multiblock copolyester as a candidate biomaterial for soft tissue engineering: Solid-state properties, degradability, and biocompatibility.* Journal of Bioactive and Compatible Polymers. **27**(3): p. 244-264.
60. Rothstein, S.N., W.J. Federspiel, and S.R. Little, *A unified mathematical model for the prediction of controlled release from surface and bulk eroding polymer matrices.* Biomaterials, 2009. **30**(8): p. 1657-1664.
61. Wang, N., et al., *Synthesis, characterization, biodegradation, and drug delivery application of biodegradable lactic/glycolic acid polymers I. Synthesis and characterization.* Journal of Biomaterials Science-Polymer Edition, 2000. **11**(3): p. 301-318.
62. Belkas, J.S., et al., *Long-term in vivo biomechanical properties and biocompatibility of poly(2-hydroxyethyl methacrylate-co-methyl methacrylate) nerve conduits.* Biomaterials, 2005. **26**(14): p. 1741-1749.
63. Moon, L.D.F., et al., *Motor enrichment sustains hindlimb movement recovered after spinal cord injury and glial transplantation.* Restorative Neurology and Neuroscience, 2006. **24**(3): p. 147-161.
64. Friedman, J.A., et al., *Biodegradable polymer grafts for surgical repair of the injured spinal cord.* Neurosurgery, 2002. **51**(3): p. 742-751.
65. Madigan, N.N., et al., *Current tissue engineering and novel therapeutic approaches to axonal regeneration following spinal cord injury using polymer scaffolds.* Respiratory Physiology & Neurobiology, 2009. **169**(2): p. 183-199.
66. Nisbet, D.R., et al., *Neural Tissue Engineering of the CNS Using Hydrogels - A review (vol 5, pg 293, 2003).* Journal of Biomedical Materials Research Part B-Applied Biomaterials, 2009. **88B**(1): p. 304-304.
67. Newman, K.D., et al., *Bioactive hydrogel-filament scaffolds for nerve repair and regeneration.* International Journal of Artificial Organs, 2006. **29**(11): p. 1082-1091.
68. Traore, A.S., et al., *In vivo magnetic resonance imaging and relaxometry study of a porous hydrogel implanted in the trapezius muscle of rabbits.* Tissue Engineering, 2000. **6**(3): p. 265-278.
69. Ramaswamy, S., et al., *An analysis of the integration between articular cartilage and nondegradable hydrogel using magnetic resonance imaging.* Journal of Biomedical Materials Research Part B: Applied Biomaterials, 2006. **77B**(1): p. 144-148.
70. Kim, J., et al., *Bone regeneration using hyaluronic acid-based hydrogel with bone morphogenic protein-2 and human mesenchymal stem cells.* Biomaterials, 2007. **28**(10): p. 1830-1837.
71. Perale, G., et al., *Hydrogels in Spinal Cord Injury Repair Strategies.* ACS Chemical Neuroscience. **2**(7): p. 336-345.

72. Sell, S.A., et al., *The Use of Natural Polymers in Tissue Engineering: A Focus on Electrospun Extracellular Matrix Analogues.* Polymers. **2**(4): p. 522-553.
73. Chiono, V., C. Tonda-Turo, and G. Ciardelli, *Artificial scaffolds for peripheral nerve reconstruction,* in *Essays on Peripheral Nerve Repair and Regeneration*. 2009. p. 173-198.
74. Ciardelli, G. and V. Chiono, *Materials for peripheral nerve regeneration.* Macromolecular Bioscience, 2006. **6**(1): p. 13-26.
75. Nisbet, D.R., et al., *Neural tissue engineering of the CNS using hydrogels.* Journal of Biomedical Materials Research Part B-Applied Biomaterials, 2008. **87B**(1): p. 251-263.
76. Kadler, K.E., et al., *Collagens at a glance.* Journal of Cell Science, 2007. **120**(12): p. 1955-1958.
77. Schnell, E., et al., *Guidance of glial cell. migration and axonal growth on electrospun nanofibers of poly-epsilon-caprolactone and a collagen/poly-epsilon-caprolactone blend.* Biomaterials, 2007. **28**(19): p. 3012-3025.
78. Phillips, J.B., et al., *Neural tissue engineering: A self-organizing collagen guidance conduit.* Tissue Engineering, 2005. **11**(9-10): p. 1611-1617.
79. Zeugolis, D.I., R.G. Paul, and G. Attenburrow, *Engineering extruded collagen fibers for biomedical applications.* Journal of Applied Polymer Science, 2008. **108**(5): p. 2886-2894.
80. Liu, T., et al., *Nanofibrous Collagen Nerve Conduits for Spinal Cord Repair.* Tissue Engineering Part A. **18**(9-10): p. 1057-1066.
81. Parenteau-Bareil, R.m., R. Gauvin, and F.o. Berthod, *Collagen-Based Biomaterials for Tissue Engineering Applications.* Materials. **3**(3): p. 1863-1887.
82. Hiraoka, Y., et al., *Fabrication and characterization of mechanically reinforced collagen sponge,* in *Asbm6: Advanced Biomaterials Vi*. 2005. p. 385-388.
83. Freier, T., et al., *Chitin-based tubes for tissue engineering in the nervous system.* Biomaterials, 2005. **26**(22): p. 4624-4632.
84. Wang, D.-Y. and Y.-Y. Huang, *Fabricate coaxial stacked nerve conduits through soft lithography and molding processes.* Journal of Biomedical Materials Research Part A, 2008. **85A**(2): p. 434-438.
85. Bozkurt, G., et al., *Chitosan Channels Containing Spinal Cord-Derived Stem/Progenitor Cells for Repair of Subacute Spinal Cord Injury in the Rat.* Neurosurgery. **67**(6): p. 1733-1744.
86. Alves, N.M. and J.F. Mano, *Chitosan derivatives obtained by chemical modifications for biomedical and environmental applications.* International Journal of Biological Macromolecules, 2008. **43**(5): p. 401-414.
87. Xie, F., et al., *In vitro and in vivo evaluation of a biodegradable chitosan–PLA composite peripheral nerve guide conduit material.* Microsurgery, 2008. **28**(6): p. 471-479.
88. Zahir, T., et al., *Bioengineering neural stem/progenitor cell-coated tubes for spinal cord injury repair.* Cell Transplantation, 2008. **17**(3): p. 245-254.
89. Gamez, E., et al., *Photofabricated gelatin-based nerve conduits: Nerve tissue regeneration potentials.* Cell Transplantation, 2004. **13**(5): p. 549-564.
90. Liu, B.-S., *Fabrication and evaluation of a biodegradable proanthocyanidin-crosslinked gelatin conduit in peripheral nerve repair.* Journal of Biomedical Materials Research Part A, 2008. **87A**(4): p. 1092-1102.

91. Chang, J.-Y., et al., *In Vivo Evaluation of a Biodegradable EDC/NHS-Cross-Linked Gelatin Peripheral Nerve Guide Conduit Material.* Macromolecular Bioscience, 2007. **7**(4): p. 500-507.
92. Lu, M.C., et al., *Influence of cross-linking degree of a biodegradable genipin-cross-linked gelatin guide on peripheral nerve regeneration.* Journal of Biomaterials Science-Polymer Edition, 2007. **18**(7): p. 843-863.
93. Khataokar, A., et al., *Development of Schwann Cell-Seeded Conduit Using Chitosan-Based Biopolymers for Nerve Repair*, in *2010 Ieee 36th Annual Northeast Bioengineering Conference*.
94. Novikova, L.N., L.N. Novikov, and J.O. Kellerth, *Biopolymers and biodegradable smart implants for tissue regeneration after spinal cord injury.* Current Opinion in Neurology, 2003. **16**(6): p. 711-715.
95. Suzuki, K., et al., *Regeneration of transected spinal cord in young adult rats using freeze-dried alginate gel.* Neuroreport, 1999. **10**(14): p. 2891-2894.
96. Mukhatyar, V.J., et al., *Role of fibronectin in topographical guidance of neurite extension on electrospun fibers.* Biomaterials. **32**(16): p. 3958-3968.
97. King, V.R., et al., *The use of injectable forms of fibrin and fibronectin to support axonal ingrowth after spinal cord injury.* Biomaterials. **31**(15): p. 4447-4456.
98. Priestley, J.V., et al., *Stimulating regeneration in the damaged spinal cord.* Journal of Physiology-Paris, 2002. **96**(1-2): p. 123-133.
99. King, V.R., et al., *Characterization of non-neuronal elements within fibronectin mats implanted into the damaged adult rat spinal cord.* Biomaterials, 2006. **27**(3): p. 485-496.
100. Ichihara, S., Y. Inada, and T. Nakamura, *Artificial nerve tubes and their application for repair of peripheral nerve injury: an update of current concepts.* Injury, 2008. **39,** Supplement 4(0): p. 29-39.
101. Kannan, R.Y., et al., *Artificial nerve conduits in peripheral-nerve repair.* Biotechnology and Applied Biochemistry, 2005. **41**(3): p. 193-200.
102. Gautier, S.E., et al., *Poly(alpha-hydroxyacids) for application in the spinal cord: Resorbability and biocompatibility with adult rat Schwann cells and spinal cord.* Journal of Biomedical Materials Research, 1998. **42**(4): p. 642-654.
103. Cai, J., et al., *Evaluation of cellular organization and axonal regeneration through linear PLA foam implants in acute and chronic spinal cord injury.* Journal of Biomedical Materials Research Part A, 2007. **83A**(2): p. 512-520.
104. Novikov, L.N., et al., *A novel biodegradable implant for neuronal rescue and regeneration after spinal cord injury.* Biomaterials, 2002. **23**(16): p. 3369-3376.
105. Xu, X.Y., et al., *The behaviour of neural stem cells on polyhydroxyalkanoate nanofiber scaffolds.* Biomaterials. **31**(14): p. 3967-3975.
106. Hwang, D.H., et al., *Combination of Multifaceted Strategies to Maximize the Therapeutic Benefits of Neural Stem Cell Transplantation for Spinal Cord Repair.* Cell Transplantation. **20**(9): p. 1361-1379.
107. Flynn, L., P.D. Dalton, and M.S. Shoichet, *Fiber ternplating of poly(2-hydroxyethyl methacrylate) for neural tissue engineering.* Biomaterials, 2003. **24**(23): p. 4265-4272.
108. Chen, B.K.K., et al., *Comparison of polymer scaffolds in rat spinal cord: A step toward quantitative assessment of combinatorial approaches to spinal cord repair.* Biomaterials. **32**(32): p. 8077-8086.

109. Kang, K.N., et al., *Tissue engineered regeneration of completely transected spinal cord using human mesenchymal stem cells.* Biomaterials. **33**(19): p. 4828-4835.
110. Zhu, Y.Q., et al., *Nanofibrous Patches for Spinal Cord Regeneration.* Advanced Functional Materials. **20**(9): p. 1433-1440.
111. Kim, K., et al., *Control of degradation rate and hydrophilicity in electrospun non-woven poly(D,L-lactide) nanofiber scaffolds for biomedical applications.* Biomaterials, 2003. **24**(27): p. 4977-4985.
112. Kricheldorf, H.R., *Syntheses and application of polylactides.* Chemosphere, 2001. **43**(1): p. 49-54.
113. Patist, C.M., et al., *Freeze-dried poly(d,l-lactic acid) macroporous guidance scaffolds impregnated with brain-derived neurotrophic factor in the transected adult rat thoracic spinal cord.* Biomaterials, 2004. **25**(9): p. 1569-1582.
114. Ljungberg, C., et al., *Neuronal survival using a resorbable synthetic conduit as an alternative to primary nerve repair.* Microsurgery, 1999. **19**(6): p. 259-264.
115. Novikov, L.N., et al., *A novel biodegradable implant for neuronal rescue and regeneration after spinal cord injury.* Biomaterials, 2002. **23**(16): p. 3369-3376.
116. Venugopal, J., Y.Z. Zhang, and S. Ramakrishna, *Electrospun nanofibres: Biomedical applications.* Proceedings of the Institution of Mechanical Engineers, Part N: Journal of Nanoengineering and Nanosystems, 2004. **218**(1): p. 35-45.
117. Bender, M.D., et al., *Multi-channeled biodegradable polymer/CultiSpher composite nerve guides.* Biomaterials, 2004. **25**(7-8): p. 1269-1278.
118. Astete, C.E. and C.M. Sabliov, *Synthesis and characterization of PLGA nanoparticles.* Journal of Biomaterials Science-Polymer Edition, 2006. **17**(3): p. 247-289.
119. Prabhakaran, M.P., J. Venugopal, and S. Ramakrishna, *Electrospun nanostructured scaffolds for bone tissue engineering.* Acta Biomaterialia, 2009. **5**(8): p. 2884-2893.
120. Cai, L., et al., *Photo-cured Biodegradable Polymer Substrates of Varying Stiffness and Microgroove Dimensions for Promoting Nerve Cell Guidance and Differentiation.* Langmuir.
121. Wang, S., et al., *A new nerve guide conduit material composed of a biodegradable poly(phosphoester).* Biomaterials, 2001. **22**(10): p. 1157-1169.
122. Yucel, D., G.T. Kose, and V. Hasirci, *Polyester based nerve guidance conduit design.* Biomaterials. **31**(7): p. 1596-1603.
123. Kalbermatten, D.F., et al., *Fibrin matrix for suspension of regenerative cells in an artificial nerve conduit.* Journal of Plastic Reconstructive and Aesthetic Surgery, 2008. **61**(6): p. 669-675.
124. Madduri, S., M. Papaloizos, and B. Gander, *Trophically and topographically functionalized silk fibroin nerve conduits for guided peripheral nerve regeneration.* Biomaterials. **31**(8): p. 2323-2334.
125. Nakayama, K., et al., *Enhancement of peripheral nerve regeneration using bioabsorbable polymer tubes packed with fibrin gel.* Artificial Organs, 2007. **31**(7): p. 500-508.
126. Ahmed, M.R., et al., *Microwave irradiated collagen tubes as a better matrix for peripheral nerve regeneration.* Brain Research, 2005. **1046**(1â€“2): p. 55-67.
127. Widmer, M.S., et al., *Manufacture of porous biodegradable polymer conduits by an extrusion process for guided tissue regeneration.* Biomaterials, 1998. **19**(21): p. 1945-1955.

128. Wang, S. and L. Cai, *Polymers for Fabricating Nerve Conduits.* International Journal of Polymer Science. **2010**.
129. Purcell, E.M., H.C. Torrey, and R.V. Pound, *Resonance absorption by nuclear magnetic moments in a solid.* Physical Review, 1946. **69**(1-2): p. 37-38.
130. Bloch, F., *Nuclear induction.* Physical Review, 1946. **70**(7-8): p. 460-474.
131. Lauterbur, P.C., *Image formation by induced local interactions - examples employing nuclear magnetic-resonance.* Nature, 1973. **242**(5394): p. 190-191.
132. Mansfield, P. and P.K. Grannell, *NMR DIFFRACTION IN SOLIDS.* Journal of Physics C-Solid State Physics, 1973. **6**(22): p. L422-L426.
133. Plewes, D.B. and W. Kucharczyk, *Physics of MRI: A primer.* Journal of Magnetic Resonance Imaging. **35**(5): p. 1038-1054.
134. Chavhan, G.B., et al., *Principles, Techniques, and Applications of T2*-based MR Imaging and Its Special Applications.* Radiographics, 2009. **29**(5): p. 1433-U272.
135. Lee, G.H., Y. Chang, and T.J. Kim, *Blood-Pool and Targeting MRI Contrast Agents: From Gd-Chelates to Gd-Nanoparticles.* European Journal of Inorganic Chemistry, (12): p. 1924-1933.
136. Dorazio, S.J. and J.R. Morrow, *The Development of Iron(II) Complexes as ParaCEST MRI Contrast Agents.* European Journal of Inorganic Chemistry, (12): p. 2006-2014.
137. Botta, M. and L. Tei, *Relaxivity Enhancement in Macromolecular and Nanosized GdIII-Based MRI Contrast Agents.* European Journal of Inorganic Chemistry, (12): p. 1945-1960.
138. Murph, S.E.H., et al., *Manganese-gold nanoparticles as an MRI positive contrast agent in mesenchymal stem cell labeling.* Journal of Nanoparticle Research. **14**(4).
139. Sommer, W.H., et al., *Contrast agents as a biological marker in magnetic resonance imaging of the liver: conventional and new approaches.* Abdominal Imaging. **37**(2): p. 164-179.
140. Iwaki, S., et al., *Development of hypoxia-sensitive Gd3+-based MRI contrast agents.* Bioorganic & Medicinal Chemistry Letters. **22**(8): p. 2798-2802.
141. Evans, M.C., et al., *Magnetic resonance imaging of pathological processes in rodent models of amyotrophic lateral sclerosis.* Amyotrophic Lateral Sclerosis. **13**(3): p. 288-301.
142. Frullano, L., et al., *A Myelin-Specific Contrast Agent for Magnetic Resonance Imaging of Myelination.* Journal of the American Chemical Society. **133**(6): p. 1611-1613.
143. Filippi, M. and M.A. Rocca, *Novel MRI approaches to assess patients with multiple sclerosis.* Current Opinion in Neurology. **23**(3): p. 212-217.
144. Serres, S., et al., *Molecular MRI enables early and sensitive detection of brain metastases.* Proceedings of the National Academy of Sciences of the United States of America. **109**(17): p. 6674-6679.
145. Sturzu, A., et al., *Novel Gastrin Receptor-Directed Contrast Agents - Potential in Brain Tumor Magnetic Resonance Imaging.* Medicinal Chemistry. **8**(2): p. 133-137.
146. Kobayashi, H., et al., *Avidin-dendrimer-(1B4M-Gd)(254): A tumor-targeting therapeutic agent for gadolinium neutron capture therapy of intraperitoneal disseminated tumor which can be monitored by MRI.* Bioconjugate Chemistry, 2001. **12**(4): p. 587-593.

147. Hirashima, Y., et al., *Pharmacokinetic parameters from 3-Tesla DCE-MRI as surrogate biomarkers of antitumor effects of bevacizumab plus FOLFIRI in colorectal cancer with liver metastasis.* International Journal of Cancer. **130**(10): p. 2359-2365.
148. Gianolio, E., et al., *MRI Paramagnetic Probes for Cellular Labeling.* European Journal of Inorganic Chemistry, (12): p. 1934-1944.
149. Addicott, B., et al., *Mesenchymal stem cell labeling and in vitro MR characterization at 1.5 T of new SPIO contrast agent: Molday ION Rhodamine-B (TM).* Contrast Media & Molecular Imaging. **6**(1): p. 7-18.
150. Neoh, K.G. and E.T. Kang, *Surface modification of magnetic nanoparticles for stem cell labeling.* Soft Matter. **8**(7): p. 2057-2069.
151. Guenoun, J., et al., *Cationic Gd-DTPA Liposomes for Highly Efficient Labeling of Mesenchymal Stem Cells and Cell Tracking With MRI.* Cell Transplantation. **21**(1): p. 191-205.
152. Battaglia, M., et al., *Validity of T2 mapping in characterization of the regeneration tissue by bone marrow derived cell transplantation in osteochondral lesions of the ankle.* European Journal of Radiology. **80**(2): p. E132-E139.
153. Wei, Z.M., et al., *Quantitative T2 mapping evaluation for articular cartilage lesions in a rabbit model of anterior cruciate ligament transection osteoarthritis.* Chinese Medical Journal. **125**(5): p. 843-850.
154. Li, X.L., et al., *Magnetite-loaded fluorine-containing polymeric micelles for magnetic resonance imaging and drug delivery.* Biomaterials. **33**(10): p. 3013-3024.
155. Chen, Y., et al., *Structure-property relationships in manganese oxide - nnesoporous silica nanoparticles used for T-1-weighted MRI and simultaneous anti-cancer drug delivery.* Biomaterials. **33**(7): p. 2388-2398.
156. Chen, Y.S., et al., *Peripheral nerve regeneration using silicone rubber chambers filled with collagen, laminin and fibronectin.* Biomaterials, 2000. **21**(15): p. 1541-1547.
157. Chang, Y.L., et al., *Synthesis and characterization of DOX-conjugated dendrimer-modified magnetic iron oxide conjugates for magnetic resonance imaging, targeting, and drug delivery.* Journal of Materials Chemistry. **22**(19): p. 9594-9601.
158. Thorek, D.L.J., et al., *Superparamagnetic iron oxide nanoparticle probes for molecular imaging.* Annals of Biomedical Engineering, 2006. **34**(1): p. 23-38.
159. Morawski, A.M., et al., *Targeted nanoparticles for quantitative imaging of sparse molecular epitopes with MRI.* Magnetic Resonance in Medicine, 2004. **51**(3): p. 480-486.
160. Saleh, A., et al., *In vivo MRI of brain inflammation in human ischaemic stroke.* Brain, 2004. **127**: p. 1670-1677.
161. Anzai, Y., et al., *Evaluation of neck and body metastases to nodes with ferumoxtran 10-enhanced MR imaging: Phase III safety and efficacy study.* Radiology, 2003. **228**(3): p. 777-788.
162. Stuckey, D.J., et al., *Iron particles for noninvasive monitoring of bone marrow stromal cell engraftment into, and isolation of viable engrafted donor cells from, the heart.* Stem Cells, 2006. **24**(8): p. 1968-1975.
163. Zhang, H., et al., *Injection of bone marrow mesenchymal stem cells in the borderline area of infarcted myocardium: Heart status and cell distribution.* Journal of Thoracic and Cardiovascular Surgery, 2007. **134**(5): p. 1234-U23.

164. Kubinova, S. and E. Sykova, *Nanotechnologies in regenerative medicine.* Minimally Invasive Therapy & Allied Technologies. **19**(3-4): p. 144-156.
165. Shapiro, E.M., et al., *MRI detection of single particles for cellular imaging.* Proceedings of the National Academy of Sciences of the United States of America, 2004. **101**(30): p. 10901-10906.
166. Stuckey, D.J., et al., *Magnetic Resonance Imaging Evaluation of Remodeling by Cardiac Elastomeric Tissue Scaffold Biomaterials in a Rat Model of Myocardial Infarction.* Tissue Engineering Part A. **16**(11): p. 3395-3402.
167. Terrovitis, J.V., et al., *Magnetic resonance imaging of ferumoxide-labeled mesenchymal stem cells seeded on collagen scaffolds - Relevance to tissue engineering.* Tissue Engineering, 2006. **12**(10): p. 2765-2775.
168. Obenaus, A., et al., *Long-Term Magnetic Resonance Imaging of Stem Cells in Neonatal Ischemic Injury.* Annals of Neurology. **69**(2): p. 282-291.
169. Ko, I.K., et al., *In vivo MR imaging of tissue-engineered human mesenchymal stem cells transplanted to mouse: A preliminary study.* Annals of Biomedical Engineering, 2007. **35**(1): p. 101-108.
170. Saldanha, K.J., et al., *Micrometer-sized iron oxide particle labeling of mesenchymal stem cells for magnetic resonance imaging-based monitoring of cartilage tissue engineering.* Magnetic Resonance Imaging. **29**(1): p. 40-49.
171. Poirier-Quinot, M., et al., *High-Resolution 1.5-Tesla Magnetic Resonance Imaging for Tissue-Engineered Constructs: A Noninvasive Tool to Assess Three-Dimensional Scaffold Architecture and Cell Seeding.* Tissue Engineering Part C-Methods. **16**(2): p. 185-200.
172. Zhang, S.Z., et al., *Tracking Intrahepatically Transplanted Islets Labeled With Feridex-Polyethyleneimine Complex Using a Clinical 3.0-T Magnetic Resonance Imaging Scanner.* Pancreas, 2009. **38**(3): p. 293-302.
173. Koblas, T., et al., *Magnetic resonance imaging of intrahepatically transplanted islets using paramagnetic beads.* Transplantation Proceedings, 2005. **37**(8): p. 3493-3495.
174. Cheng, H.-L.M., Y. Loai, and W.A. Farhat, *Monitoring tissue development in acellular matrix-based regeneration for bladder tissue engineering: Multiexponential diffusion and T2* for improved specificity.* NMR in Biomedicine. **25**(3): p. 418-426.
175. Ling, Y., et al., *Temozolomide loaded PLGA-based superparamagnetic nanoparticles for magnetic resonance imaging and treatment of malignant glioma.* Int J Pharm.
176. Ramaswamy, S., et al., *Superparamagnetic iron oxide (SPIO) labeling efficiency and subsequent MRI tracking of native cell populations pertinent to pulmonary heart valve tissue engineering studies.* NMR in Biomedicine. **25**(3): p. 410-417.
177. Vey, E., et al., *The impact of chemical composition on the degradation kinetics of poly(lactic-co-glycolic) acid copolymers cast films in phosphate buffer solution.* Polymer Degradation and Stability. **97**(3): p. 358-365.
178. Yang, Y.F., et al., *Effect of Cyclic Loading on In Vitro Degradation of Poly(L-lactide-co-glycolide) Scaffolds.* Journal of Biomaterials Science-Polymer Edition. **21**(1): p. 53-66.
179. Dorati, R., et al., *Effect of porogen on the physico-chemical properties and degradation performance of PLGA scaffolds.* Polymer Degradation and Stability. **95**(4): p. 694-701.

180. Paakinaho, K., et al., *Effects of lactide monomer on the hydrolytic degradation of poly(lactide-co-glycolide) 85L/15G.* Journal of the Mechanical Behavior of Biomedical Materials. **4**(7): p. 1283-1290.
181. Ling, Y., et al., *Dual docetaxel/superparamagnetic iron oxide loaded nanoparticles for both targeting magnetic resonance imaging and cancer therapy.* Biomaterials. **32**(29): p. 7139-7150.
182. Wang, Y., et al., *Formulation of Superparamagnetic Iron Oxides by Nanoparticles of Biodegradable Polymers for Magnetic Resonance Imaging.* Advanced Functional Materials, 2008. **18**(2): p. 308-318.
183. Lee, S.J., et al., *Nanoparticles of magnetic ferric oxides encapsulated with poly(D,L latide-co-glycolide) and their applications to magnetic resonance imaging contrast agent.* Journal of Magnetism and Magnetic Materials, 2004. **272**: p. 2432-2433.
184. Ramaswamy, S., et al., *Assessment of tissue repair in full thickness chondral defects in the rabbit using magnetic resonance imaging transverse relaxation measurements.* Journal of Biomedical Materials Research Part B-Applied Biomaterials, 2008. **86B**(2): p. 375-380.
185. Qiao, R., C. Yang, and M. Gao, *Superparamagnetic iron oxide nanoparticles: from preparations to in vivo MRI applications.* Journal of Materials Chemistry, 2009. **19**(35): p. 6274-6293.
186. Tanimoto, A., et al., *Relaxation effects of clustered particles.* Journal of Magnetic Resonance Imaging, 2001. **14**(1): p. 72-77.
187. van der Zande, M., et al., *In Vivo Magnetic Resonance Imaging of the Distribution Pattern of Gadonanotubes Released from a Degrading Poly(Lactic-Co-Glycolic Acid) Scaffold.* Tissue Engineering Part C-Methods. **17**(1): p. 19-26.
188. Yoshioka, T., et al., *Structural Changes and Biodegradation of PLLA, PCL, and PLGA Sponges During In Vitro Incubation.* Polymer Engineering and Science. **50**(10): p. 1895-1903.
189. Yang, Y., et al., *In vitro degradation of porous poly(l-lactide-co-glycolide)/Î²-tricalcium phosphate (PLGA/Î²-TCP) scaffolds under dynamic and static conditions.* Polymer Degradation and Stability, 2008. **93**(10): p. 1838-1845.
190. Agrawal, C.M. and R.B. Ray, *Biodegradable polymeric scaffolds for musculoskeletal tissue engineering.* Journal of Biomedical Materials Research, 2001. **55**(2): p. 141-150.
191. Ramaswamy, S., et al., *An analysis of the integration between articular cartilage and nondegradable hydrogel using magnetic resonance imaging.* Journal of Biomedical Materials Research Part B-Applied Biomaterials, 2006. **77B**(1): p. 144-148.
192. Hartman, E.H.M., et al., *In vivo magnetic resonance imaging explorative study of ectopic bone formation in the rat.* Tissue Engineering, 2002. **8**(6): p. 1029-1036.
193. Jendelova, P., et al., *Imaging the fate of implanted bone marrow stromal cells labeled with superparamagnetic nanoparticles.* Magnetic Resonance in Medicine, 2003. **50**(4): p. 767-776.

A_1: Mass loss (%) and Water uptake (%) measurements of PLGA hollow fiber channels with 0% SPIO

Week 1	**Sample 1**	**Sample 2**	**Sample 3**	**Mass loss %**	**Water uptake %**
$M_{initial}$ (mg)	57.24	66.64	63.73	2.236198	136.8835
M_{wet} (mg)	132.56	125.55	121.15	4.951981	98.21598
M_{dry} (mg)	55.96	63.34	62.72	1.584811	93.16008
Average				**2.92433**	**109.4198**
Standard deviation				**1.785946**	**23.91818**

Week 2	**Sample 1**	**Sample 2**	**Sample 3**	**Mass loss %**	**Water uptake %**
$M_{initial}$ (mg)	70.97	104.85	77.77	2.944906	113.2549
M_{wet} (mg)	146.89	209.88	157.97	2.832618	106.0071
M_{dry} (mg)	68.88	101.88	75.44	2.996014	109.3982
Average				**2.924513**	**109.5534**
Standard deviation				**0.083585**	**3.626426**

Week 3	Sample 1	Sample 2	Sample 3	Mass loss %	Water uptake %
$M_{initial}$ (mg)	39.58	45.09	80.08	2.753916	121.0964
M_{wet} (mg)	85.1	93.6	147.7	3.393214	114.876
M_{dry} (mg)	38.49	43.56	77.88	2.747253	89.65074
Average				**2.964794**	**108.5411**
Standard deviation				**0.371037**	**16.65251**

Week 4	Sample 1	Sample 2	Sample 3	Mass loss %	Water uptake %
$M_{initial}$ (mg)	52.07	91.11	122.41	2.842328	108.1439
M_{wet} (mg)	105.3	175.25	265.92	2.315882	96.91011
M_{dry} (mg)	50.59	89	119.16	2.655012	123.1621
Average				**2.604407**	**109.4054**
Standard deviation				**0.266846**	**13.1714**

Week 5	Sample 1	Sample 2	Sample 3	Mass loss %	Water uptake %
$M_{initial}$ (mg)	74.18	84.88	85.57	11.93044	153.2068
M_{wet} (mg)	165.42	176.22	172.3	11.07446	133.4658
M_{dry} (mg)	65.33	75.48	76.03	11.14877	126.6211
Average				**11.38455**	**137.7646**
Standard deviation				**0.474208**	**13.80433**

Week 6	Sample 1	Sample 2	Sample 3	Mass loss %	Water uptake %
$M_{initial}$ (mg)	62.42	54.43	93.43	29.6059	264.1329
M_{wet} (mg)	160	130.52	266.28	27.246	229.596
M_{dry} (mg)	43.94	39.6	72.56	22.33758	266.9791
Average				**26.39649**	**253.5693**
Standard deviation				**3.707878**	**20.81024**

Week 7	Sample 1	Sample 2	Sample 3	Mass loss %	Water uptake %
$M_{initial}$ (mg)	60.36	62.97	56.31	47.20013	389.1748
M_{wet} (mg)	155.9	159.41	151.65	51.48483	421.8003
M_{dry} (mg)	31.87	30.55	25.45	54.80376	495.8743
Average				**51.16291**	**435.6165**
Standard deviation				**3.112505**	**44.64198**

Week 8	Sample 1	Sample 2	Sample 3	Mass loss %	Water uptake %
$M_{initial}$ (mg)	54.56	51.32	59.34	74.78006	656.686
M_{wet} (mg)	104.12	101.98	122.45	74.98051	694.2368
M_{dry} (mg)	13.76	12.84	16.9	71.52005	624.5562
Average				**73.76021**	**658.493**
Standard deviation				**1.942619**	**34.8754**

A_2: Matlab programming codes to extract signal intensity, calculate T_2 relaxation time, plot T_2 map from raw MR images for various 24 echo times (13.1 msec to 314.4 msec)

```
ima=analyze75read(filename)
dim= size(ima);
echo=[13.1:13.1:314.4];

figure
imagesc(ima(:,:,1));
[X,Y]=getpts;
X=round(X);
Y=round(Y);

RR=size(X,1);
for a=1:size(ima,4);
    for b=1:RR;
signal_decay(a)=mean(ima(Y(b),X(b),a));
    end
end
clear a;
figure
plot(echo,signal_decay,'xr')
for x=1:dim(1);
   for y=1:dim(2)
       decay(1,:)=(ima(x,y,:));
       [p]=polyfit(echo,log(decay),1);
       map(x,y)=-1/p(1);
    end
end
figure
imagesc(map,[0 2000]);
```

A_3: Matlab programming codes to fit the curves for MR signal intensity of different SPIO concentration (0.05%, 0.1%, and 0.2%) versus various echo times (13.3 to 314.4 ms)

```
echo=[13.3 26.6 39.9 53.2 66.5 79.8 93.1 106.4 119.7 133 146.3
159.6 172.9 186.2 199.5 212.8 226.1 239.4 252.7 266 279.3
292.6 305.9 319.2];
spio05=[992.425 1063.8 991.813 1006.82 965.618 978.063 959.805
959.515 948.953 923.048 925.302 919.828 906.722 898.72 908.637
887.852 885.018 889.816 866.454 873.828 850.467 868.063
844.702 849.516];
spio10=[741.558 789.938 738.386 755.999 727.518 727.179
714.106 716.344 710.902 700.308 707.713 684.336 678.894
686.267 683.385 670.263 677.653 659.395 664.209 656.223
658.444 653.035 647.593 642.151];
spio20=[608.477 580.013 513.134 499.996 486.89 453.306 445.288
437.286 413.957 434.081 415.856 389.951 410.108 397.018
396.664 398.901 388.372 385.49 385.167 384.861 384.571 374.009
368.535 383.588];


fh1 = @(echo,p) p(1) + p(2)*exp(-echo./p(3));
errfh1 = @(p,echo,spio05) sum((spio05(:)-fh1(echo(:),p)).^2);
p01 = [mean(spio05) (max(spio05)-min(spio05)) (max(echo) -
min(echo))/2];
P1 = fminsearch(errfh1,p01,[],echo,spio05);

fh2 = @(echo,q) q(1) + q(2)*exp(-echo./q(3));
errfh2 = @(q,echo,spio10) sum((spio10(:)-fh2(echo(:),q)).^2);
p02 = [mean(spio10) (max(spio10)-min(spio10)) (max(echo) -
min(echo))/2];
P2 = fminsearch(errfh2,p02,[],echo,spio10);


fh3 = @(echo,r) r(1) + r(2)*exp(-echo./r(3));
errfh3 = @(r,echo,spio20) sum((spio20(:)-fh3(echo(:),r)).^2);
p03 = [mean(spio20) (max(spio20)-min(spio20)) (max(echo) -
min(echo))/2];
P3 = fminsearch(errfh3,p03,[],echo,spio20);
```

```
h=plot(echo, spio05, 'square');
set(h,'Color','k')
hold on
plot(echo,fh1(echo,P1),'k-')
hold on
j=plot(echo, spio10,'^');
set(j,'Color','k')
plot(echo,fh2(echo,P2),'k-')
hold on
L=plot(echo, spio20,'*k');
set(L,'Color','k')
plot(echo,fh3(echo,P3),'k-')

title('T2 decay curve')
legend('SPIO 0.05%', '','SPIO 0.10%','', 'SPIO 0.20%', '')
xlabel('Echo time (ms)')
ylabel('Signal Intensity')
```

A_4: Matlab programming codes to fit the curves of T2 relaxation times versus degradation time for PLGA hollow fiber channels loaded with various SPIO concentration (0%, 0.5%, 0.1% and 0.2%)

```
function curve()
SPIO1=[951, 1092, 1169, 1136, 1213, 1295, 1265, 1363, 1359 ];
SPIO2=[843, 861, 886, 916, 940, 1007, 1180, 1214, 1362, 1350,
1359, 1350, 1347];
SPIO3=[690, 771, 691, 776, 829, 847, 1094, 1178, 1334, 1135,
1138, 1015, 1225];
SPIO4=[546, 753, 631, 792, 678, 689, 803, 961, 1043, 1029,
1121];

x_axis1=1:9;
x_axis2=1:13;
x_axis3=1:13;
x_axis4=1:11;

SD1=[207 227 228 128 128 131 135 93 119];
SD2=[64 89 155 134 42 163 195 112 146 100 128 172 152];
SD3=[83 57 105 106 176 173 94 134 155 161 160 155 124];
SD4=[19 127 127 62 98 140 109 141 145 142 134];

figure1 = figure('Color',[1 1 1]);
f_ = clf;
figure(f_);
set(f_,'Units','Pixels','Position',[473 113 688 485]);

xlim_ = [Inf -Inf];

ax_ = axes;
set(ax_,'Units','normalized','OuterPosition',[0 0 1 1]);
set(ax_,'Box','on');
axes(ax_);
hold on;

x_axis1 = x_axis1(:);
SPIO1 = SPIO1(:);
```

```
h_ = line(x_axis1,SPIO1,'Parent',ax_,'Color',[0 0 0],...
    'LineStyle','none', 'LineWidth',1,...
    'Marker','square', 'MarkerSize',6);
xlim_(1) = min(xlim_(1),min(x_axis1));
xlim_(2) = max(xlim_(2),max(x_axis1));
hold on
errorbar(SPIO1,SD1,'k.');

x_axis2 = x_axis2(:);
SPIO2 = SPIO2(:);
h_ = line(x_axis2,SPIO2,'Parent',ax_,'Color',[0 0 0],...
    'LineStyle','none', 'LineWidth',1,...
    'Marker','^', 'MarkerSize',6);
xlim_(1) = min(xlim_(1),min(x_axis2));
xlim_(2) = max(xlim_(2),max(x_axis2));
hold on
errorbar(SPIO2,SD2,'k.');


x_axis3 = x_axis3(:);
SPIO3 = SPIO3(:);
h_ = line(x_axis3,SPIO3,'Parent',ax_,'Color',[0 0 0],...
    'LineStyle','none', 'LineWidth',1,...
    'Marker','*', 'MarkerSize',6);
xlim_(1) = min(xlim_(1),min(x_axis3));
xlim_(2) = max(xlim_(2),max(x_axis3));
hold on
errorbar(SPIO3,SD3,'k.');

x_axis4 = x_axis4(:);
SPIO4 = SPIO4(:);
h_ = line(x_axis4,SPIO4,'Parent',ax_,'Color',[0 0 0],...
    'LineStyle','none', 'LineWidth',1,...
    'Marker','o', 'MarkerSize',6);
xlim_(1) = min(xlim_(1),min(x_axis4));
xlim_(2) = max(xlim_(2),max(x_axis4));
hold on
errorbar(SPIO4,SD4,'k.');
```

```
if all(isfinite(xlim_))
    xlim_ = xlim_ + [-1 1] * 0.01 * diff(xlim_);
    set(ax_,'XLim',xlim_)
else
    set(ax_, 'XLim',[0.88, 13.119999999999999]);
end

fo_=fitoptions('method','NonlinearLeastSquares','Algorithm','L
evenberg-Marquardt');
ok_ = isfinite(x_axis1) & isfinite(SPIO1);

st_ = [0.56914457308758226 0.50190071557406613
0.67126885900980793 0.22216990068041154 ];
set(fo_,'Startpoint',st_);
ft_ = fittype('(A+((B-A)/(1+exp((C-x)/D))))',...
    'dependent',{'y'},'independent',{'x'},...
    'coefficients',{'A', 'B', 'C', 'D'});

cf_ = fit(x_axis1(ok_),SPIO1(ok_),ft_,fo_);

h_ = plot(cf_,'fit',0.95);
set(h_(1),'Color',[0 0 0],...
    'LineStyle','-', 'LineWidth',2,...
    'Marker','none', 'MarkerSize',6);

legend off;

fo_ =
fitoptions('method','NonlinearLeastSquares','Algorithm','Leven
berg-Marquardt');
ok_ = isfinite(x_axis2) & isfinite(SPIO2);

st_ = [0.56914457308758226 0.50190071557406613
0.67126885900980793 0.22216990068041154 ];
set(fo_,'Startpoint',st_);
ft_ = fittype('(A+((B-A)/(1+exp((C-x)/D))))',...
    'dependent',{'y'},'independent',{'x'},...
    'coefficients',{'A', 'B', 'C', 'D'});

cf_ = fit(x_axis2(ok_),SPIO2(ok_),ft_,fo_);
```

```
h_ = plot(cf_,'fit',0.95);
set(h_(1),'Color',[0 0 0],...
    'LineStyle','--', 'LineWidth',2,...
    'Marker','none', 'MarkerSize',6);
% Turn off legend created by plot method.
legend off;


fo_=fitoptions('method','NonlinearLeastSquares','Algorithm','L
evenberg-Marquardt');
ok_ = isfinite(x_axis3) & isfinite(SPIO3);

st_ = [0.56914457308758226 0.50190071557406613
0.67126885900980793 0.22216990068041154 ];
set(fo_,'Startpoint',st_);
ft_ = fittype('(A+((B-A)/(1+exp((C-x)/D))))',...
    'dependent',{'y'},'independent',{'x'},...
    'coefficients',{'A', 'B', 'C', 'D'});


cf_ = fit(x_axis3(ok_),SPIO3(ok_),ft_,fo_);


h_ = plot(cf_,'fit',0.95);
set(h_(1),'Color',[0 0 0],...
    'LineStyle','-.', 'LineWidth',2,...
    'Marker','none', 'MarkerSize',6);

legend off;

fo_=fitoptions('method','NonlinearLeastSquares','Algorithm','L
evenberg-Marquardt');
ok_ = isfinite(x_axis4) & isfinite(SPIO4);

st_ = [0.56914457308758226 0.50190071557406613
0.67126885900980793 0.22216990068041154 ];
set(fo_,'Startpoint',st_);
ft_ = fittype('(A+((B-A)/(1+exp((C-x)/D))))',...
    'dependent',{'y'},'independent',{'x'},...
    'coefficients',{'A', 'B', 'C', 'D'});
```

```
hold on
cf_ = fit(x_axis4(ok_),SPIO4(ok_),ft_,fo_);

hold on
h_ = plot(cf_,'fit',0.95);
set(h_(1),'Color',[0 0 0],...
    'LineStyle',':', 'LineWidth',2,...
    'Marker','none', 'MarkerSize',6);
legend off;
hold off;

xlabel('Time (weeks)')
ylabel('T_2 (ms)')
hold on
legend('SPIO 0.00%','','SPIO 0.05%','','SPIO 0.10%','','SPIO
0.20%', 'Location','SouthEast')
```